Université de Montréal

Magnetic resonance imaging of resting cerebral oxygen metabolism - applications in Alzheimer's disease

par Isabelle Lajoie

Département de Pharmacologie et Physiologie
de l'Université de Montréal
Faculté de Médecine

Thèse présentée
en vue de l'obtention du grade de Philosophiæ Doctor (Ph.D.)
en Génie Biomédical

Février, 2017

Résumé

Le contraste BOLD employé dans les études d'imagerie par résonance magnétique fonctionnelle (IRMf) provient d'une combinaison ambigüe de changements du flux sanguin cérébral, du volume sanguin ainsi que du métabolisme oxydatif. Dans un contexte où les fonctions vasculaires ou métaboliques du cerveau ont pu être affectées, tel qu'avec l'âge ou certaines maladies, il est crucial d'effectuer une décomposition du signal BOLD en composantes physiologiquement plus spécifiques. La dernière génération de méthodes d'IRMf calibrée permet d'estimer à la fois le flux sanguin cérébral et le métabolisme oxydatif au repos. Le présent travail est basé sur une telle technique, appelée QUantitative O2 (QUO2), qui, via un model généralisé, prend en considération les changements du flux sanguin ainsi que ceux en concentrations sanguine d'O_2 durant des périodes d'hypercapnie et d'hyperoxie, afin d'estimer, à chaque voxel, la fraction d'extraction d'oxygène et le métabolisme oxydatif au repos. Dans la première partie de cette thèse, le protocole d'acquisition ainsi que la stratégie d'analyse de l'approche QUO2 ont été revus afin d'améliorer la stabilité temporelle des réponses BOLD et du flux sanguin, conséquemment, afin d'accroître la fiabilité des paramètres estimés. Par la suite, une évaluation de la variabilité intra- et inter-sujet des différentes mesures QUO2 a été effectuée auprès d'un groupe de participants sains. En parallèle, une analyse de la sensibilité du model à différentes sources d'erreurs aléatoires (issues des mesures acquises) et systématiques (dues aux assomptions du model) a été réalisée. De plus, les impacts du niveau d'oxygène administré durant les périodes d'hyperoxie ont été évalués via une simulation puis expérimentalement, indiquant qu'une hyperoxie moyenne était bénéfique. Finalement, l'influence de la maladie d'Alzheimer sur les changements vasculaires et métaboliques a été explorée pour la première fois en appliquant le protocole QUO2 à une cohorte de patients Alzheimer et à un groupe témoin du même âge. Des différences en terme de flux sanguin, fraction d'oxygène extraite, métabolisme oxydatif, et taux de relaxation transverse R2* au repos comme en réponse à l'hypercapnie, ont été identifiées au niveau du voxel, ainsi qu'au niveau de régions cérébrales vulnérables à la maladie d'Alzheimer. Une liste de limitations accompagnées de recommandations a été dressée en ce qui a trait au temps

de transit différé, aux artéfacts de susceptibilité magnétique, de même qu'au défi que représente l'hypercapnie chez les personnes âgées ou atteintes de la maladie d'Alzheimer.

Mots-clés : IRMf calibré, hyperoxie, hypercapnie, exactitude et précision, métabolisme oxydatif au repos, fraction d'extraction d'oxygène, flux sanguin cérébral, santé vasculaire et métabolique, maladie d'Alzheimer

Abstract

The BOLD contrast employed in functional MRI studies is an ambiguous signal composed of changes in blood flow, blood volume and oxidative metabolism. In situations where the vasculature and metabolism may have been affected, such as in aging and in certain diseases, the dissociation of the more physiologically-specific components from the BOLD signal becomes crucial. The latest generation of calibrated functional MRI methods allows the estimation of both resting blood flow and absolute oxygen metabolism. The work presented here is based on one such proof-of-concept approach, dubbed QUO2, whereby taking into account, within a generalized model, both arbitrary changes in blood flow and blood O_2 content during a combination of hypercapnia and hyperoxia breathing manipulations, yields voxel-wise estimates of resting oxygen extraction fraction and oxidative metabolism. In the first part of this thesis, the QUO2 acquisition protocol and data analysis were revisited in order to enhance the temporal stability of individual blood flow and BOLD responses, consequently improving reliability of the model-derived estimates. Thereafter, an assessment of the within and between-subject variability of the optimized QUO2 measurements was performed on a group of healthy volunteers. In parallel, an analysis was performed of the sensitivity of the model to different sources of random and systematic errors, respectively due to errors in measurements and choice of assumed parameters values. Moreover, the various impacts of the oxygen concentration administered during the hyperoxia manipulation were evaluated through a simulation and experimentally, indicating that a mild hyperoxia was beneficial. Finally, the influence of Alzheimer's disease in vascular and metabolic changes was explored for the first time by applying the QUO2 approach in a cohort of probable Alzheimer's disease patients and age-matched control group. Voxel-wise and region-wise differences in resting blood flow, oxygen extraction fraction, oxidative metabolism, transverse relaxation rate constant R2* and R2* changes during hypercapnia were identified. A series of limitations along with recommended solutions was given with regards to the delayed transit time, the susceptibility artifacts and the challenge of performing a hypercapnia manipulation in cohorts of elderly and Alzheimer's patients.

Keywords: calibrated fMRI, hyperoxia, hypercapnia, accuracy and precision, resting oxidative metabolism, oxygen extraction fraction at rest, cerebral blood flow, vascular and metabolism health, Alzheimer's disease

Table of Contents

List of tables

List of figures

Abbreviations and acronyms

AC	Anterior cingulate
AD	Alzheimer's disease
APOE	Apolipoprotein E
APP	Amyloid precursor protein
ASL/pCASL/de-pCASL	Arterial spin labeling/Pseudo-continuous ASL/dual-echo pCASL
ATT	Arterial transit time
BET	Brain extraction tool
BOLD	Blood oxygen level-dependent
CaO_2	Arterial content of O_2
CBF	Cerebral blood flow
CBV	Cerebral blood volume
$CMRO_2$	Cerebral metabolic rate of O_2
CNR	Contrast to noise ratio
CO_2	Carbon dioxide
CR	Coefficient of repeatability
CV/wsCV/bsCV	Coefficient of variance/Within-subject CV/Between-subject CV
CVR	Cerebrovascular reactivity
EPI	Echo planar imaging
$ETO_2/ETCO_2$	End-tidal O_2/CO_2 concentration
FAST	FMRIB's automated segmentation tool
FDG	Fluoro-D-glucose
FI	Fixed-inspired
FLAIR	Fluid attenuated inversion recovery
fMRI	Functional magnetic resonance imaging
FSL	FMRIB Software Library
FWHM	Full width at half maximum
GCM	Generalized calibration model
GESSE	Gradient echo sampling of the spin echo

GLM	General linear model
GM	Grey matter
GRAPPA	Generalized autocalibrating partially parallel acquisition
GRE	Gradient echo
Hb/dHb	Hemoglobin/Deoxyhemoglobin
HC/HO	Hypecapnia/Hyperoxia
HIP	Hippocampus
HRF	Hemodynamic response function
IP	Inferior parietal
LHO/HHO	Lower/Higher hyperoxia
M	Maximal possible BOLD signal change
MCI	Mild cognitive impairment
MDD	Minimum detectable difference
MMSE	Mini-Mental State
MoCa	Montreal Cognitive Assessment
MPRAGE	Magnetization prepared rapid gradient echo
MRI	Magnetic resonance imaging
O_2	Oxygen
OEF	Oxygen extraction fraction
$PaO_2/PaCO_2$	Arterial partial pressure of O_2/CO_2
PC	Posterior cingulate
PD	Proton density
PET	Positron emission tomography
PLD	Post-labeling delay
PRE	Precuneus
qBOLD	Quantitative BOLD
QUIXOTIC	Quantitative imaging of extraction of oxygen and tissue
QUO2	Quantitative O2
ROI	Region-of-interest
RSN	Resting-state network
R^2	Coefficient of determination

R2*	Transverse relaxation rate constant
SD/wsSD	Standard deviation/Within-subject SD
SNR	(temporal) Signal-to-noise ratio
SP	Superior parietal
SWI	Susceptibility-weighted imaging
T	Tesla
T_1	Longitudinal relaxation time
T_2/T_2*	Transverse relaxation time
TE	Echo time
TR	Repetition time
tSNR	Temporal signal-to-noise ratio
VaD	Vascular dementia
WM	White matter
3D	Three-dimensional

Acknowledgments

J'aimerais d'abord remercier mon directeur de recherche, Rick, pour m'avoir offert cette opportunité d'apprendre et de travailler dans un domaine des plus stimulants. Merci pour la confiance placée en moi, pour les conseils scientifiques et pour cette touche humoristique qui aura adouci les différentes épreuves rencontrées.

Merci à Claudine et Felipe de m'avoir transmis une partie de leurs connaissances et de leur passion pour la recherche. Un merci tout spéciale à Felipe, qui aura été pour moi un mentor durant ces années de collaboration.

Un énorme merci à Anne-Marie, Lucile et Michel, dont le travail exceptionnel de coordination et d'assurance qualité aura grandement contribué au succès et à la qualité du travail de thèse.

Merci à Bahare, Marius, Mike-Ely, Scott, Clément et Santiego pour les discussions tantôt scientifiques, tantôt tout simplement loufoques et combien divertissantes!

Un merci chaleureux à mes parents qui ont toujours cru en moi et n'ont jamais arrêté de m'encourager, et ce malgré un parcours académique non traditionnel.

Un tendre merci à Jean-Philippe pour avoir agrémenté mon quotidien spécialement dans les moments plus difficiles. Merci de m'avoir soutenue tout au long et d'avoir fait preuve d'une constante compréhension malgré les heures accumulées de travail en soirée et les fins de semaine.

Finalement, un merci tout spécial à bébé Édouard, qui a su patienter au moins 39 semaines avant de se montrer le bout du nez, me permettant ainsi de mener à bien cette thèse avant de pouvoir savourer pleinement sa venue tant attendue dans nos vies.

1. Introduction

Alzheimer's disease (AD) is the most common type of dementia and there is substantial interest in better understanding the condition to help discover new treatments. Candidates for the primary causal factor of the disease include: cholinergic deficits [1], beta-amyloid (Aβ) deposition [2,3] and hyperphosphorylated tau pathology [4]. Additional factors that may have an important influence in the development of AD are: mitochondrial dysfunction [5-9] which tends to decrease the cerebral metabolic rate of O_2 ($CMRO_2$) consumption [10], and chronic hypoperfusion (a deficit in cerebral blood flow (CBF)) which could result in a lack of oxygen availability, leading to the beginning of mitochondrial failure [10]. Ultimately, a progressive synaptic, neuronal and axonal degeneration is observed. Given the above considerations, a detailed exploration of both oxidative metabolic ($CMRO_2$) and vascular (CBF) dysfunction is a promising avenue to consider in order to advance preventative and treatment strategies of the AD.

1.1. Positron emission tomography in AD

Positron emission tomography (PET) has been used to image resting oxygen consumption [11,12] in AD. However, imaging of $CMRO_2$ using PET is challenging as it requires an on-site cyclotron for the three separate administrations of the short-lived (half-life of about two minutes) ^{15}O radioactive tracers, each followed by an image acquisition of relatively low sensitivity [13], along with a number of arterial blood draws to measure blood radioactivity. Hence, this procedure is arduous for the patients and its adoption in large-scale research studies and clinical setting has been difficult. Despite the challenges associated with this approach, earlier PET studies have allowed the establishment of basic physiology associated with oxygen uptake deficits associated with AD. Ishii et al. observed an oxidative metabolism deficit in the medial temporal, lateral temporal and parietal cortices of AD relative to controls [14], which was later replicated [15-17], while no significant difference between the two groups was generally found with regards to oxygen extraction fraction (OEF) at rest. More recent results are in agreement with the hypothesis that oxidative metabolism may have a predominant role in the development of AD [18-23].

In addition to imaging of $CMRO_2$, PET is commonly used to image amyloid burden, regional perfusion and glucose uptake at rest (^{18}FDG, i.e. fluorodeoxyglucose). As opposed to the PET measures of $CMRO_2$, FDG-PET offers good sensitivity and spatial resolution, and since ^{18}F has a relatively long half-life, there is no need for an on-site cyclotron when used in clinical settings. Studies have shown a coupling between cerebral perfusion, glucose consumption and oxygen consumption, which includes a parietotemporal pattern of reduction in perfusion and glucose uptake. It was also observed that a frontal deficit was either associated with the degree of AD progression [24], or with frontotemporal dementia [25] and vascular disease [15].

1.2. Magnetic resonance imaging in AD

Similar to PET imaging, magnetic resonance imaging (MRI) has so far played an important role in the characterization of Alzheimer's disease. Structural MRI has been used to provide static anatomical information.

During a structural MRI scan, the application of an RF pulse forces protons in the brain tissue to align and thereafter, to revert back to their resting states following a certain longitudinal (T_1) and transverse (T_2) relaxation time. A different signal intensity is thereby observed across tissues and depends mainly on the amount of water in each voxel (proton density (PD)) as well as the longitudinal (T_1-weighted) and transverse (T_2-weighted) relaxation times, associated with each soft tissue. Hence, structural MRI offers a high spatial resolution view of soft tissue contrast, and is therefore well suited for the estimation of tissue damage or loss, an important biomarker in AD. The application of structural MRI in AD includes the characterization of whole-brain atrophy [26-29] or atrophy of vulnerable regions, such as the hippocampus [30-33] and entorhinal cortex [34], which are both part of the medial temporal lobe and implicated in the formation and storage of memories [35,36]. Additionally, it was found that the structural changes were particularly sensitive to progression from mild cognitive impairment (MCI), patients with early clinical signs of AD who don't fulfill the criteria for dementia, to moderate stages of AD [29,37].

Functional MRI (fMRI) provides dynamic physiological information and includes, among other parameters, blood oxygen level dependent (BOLD), connectivity and blood flow techniques.

The BOLD contrast mechanism results from the presence of different magnetic properties of oxygenated and deoxygenated hemoglobin [38]. While oxyhemoglobin (Hb) is diamagnetic, deoxyhemoglobin (dHb) is paramagnetic. The presence of paramagnetic dHb yields a decrease in the T_2*-weighted signal (1/R2*) due to increased signal inhomogeneity resulting from dephased water spins. As arterial blood is almost fully oxygenated, the attenuation of the T_2* signal comes from venous blood and tissue with dHb [39,40]. Following the elimination of all dHb, the BOLD value will be at its maximum, and will depend on the initial dHb concentration. During a task, blood velocity and vessel volume increase. The increase in perfusion exceeds that of the oxygen consumption rate, yielding a lower dHb concentration, and hence the BOLD increase we observe in fMRI (increase in the T_2*-weighted signal) [38,41].

The most common use of the BOLD technique for AD is the evaluation of functional responses during a memory-encoding task [42-44]. More recently, an additional fMRI approach was developed, that maps the resting-state network (RSN) connectivity in the brain. By removing the need for a task paradigm, this approach lessens the potential difficulties experienced by the patients and can simplify statistical analysis and interpretation of the results due to the large number of behavioral variables. Resting-state fMRI connectivity allows the study of spontaneous BOLD fluctuations over time and the identification of correlation patterns (or networks) between voxels. It was demonstrated that the basic brain networks were altered in AD compared to a cohort of healthy controls [45-47].

The arterial-spin-labeling (ASL) technique is a non-invasive MRI approach that, by labeling the blood water from the neck as it flows up toward the brain, creates a temporary endogenous contrast agent yielding a blood flow-dependent component in the brain's MRI signal that can be isolated and quantified by subtraction of the unlabeled control images. The ASL technique allows the quantitative measurement of resting CBF, task-related responses, as well as cerebrovascular reactivity (CVR). CVR is measured under hypercapnic conditions, i.e. when the arterial carbon dioxide content ($PaCO_2$) is increased, acting as a vasoactive agent

[48], hence increasing blood flow [49,50]. CVR is commonly expressed as the amplitude of CBF increase for a given increase of $PaCO_2$. ASL was previously applied to dementia to assess the resting vascular component of the condition [51,52] and most consistent result was the blood flow decrease in the precuneus and/or posterior cingulate, as well as in the lateral parietal cortex. Decreased blood flow in posterior cingulate was also observed in MCI, making it a good candidate for early detection of the disease. These flow decreases appear to be coupled with metabolism decreases observed using PET [24]. Findings in the temporal lobe are limited due to the small number of studies providing information in that region, however, it was suggested that blood flow in AD was decreased in inferior-lateral temporal cortex. Finally, few studies have pointed towards an increase in hippocampal blood flow [53,54].

1.3. Calibrated MRI: task-related changes of $CMRO_2$

The BOLD contrast obtained from conventional fMRI suffers from being unspecific, since it reflects multiple physiological processes such as changes in blood flow, blood volume and oxidative metabolism. In situations where a cohort of homogeneous participants is evaluated, BOLD contrast remains a non-invasive and accessible method with good sensitivity for mapping task-related responses. However, when heterogeneity is suspected between two cohorts of a vascular or metabolic nature, the BOLD signal becomes insufficient. In 1998, the term “calibrated MRI” was introduced by Tim Davis, to describe a method that combined the BOLD and the ASL responses to a hypercapnic manipulation, in order to calibrate the BOLD contrast and subsequently, to determine the quantitative changes in oxygen consumption encountered during a specific task [55]. This calibrated MRI was later referred as hypercapnically calibrated fMRI. In 2007, Peter Chiarelli et al. proposed a variation of the Davis hypercapnia approach, by replacing the hypercapnia periods with periods of hyperoxia, where participants were breathing air with enriched O_2 [56]. This new approach had the advantages of eliminating the discomfort associated with the carbon dioxide inhalation, excludes the possibility of CO_2 impacting the metabolism and reduces the importance of ASL. However, this technique implicates a set of assumptions, including a constant whole brain oxygen extraction fraction (OEF), which can in fact vary between regions and participants in cases of pathology [57]. In recent years, other groups have introduced the R2’ method [58],

which aims to estimate the calibration parameter *M* without requiring a gas manipulation, and the General Calibrated Model (GCM), introduced by our group [59], where the BOLD contrast could be calibrated for any arbitrary combinations of hypercapnic and hyperoxic manipulation. Compared to the original hypercapnic and hyperoxic approaches, the GCM was found to offer a better stability in the presence of noisy CBF signals [59]. Until then, the quantitative MRI methods were restricted to measure fractional changes in O_2 consumption (during a task) and were thus quantitative in relative terms only. Following the growing interest in the mapping of absolute baseline O_2 extraction fraction and O_2 consumption, novel MRI-based techniques were developed in this respect and are discussed next.

1.4. Baseline $CMRO_2$

The quantitative BOLD (qBOLD) method, described by He and Yablonskiy, is based on the Gradient Echo Sampling of Spin Echo (GESSE) sequence. With the use of a biophysical model, this sequence allows the extraction of the venous oxygen saturation in extravascular tissue and the estimation of the baseline OEF [60-62]. A major drawback of the qBOLD method is that it depends on a large number of assumed parameters, which are difficult to measure directly on an individual basis.

A second approach, dubbed QUIXOTIC (quantitative imaging of extraction of oxygen and tissue), uses a velocity-selective excitation scheme to isolate the venous blood oxygenation signal [63], from which the OEF and $CMRO_2$ can be obtained. An important limitation of the QUIXOTIC method is the need to know the precise velocity range in order to select the blood venular signal, a range that may differ with age and disease.

Finally, an alternative method has been suggested by Bulte et al. [64], in which the calibrated parameter *M* is determined employing the hypercapnia calibration [55] and then fitted in the hyperoxia calibration technique [56] to obtain the OEF. By combining the latter with measures of CBF and end-tidal O_2, the baseline estimate of $CMRO_2$ is retrieved. This method is closely related to the approach proposed by Gauthier et al., dubbed QUO2 (Quantitative O2) [65]. However, it possesses a larger number of assumptions, which differ between the hypercapnia and hyperoxia calibration, hence increasing its sources of systematic

errors and of physiological ambiguity [59]. The QUO2 approach was the starting point of this thesis and is described in further details in the following section.

1.5. QUO2: Quantitative O2

The approach, shown in Figure 1.1, combines periods of hypercapnia (HC) and hyperoxia (HO) with simultaneous acquisition of BOLD and CBF using dual-echo pCASL [65]. Meanwhile, end-tidal respiratory gases are non-invasively sampled. The end-tidal O_2, along with the BOLD and CBF voxel-wise responses to either one of the respiratory manipulation, are inputs to the GCM, yielding a functional curve of paired maximum BOLD increase (*M*) and OEF. Repeating the latter measurements under the other respiratory manipulation, results of an additional functional curve of dependency between *M* and OEF. By intersecting the two curves, thus solving the system of two equations, we obtain the voxel-wise value of *M* and OEF. The product of resulted arterial O_2 content (CAO_2), approximated by the end-tidal O_2, with resting CBF gives us the O_2 delivery, which multiplied by OEF, yields the resting $CMRO_2$ in micromolar units. Moreover, in addition to providing estimates of M, OEF and $CMRO_2$, the QUO2 method offers vascular information such as the baseline blood velocity and the CO_2-mediated cerebrovascular reactivity (CVR).

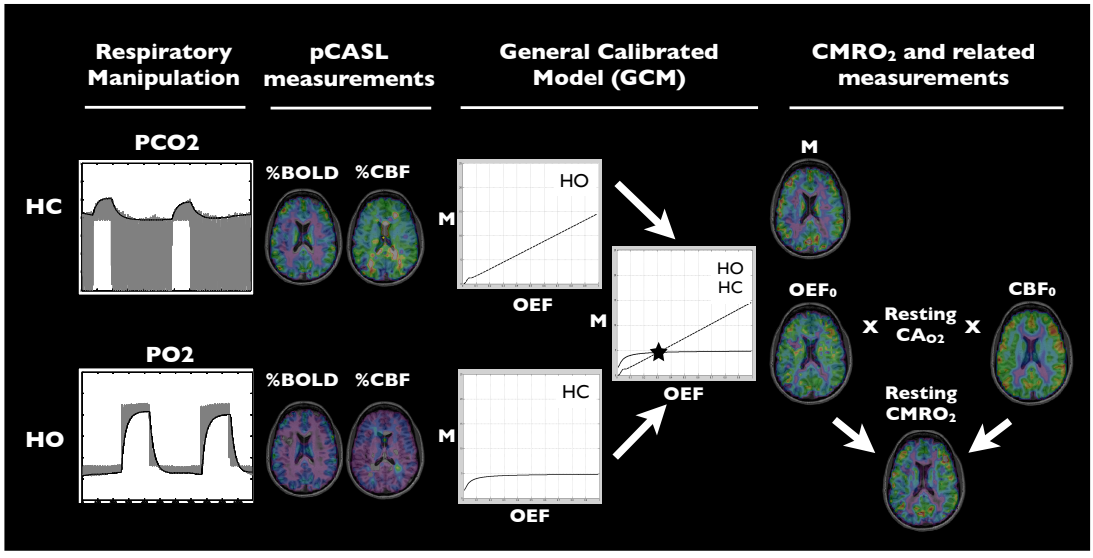

Figure 1.1. The Quantitative O2 (QUO2) approach
The approach combines periods of hypercapnia (HC) and hyperoxia (HO) with simultaneous acquisition of blood oxygen level dependent (BOLD) and cerebral blood flow (CBF) using a

dual-echo version of pseudo-continuous arterial spin labeling (pCASL). A Generalized Calibration Model (GCM) is fed with obtained measurements yielding a fully determined system of two equations and two unknowns: Oxygen Extraction Fraction (OEF), and extrapolated maximum BOLD signal increase (*M*). The product of resulted arterial O_2 content (CAO_2) with resting CBF gives us the O_2 delivery, which multiplied by OEF, yields the resting cerebral metabolic rate of O_2 ($CMRO_2$) in micromolar units.

The QUO2 method thus offers the possibility of employing a widely available system that does not imply any ionizing radiation or arterial catheterization, to help better characterize the vascular and metabolic burdens of disease such as AD. Another major advantage of QUO2 fMRI over other modalities is that structural, vascular and connectivity measurements can be performed concurrently. Together, these allow correlation of structural and functional measurements within a single modality.

1.6. The present thesis work

Prior to the beginning of the work presented in this thesis, the initial proof-of-concept QUO2 had been tested in seven healthy volunteers [65], and, while it proved to produce valid regional and group-averaged estimates of *M*, OEF and $CMRO_2$, it showed signs of instability and lack of solutions in individual maps. These preliminary results were encouraging, but further improvement, validation and evaluation of the technique were needed (Tancredi et al. [66,67], Chapter 2-3) prior to its application in an AD population (Chapter 4).

The initial application of the proof-of-concept QUO2 method employed a standard oxygen breathing circuit, which needed to be fixed to the participant's face using tape in order to avoid contamination from room air. Even with the use of tape (which could induce discomfort and an increased feeling of claustrophobia for certain participants), it was observed that the use of the standard oxygen mask yielded unstable fractional concentrations of inspired O_2 or CO_2, as well as a dependency between end-tidal measurements and the administered flow rate [66]. In order to increase the participant's comfort and stability in inspired and end-tidal values, we developed a breathing circuit, presented in Tancredi et al. [66], which was employed throughout the present work. The latter, by incorporating an open reservoir through

which the participant could breathe room air whenever the provided flow become insufficient, also provides, over the simple oxygen mask, additional safety to the participant.

Thereafter, an assessment of the precision (Tancredi et al. [67], Chapter 2) and accuracy (Chapter 2) of QUO2 parameters was performed. Precision of the model-derived parameters will partly depend on the random error in the measurements of BOLD and CBF response to the respiratory manipulation. While previous work presented a simulation of the impact on *M* estimates of such errors in CBF measurements [59], the impact on OEF (and indirectly $CMRO_2$) to errors in BOLD measurements in addition to CBF, was still to be evaluated and was simulated in Chapter 2. Additionally, a reproducibility study was performed in eight healthy volunteers to determine the regional within- and between-subject variance (Chapter 2). On the other hand, the accuracy of model-derived estimates is impacted by systematic errors due to the assumed parameters used in the model. Chapter 2 presents the sensitivity of the model to the QUO2 assumed parameters described next. The Grubb parameter (α) defines the relationship between the venous blood flow and blood volume. It was originally estimated to be 0.38, based on work in anesthetized monkeys [68], but was later found to be 0.18 in adult humans [69,70]. The latter value has been used in several studies, including the present work. The β parameter represents the power-law relationship between dHb and transverse relaxation [71]. The original estimate of 1.5 at 3 Tesla was employed throughout the present work although alternate interpretations have been postulated corresponding to a lower value of 0.91 [72]. The hemoglobin concentration in blood ([Hb]) was set to 15 g Hb/dl blood the group of healthy volunteers in Chapter 2 and 3 [56,73]. However, considering that [Hb] varies with gender and age [74-76], and that it can be easily determined by a simple blood draw, we measured it in our probable AD and elderly cohorts of Chapter 4, hence eliminating the presence of systematic errors associated with the hemoglobin concentration in blood. An additional assumption made throughout the present work is that neither hyperoxia nor hypercapnia were yielding a change in oxidative metabolism. This assumption remains the subject of ongoing debate [77-83] and hence, the sensitivity of the model to any changes in $CMRO_2$ during either HC or HO was assessed. Finally, an assumed value [64,84] or the group-averaged value of blood flow changes during hyperoxia in calibrated fMRI is commonly employed [65,85] since its real value is often near the level of

ASL noise and because the correction for changes in blood T_1 during HO remains challenging. This latter correction will be discussed in the following section. For our younger healthy controls (Chapter 2 and 3), we used the individual T_1-corrected CBF_{HO} value and presented an evaluation of the QUO2 sensitivity to this parameter (Chapter 2). In Chapter 3, we opted for the use of group-averaged T_1-corrected value due to a larger noise level in our patients and elderly cohorts data compared to our younger healthy controls.

An additional factor that may contribute to the precision and accuracy of the QUO2 model-derived estimates is the oxygen concentration provided during the hyperoxia manipulation. A maximal level, such as 100% oxygen, may diminish the error in M estimation by bringing the BOLD changes closer to the maximum value. However, compared to a lower concentration of O_2, such as around 50%, the inhalation of 100% O_2 may result in a larger area of susceptibility artifacts near the sinuses due to the increased presence of paramagnetic oxygen molecule [86]. Additionally, the inhalation of air enriched with O_2, results in an increased paramagnetic O_2 concentration in plasma, which shortens the arterial relaxation time T_1 [87-89]. Since the ASL signal depends on the blood relaxation time [90], this decrease in T_1 must therefore be taken into account, otherwise the estimated response to hyperoxia will be overestimated. The T_1-correction throughout the present thesis was performed as follows: first, the T_1 during hyperoxia was linearly interpolated from literature values [89] based on our individual arterial partial pressure (PaO_2). Finally, a corrective factor was applied [91,92] based on the adjusted T_1 and the quantitative blood flow equation [93]. Hence, a higher level of O_2 concentration during HO may necessitate a greater T_1-correction, which could be prone to larger errors in T_1-corrected CBF response estimation. Chapter 3 was dedicated to the exploration of the above impacts of inspired oxygen levels on the QUO2 model-derived estimates, in order to determine the best compromise for the concentration of inspired O_2.

Finally, we recruited 65 probable AD dementia and 65 age-matched controls in order to apply the enhanced QUO2 calibrated fMRI for comparison of obtained estimates. The application of task-related calibrated fMRI was previously seen in aging [94-96], while only isolated studies evaluated the absolute oxygen metabolism applying a calibrated fMRI approach in aging or in internal carotid artery occlusion patients [97,98]. To our knowledge, this is the first application of such an approach in an Alzheimer's population, making this last

part of the present thesis a particularly novel contribution both in the developments of calibrated MRI techniques as well as in clinical and research applications in AD. Chapter 4 of this thesis presents the outcomes of the QUO2 application in AD.

In summary, in order to enhance the accuracy and robustness of the model-derived estimates, the temporal stability of the BOLD and CBF responses to respiratory manipulation were enhanced through improved respiratory monitoring with a novel breathing circuit [66]. Thereafter, the reproducibility in grey matter of the previous measurements was evaluated in healthy subjects [67]. Chapter 2 presents an enhancement in the QUO2 image analysis, the assessment of the within- and between-subject variance of the model-derived estimates, as well as the evaluation of sensitivity of the model to random and systematic errors. Chapter 3 assesses the impact of the O_2 level during the hyperoxia periods on M, OEF and $CMRO_2$. Finally, in Chapter 4, the QUO2 is applied in a cohort of probable AD and age-matched group control.

2. Regional Reproducibility of BOLD Calibration Parameter *M*, OEF and Resting-State $CMRO_2$ Measurements with QUO2 MRI

Authors: Isabelle Lajoie, Felipe B. Tancredi, Richard D. Hoge

Authors contributions: Study design and Software development: IL FBT RDH; Data acquisition: IL FBT; Formal analysis and Data interpretation: IL; Writing original draft and Visualization/Data presentation: IL; Project administration and Funding acquisition: RDH.

Status: Published in the journal *PLoS ONE*. 2016; 11(9): e0163071.

2.1. Preface

Calibrated fMRI was first proposed by Davis et al. [55], who employed a hypercapnic respiratory manipulation along with an MRI ASL sequence and a biophysical model. This allowed the quantification of task-evoked fractional $CMRO_2$. Considering the discomfort associated with the inhalation of air mixed with carbon dioxide, alternative techniques were developed. Chiarelli et al. proposed the hyperoxia calibration [56], whereas Blockley et al. suggested the use of the information in gradient and spin echoes to calibrate the BOLD signal without the need for a gas manipulation [58]. However, these two methods were found to be more sensitive to errors than the original hypercapnic calibration method [58]. A third method, the generalized calibration model (GCM), was proposed [59] that allows the calibration of the BOLD signal for any arbitrary combinations of hypercapnic and hyperoxic manipulations. This new approach was found to yield robust and accurate *M* maps and hence reliable estimations of the changes in $CMRO_2$ during a visual task.

The different calibrated fMRI approaches are limited by the fact that they report a relative change from unknown baselines, making them insufficient in situations where the studied groups have different baseline $CMRO_2$, such as in aging or dementia [19,99-101]. Moreover, they require a task, which may be arduous for certain clinical populations.

Therefore, several groups have developed MRI-based techniques allowing absolute quantification of resting $CMRO_2$ [61-64,102-105]. One such approach, which was dubbed Quantitative O_2 (QUO2) [65], combines two separate hypercapnia and hyperoxia manipulations using the GCM in order to estimate voxel-wise *M* and resting oxygen extraction fraction (OEF) values. The product of resting OEF, resting blood flow (issued from the MRI ASL sequence) and arterial oxygen content, yields the baseline $CMRO_2$.

The initial proof-of-concept for QUO2, applied in a population of healthy volunteers proved to yield regional and group-averaged estimates that were consistent with those of prior PET studies [65]. However, the voxel-wise individual maps suffered from instability and some voxels lacked solutions for OEF and *M*, while information about variance in its estimates as well as about its sensitivity to random and systematic errors were incomplete. Within the course of work of the present thesis, the first advance was achieved by the replacement of the

standard oxygen mask by a newly designed breathing circuit which proved to yield a better stability in the inspired concentration and hence in the end-tidal values [66]. This in turn led to a better temporal stability of the CBF and BOLD responses to the respiratory manipulations. Thereafter, end-tidal O_2/CO_2 and grey matter CBF/BOLD signals reproducibility were assessed, revealing generally robust and consistent measures, with blood flow response to hypercapnia being the most variable (CV<20%) [67].

Here, in Chapter 2, we propose a number of improvements for QUO2 MRI image analysis, followed by an investigation of the within- and between-subject repeatability of model-derived estimates within different key regions. Finally, the sensitivity of the model to different sources of random and systematic errors was established.

2.2. Abstract

The current generation of calibrated MRI methods goes beyond simple localization of task-related responses to allow the mapping of resting cerebral metabolic rate of oxygen ($CMRO_2$) in micromolar units and estimation of oxygen extraction fraction (OEF). Prior to the adoption of such techniques in neuroscience research applications, knowledge about the precision and accuracy of absolute estimates of $CMRO_2$ and OEF is crucial and remains unexplored to this day. In this study, we addressed the question of methodological precision by assessing the regional inter-subject variance and intra-subject reproducibility of the BOLD calibration parameter *M*, OEF, O_2 delivery and absolute $CMRO_2$ estimates derived from a state-of-the-art calibrated BOLD technique, the QUantitative O2 (QUO2) approach. We acquired simultaneous measurements of CBF and R2* at rest and during periods of hypercapnia (HC) and hyperoxia (HO) on two separate scan sessions within 24 hour using a clinical 3 T MRI scanner. Maps of *M*, OEF, oxygen delivery and $CMRO_2$, were estimated from the measured end-tidal O_2, CBF_0, $CBF_{HC/HO}$ and $R2^*_{HC/HO}$. Variability was assessed by computing the between-subject coefficients of variation (bwCV) and within-subject CV (wsCV) in seven ROIs. All tests GM-averaged values of CBF_0, *M*, OEF, O_2 delivery and $CMRO_2$ were: 49.5 ± 6.4 mL/100 g/min, 4.69 ± 0.91%, 0.37 ± 0.06, 377 ± 51 μmol/100 g/min and 143 ± 34 μmol/100 g/min respectively. The variability of parameter estimates was found to be the lowest when averaged throughout all GM, with general trends toward higher CVs

when averaged over smaller regions. Among the MRI measurements, the most reproducible across scans was $R2^*_0$ ($wsCV_{GM}$=0.33%) along with CBF_0 ($wsCV_{GM}$=3.88%) and $R2^*_{HC}$ ($wsCV_{GM}$=6.7%). CBF_{HC} and $R2^*_{HO}$ were found to have a higher intra-subject variability ($wsCV_{GM}$=22.4% and $wsCV_{GM}$=16% respectively), which is likely due to propagation of random measurement errors, especially for CBF_{HC} due to the low contrast-to-noise ratio intrinsic to ASL. Reproducibility of the QUO2 derived estimates were computed, yielding a GM intra-subject reproducibility of 3.87% for O_2 delivery, 16.8% for the *M* value, 13.6% for OEF and 15.2% for $CMRO_2$. Although these results focus on the precision of the QUO2 method, rather than the accuracy, the information will be useful for calculation of statistical power in future validation studies and ultimately for research applications of the method. The higher test-retest variability for the more extensively modeled parameters (*M*, OEF, and $CMRO_2$) highlights the need for further improvement of acquisition methods to reduce noise levels.

Key-words: Calibrated fMRI; Baseline oxidative metabolism; Reproducibility; Hypercapnia; Hyperoxia; de-pCASL

2.3. Introduction

Mapping of resting metabolism in the brain is of considerable interest for diagnostic and research applications. Until recently, positron emission tomography (PET) using a triple injection of radio-labeled O_2 was the only imaging method for measuring cerebral metabolic rate of O_2 consumption ($CMRO_2$) [11]. The PET method requires exposure to ionizing radiation, arterial sampling, and access to an on-site cyclotron to produce the short-lived ^{15}O-labeled tracers, limitations that have led to the development of magnetic resonance imaging (MRI) techniques to measure O_2 consumption [64,85,106].

The approach proposed by our team, Quantitative O2 (QUO2) MRI is based on respiratory calibration of the BOLD signal, in which the oxygen extraction fraction (OEF) at rest is determined using hypercapnia (HC) and hyperoxia (HO). During the respiratory manipulation, we monitor end-tidal O_2 (ETO_2) levels and use dual-echo ASL to measure BOLD and cerebral blood flow (CBF) simultaneously. ETO_2, BOLD and CBF then serve as inputs to the generalized calibration model (GCM) described in Gauthier and Hoge [59],

which yields a system of two equations with solutions for the BOLD calibration parameter *M,* i.e. the maximum BOLD signal increase when venous O_2 saturation approaches 100%, and resting OEF. Multiplication of OEF by baseline CBF and arterial O_2 content (estimated from ETO_2 monitoring and, optionally, blood testing) gives resting $CMRO_2$ in absolute units, e.g. μmol/100 g/min.

An initial proof-of-concept of the QUO2 method was presented in Gauthier and Hoge [65] to obtain individual and group maps of BOLD calibration parameter *M*, resting OEF and $CMRO_2$. While valid regional and group-averaged estimates of the latter parameters were obtained, individual OEF maps showed signs of instability characterized by large fluctuations in the modeled values and a lack of solution in certain regions. The stability of individual solution maps generated using this method depends on accurate and robust measures of end-tidal O_2 and maps of fractional changes in BOLD and CBF during the respiratory manipulation. In an attempt to improve the stability and avoid circumstances where the QUO2 model cannot be solved, we have adapted the imaging and respiratory protocols used in several ways. Instead of performing two separate respiratory scans for hyperoxia and hypercapnia, we have adopted the 18-minute respiratory sequence that alternates between periods of hypercapnia and hyperoxia [64] and during which the total time dedicated to each gas manipulation is increased compared to the original protocol, improving statistical power. We developed a simple breathing circuit allowing a better control over fractional concentration of inspired gas and thus yielding improved stability of end-tidal values compared with the simple oxygen masks used in our earlier studies [66]. Combining a version of the pseudo-continuous ASL sequence (de-pCASL), the respiratory protocol and breathing circuit mentioned above, we assessed the test-retest reliability in the respiratory responses and in CBF and BOLD responses within GM [67]. In the present study, we attempted to further improve the voxel-wise image quality in single-subject maps by performing an integrated analysis on the dual-echo pCASL data. The novel analysis strategy (further described in Materials and Methods) involved 1) motion correcting the interleaved echo series using the same transformation for the two echo times; 2) applying a more holistic general linear model on the motion-corrected series to extract baseline parameters and gas responses using one regressor per combination of echo and tag/control; 3) employing both echoes information to

estimate R2* rather than approximating it from the second echo; and 4) employing a more sophisticated approach to mitigate solution instabilities from isolated non-parenchymal voxels using 3D median filtering.

The aim of this study was to assess, in a small cohort of healthy individuals, the variability of the optimized QUO2 measures across and within subject in different brain regions. These results, based on the precision of the method, will help guide future developments and research application of the method. The following estimates were obtained: BOLD calibration parameter *M*, OEF, O_2 delivery and resting $CMRO_2$. The impact of systematic and random errors on the accuracy and precision of such estimates was also evaluated. Furthermore, these estimates were compared with CBF and BOLD-based reproducibility estimates derived from the same group of subjects and same enhanced analysis.

2.4. Materials and Methods

Eight healthy adults were enrolled in this study (4 females, mean age: 30.5 ± 5.7 years). Two participants were current smokers. None of the participants had asthma, previous history of cardiovascular, cerebrovascular or respiratory diseases. One participant was treated for hypothyroidism. All participants gave written informed consent and the project was approved by the Comité mixte d'éthique de la recherche du Regroupement Neuroimagerie/Québec. They were scanned twice (referred to as Test A and Test B), within 24 hour, using the same imaging procedures and respiratory manipulation. To minimize effects of diurnal fluctuation in blood flow, all sessions was acquired between 2 PM and 6 PM [107]. The participants were asked to abstain from caffeine 3 hours prior to scanning.

2.4.1. Respiratory Manipulation

For the respiratory manipulation, we adopted the gas sequence described by Bulte et al. [64] with a total duration of 18 minutes. This involves two 2-min periods of hypercapnia (HC) and two 3-min periods of hyperoxia (HO). HC was followed by a 1-min normocapnic period and then the 3-min hyperoxic stimulus. HO was followed by a 3-min period of normoxia.

HC and HO blocks were induced by supplying participants with gas mixtures enriched with CO_2 or O_2. Participants breathed the gas mixtures through the breathing circuit developed in-house [66]. An automated system, also developed in-house, was used to deliver the gas mixtures with a reproducible time course in all scanning sessions. The system comprises 4 flow controllers (SideTrak® 840, Sierra instruments, L. Monterey, CA, USA), a ~25 mL mixing chamber, a digital interface (Sierra, FloBox^{TM} 954) to send commands to the flow controllers and a laptop computer to automate the gas mixture processes and collect behavioral data. The system's output is connected to the breathing circuit via 10 meters of plastic tubing (BIOPAC, AFT31-MRI). Three gases were input to the flow controllers: medical air, oxygen and a 5% CO_2 and air mixture. During the hyperoxia periods, subjects breathed a mixture of 50% pure oxygen balanced with air, yielding a fix inspired O_2 concentration of 60% O_2. Otherwise, participants were given medical air to breathe. Gas mixtures were administered at a rate of 20 L/min, except during transitions in inspired concentrations, during which the flow rate was increased to 50 L/min for 5.4 seconds in order to accelerate transitions.

Respiratory gases were continuously monitored using the CO2100C and O2100C modules of a BIOPAC MP150 system (BIOPAC Systems Inc., CA, USA). Gases were sampled via a 10m segment of rigid tubing (AFT31-XL, from BIOPAC System Inc.) in series with a bacterial filter (#2200/01, GVS filter technology, LA, UK) and 1' segment of oxygen tubing attached to the sampling port of the respiratory circuit.

2.4.2. Image Acquisition

Images were acquired on a clinical 3 T scanner (Siemens TIM TRIO, Siemens Medical Solutions, Erlangen, Germany) using the vendor's 32-channel receive-only head coil. The scan session included a 5-minute anatomical acquisition (1 mm^3 MPRAGE with TR/TE/flip angle = 2.3 seconds/3 msec/9°, 256x240 matrix, GRAPPA factor = 2), and an 18-minute functional scan using a dual-echo version of pseudo-continuous ASL sequence (de-pCASL) [108] in order to acquire simultaneous measures of BOLD and CBF. The de-pCASL parameters were: TR/TE1/TE2/alpha = 4.12 seconds/8.4 msec/30 msec/90°, labeling duration = 2 seconds using Hanning window-shaped RF pulse with duration/space = 500 μsec/360 μsec, flip angle = 25°, slice-selective gradient = 6 mT/m, label offset = 100 mm below the center of image slab,

nominal and average post-labeling delay (PLD) = 0.9 and 1.44 seconds respectively. The readout consisted of a GRE-EPI with GRAPPA factor = 2, partial sampling of k-space = 7/8, in-plane resolution of 4.5 x 4.5 mm^2, 21 slices with 4.5 mm thickness and 0.45 mm gap.

2.4.3. Respiratory Data Analysis

Analysis of the respiratory data was carried out using an in-house program developed in Matlab (MathWorks, Natick, MA, USA). An automatic extraction of the end-tidal (ET) and fixed-inspired (FI) points from the continuous O_2 and CO_2 traces was performed. It was observed that the filter placed in series with the sampling line added an extra resistance causing an effect of low-pass filtering to the respiratory waveform. This resulted in an offset of both the ET and FI monitored pressures, i.e. an attenuation of the peak-to-peak amplitude of the waveform, which was dependent on the participant's breathing pace. Each ET point was corrected using the average of the differences between the observed and expected FI points surrounding it. ET values were also corrected to account for an expired partial pressure of water of 47 mmHg [109]. The resting ET and changes in ET during HC and HO periods were determined by applying the linear model previously described [110]. The model is composed of a third-degree polynomial term and four regressors to represent responses to the hypercapnic and hyperoxic blocks. The offset term served to estimate the baseline ET whereas the effect size of each response regressor yielded an estimate of the associated ET change. Final ETO_2 change to periods of HO was obtained by averaging the two ETO_2 changes to HO. The same method was employed to compute the final ETO_2 change to periods of HC, and $ETCO_2$ responses to both gases.

The average values of ETO_2 at baseline and during both respiratory stimuli were used to compute arterial O_2 content (ml O_2/ml blood) and change in the venous deoxygenated fraction ($[dHb]/[dHb]_0$) as in Chiarelli et al. [56] and Gauthier et al. [85]. The latter quantities are integrated to obtain the BOLD calibrated value M, resting OEF and $CMRO_2$ as specified below.

2.4.4. Imaging Data Analysis

2.4.4.1. Preprocessing

Analysis of functional scans was performed using in-house software implemented in C. The interleaved echo series was motion corrected with consecutive first and second echo frames sharing the same transformation matrix. The resultant series was spatially filtered (8mm FWHM 3D Gaussian kernel), had extra-cerebral voxels removed and was intensity normalized (brain mean 100). The fMRI data were then fit to a GLM to extract the label and control series of both echoes during baseline, hypercapnia and hyperoxia periods. The model used four regressors per conditions to account for both echoes label and control points, and a third-degree polynomial with an offset term representing signal drifts. We used a single-gamma HRF function with 20 seconds time-to-peak and 40 seconds width, which yielded near-exponential transitions to account for the slow response of the arterial partial pressures to the inspired gas [111]. ASL (S0) and BOLD (R2* or $1/T_2$*) control and label series at baseline and during gas manipulations were computed using both echoes information. ASL flow series were computed from subtraction of S0 control to S0 label series, whereas BOLD series were isolated averaging the control and label R2* series. A 3D median filtering (radius of 1 voxel) was applied on the resultant maps to minimize the impact of non-parenchymal voxels such as those containing large blood vessels.

The functional maps produced by the above analysis were then used to further reduce the impact of voxels not meeting the assumptions of the QUO2 model: Baseline T_2* maps served to exclude voxels in regions degraded by susceptibility artifacts (lower threshold of 30ms). Voxels in which $\Delta R2^*_{HO}$ was positive were assumed to be dominated by susceptibility artifacts from adjacent nasal cavity due to the paramagnetic effect of molecular O_2. Additional voxels with positive $\Delta R2^*_{HC}$ were considered as non-parenchymal and were also excluded from the analysis. The ASL signal was converted into physiological units of flow (mL/100 g/min) as in Wang et al. [93] using the constants recommended by the ISMRM Working Committee [112] and an adjusted PLD to account for slice acquisition time (PLD range for 21 slices of 900-1960ms).

During hyperoxic manipulation, the T_1 of blood is altered due to an increase in plasma concentration of paramagnetic O_2 [89]. To account for this change in blood T_1, which would bias our $\Delta\%CBF_{HO}$ estimation, we applied a corrective factor using the approach described in Chalela et al. [91] and Zaharchuk et al. [92]. The T_1 of blood during hyperoxic intervals was estimated individually using the R1 and PaO_2 relationship in rats' blood reported in Pilkinton et al. [89].

2.4.4.2. Computation of metabolism

For each gas challenge, the changes in the venous deoxygenated fraction, along with the change in BOLD ($\Delta R2^*$) and CBF were used as inputs to the generalized calibration model (GCM) described in Gauthier et al. [59]. This yields a system of two equations with two unknowns: the BOLD calibration parameter M (extrapolated maximum BOLD fractional signal increase when venous O_2 saturation approaches 100%) and OEF (the fraction of delivered oxygen that is consumed). Absolute $CMRO_2$ was then determined by multiplying OEF by O_2 delivery, computed as the product of resting CBF by arterial O_2 content. In the absence of intersection in between the HC and HO curves, the voxel is said to have no solution and will later be excluded from any ROI or voxel average in M, OEF and $CMRO_2$. Because of the low CNR of the ASL hyperoxic response, the GM-averaged value obtained from the post-T_1-correction $\Delta\%CBF_{HO}$ was used as an estimate of the whole-brain post-T_1-correction $\Delta\%CBF_{HO}$. Previous studies [56,85] also report using a whole-brain estimate of $\Delta\%CBF_{HO}$, with the difference that, in the current paper, the value was computed for each participant. In the equation defining M (Gauthier and Hoge [59], equation 7), the parameter α, which expresses the relationship between changes in blood flow and blood volume, was assumed to be 0.18 [70] while β, defining the non-linear dependence of changes in R2* on deoxygenated hemoglobin, was set to 1.5 [71]. The hemoglobin concentration [Hb] was assumed to be 15 g Hb/dl blood, although this can be readily measured using a venous blood draw. It was also assumed that oxygen consumption remained constant during periods of hypercapnia and hyperoxia ($CMRO2_{HC}$ and $CMRO2_{HO}$). The sensitivity of QUO2 model-derived estimates to the assumed parameters was also evaluated, as detailed in the section 'Accuracy of QUO2 model-derived estimates - sensitivity to systematic errors'.

2.4.4.3. Tissue segmentation

Automated segmentation of grey matter (GM) from the anatomical scans was carried out using the FMRIB Software Library (FSL) [113]. Structural images were extracted from T_1-weighted scans using the brain extraction tool (FSL's BET). Then, a binary mask delineating the brain was created along with a probability mask of GM employing the automated segmentation tool (FSL's FAST). Both were resampled to the resolution of the functional EPI scans.

2.4.4.4. Regions Of Interest

In addition to the whole brain grey matter (GM), six ROIs in ICBM space were selected from OASIS-TRT-20 in three-dimensional mode [114]. The selected ROIs are located in parietal, occipital or temporal lobes, and are known to be implicated in conditions such as Alzheimer's disease [16,115-119]. ROI's, presented in Figure 2.1, include left and right: inferior parietal (IP), superior parietal (SP), precuneus (PRE), hippocampus (HIP), anterior (caudal and rostral) cingulate (AC) and posterior cingulate (PC). Each ROI was registered to the resolution of the functional EPI scans before being conjoined with the individual's GM probability mask excluding voxels with a GM probability lower than 50% and non-parenchymal voxels identified previously. The resultant ROI probability masks were used to perform weighted averaging of the different metrics. Voxels where no solution was found for M and OEF were excluded when performing the ROI analysis of M, OEF and $CMRO_2$.

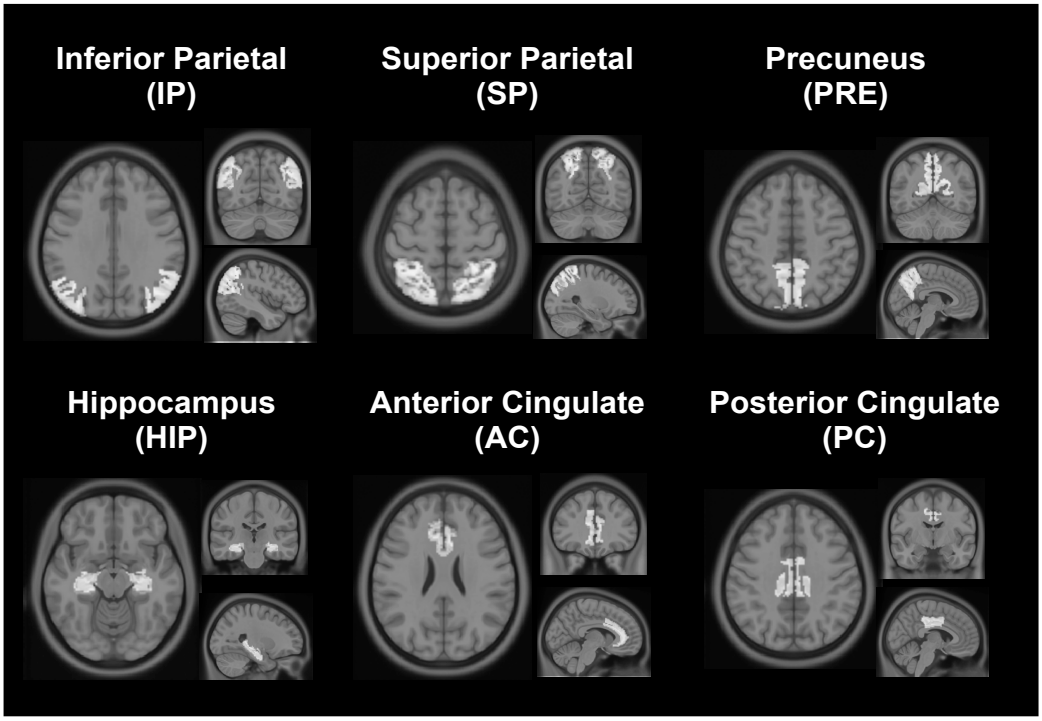

Figure 2.1. Regions of interest (ROIs)
QUO2 parameters were evaluated in GM and in six ROIs selected from the OASIS-TRT-20 atlas.

2.4.4.5. Registration

Individual BOLD, CBF, *M*, OEF and $CMRO_2$ maps were non-linearly normalized to the ICBM152 template using the CIVET software package [120] via the CBRAIN tool [121] with 12 degrees of freedom using trilinear interpolation. Test A and B average maps of BOLD and CBF were computed as arithmetic means using in-house software. On their part, average maps of *M*, OEF and $CMRO_2$ were obtained excluding from the average any voxels where no solution was found

2.4.5. Statistical Analysis

Within each measurement, i.e. CBF, BOLD (R2*), *M*, OEF and $CMRO_2$, Test A and Test B were averaged and compared across ROIs, considering $P < 0.05$ level of significance, correction for multiple comparisons.

Statistical tests were performed on the data to ensure it satisfied the criteria for conducting a reproducibility analysis. For ETO_2 and the other parameters listed above, the distribution of differences was tested for normality using the Shapiro-Wilk W-test, and the independence between the magnitude of differences and mean of measurements was verified using a rank correlation coefficient (Kendall's τ). If the differences distribution appeared to deviate from a normal distribution, or if the magnitude of differences increased with the mean of measurements, the data were transformed on the $\log_{10}$ scale and the verification was repeated. In cases where the $\log_{10}$ scaled data satisfied the criteria, the reproducibility was assessed on these scaled values. Otherwise, assessment of reproducibility was based on the original values along with appropriate annotation [122-124]. Additionally, to determine whether there was an order effect between the two tests, we performed a two-tailed paired *t*-test on each set of ROI-averaged values, considering a $P < 0.05$ level of significance.

ROI-averaged reproducibility was evaluated using Matlab to compute metrics that give complementary information on the agreement between repeated measures and population variance:

a) dSD, the standard deviation of the differences between Test A and B measurements.

b) wsSD, the within-subject standard deviation, equals dSD/√2 considering two measurements.

c) wsCV, the within-subject (or intra-subject) coefficient of variation, as used in Floyd et al. [123] and Chen et al. [125]. wsCV=√ [mean of the (wsSD/subject mean)^2]. wsCV provides an unbiased reproducibility measurement expressed as a percent of the mean with a low wsCV indicating a high reproducibility. When data were on the $\log_{10}$ scale, wsCV was approximated by 10^(wsSD)-1 [126].

d) CR, the coefficient of repeatability [127] = 1.96*√2*wsSD or 1.96*dSD. CR gives an estimate of the range of values one would obtain in a retest measurement. Thus, 95% of repeated measures for the sample will lie between the interval mean differences ± CR (α=0.05).

e) bsCV, the between-subject (or inter-subject) coefficient of variation as computed in Tjandra et al. [128]. bsCV = $SD_{pooledData}$ / $mean_{pooledData}$ * 100.

2.4.6. Accuracy of QUO2 model-derived estimates - sensitivity to systematic errors

The QUO2 derived estimates accuracy rely on assumed physiological parameters such as α, β, [Hb], as well as assumed normalized $CMRO_2$ changes during HC and HO. As sources of systematic errors, the assumed values won't affect the reproducibility/precision analysis outcomes, however they can lead to individual inaccuracy of *M*, OEF and $CMRO_2$. Using the group-averaged GM experimental Test A data, the sensitivity of QUO2 estimates to assumed parameters was evaluated by independent variation in α, β, [Hb], $CMRO2_{HC}$ and $CMRO2_{HO}$. The values used in the previous analysis were: α=0.18, β=1.5, [Hb]=15g Hb/dl blood, while isometabolism during hypercapnia and hyperoxia was considered ($CMRO2_{HC}$ and $CMRO2_{HO}$ = 1.0). Explored ranges of α and β were respectively 0.15 to 0.45 and 1.0 to 1.5, matching those in Chiarelli et al. [56]. The span of [Hb], i.e. from 11 to 17 g Hb/dl blood, was chosen as in Mark et al. [129] to take into account differences in gender and presence of anemia or polycythemia [130]. Evaluated ranges of change in $CMRO_2$ during HC and HO were determined as in Merola et al. [131]: i.e. a change of ± 1% in $CMRO_2$ for 1 mmHg and 40 mmHg change in end-tidal CO_2 and O_2 respectively. We also evaluated the impact of a maximum of 10% decrease in blood flow during HO periods, as this parameter is often assumed (normalized CBF_{HO} from 0.90 to 1.0).

2.4.7. Precision of QUO2 model-derived estimates - sensitivity to random errors

Within-subject precision of the QUO2 model-based *M*, OEF and $CMRO_2$ estimates can be affected by a certain real physiological within-subject variability as well as random errors in the measurement of brain's responses to hypercapnia and hyperoxia. To evaluate the effect, on OEF and *M* precision, of such errors in measurement, we performed an error propagation analysis of the QUO2 model, employing Test A data. In addition to the analysis of errors in measured CBF during HC, also discussed in Gauthier and Hoge [59], we examined the impact of errors in measured R2* changes during both respiratory challenges. For each observed source of error, individual OEF and *M* values were computed based on 'real' GM and respiratory measures, with simulated error ranging from -33% to +33% added to the examined

source. This simulated error can be translated into coefficient of variation of the observed input: the CV being the percent of variability with respect to the mean value, it is lower when an error is added to the measurement (CV of 20% for an error of +33%) rather than subtracted (CV of 28% for an error of -33%). Simulated group-average *M* and OEF were computed from the individual simulated values, while the latter were compared with the 'real' values to calculate the simulated CVs with respect to the added error.

2.5. Results

One participant was excluded from the analysis because their CBF response to CO_2 during Test A was found to be an outlier (value beyond twice the standard deviation). This participant reported a high level of anxiety during Test A due to a first MRI scan and hypercapnia experience.

2.5.1. Gas manipulations

At rest, the within- and between breathing rate coefficient of variation were 13% and 38% respectively. The average and standard deviation of ETO_2 levels in Test A and B are shown in Figure 2.2-A. Breathing medical air (~160 mmHg of O_2) yielded average ETO_2 levels of 111 ± 6 mmHg and 110 ± 4 for the two scan time points. During hyperoxia induction, when participants received a gas mixture with 380 mmHg of O_2, ETO_2 levels increased to 370 ± 9 mmHg during Test A and 374 ± 12 mmHg during Test B. During hypercapnia periods, participants demonstrated a slight increase in the minute volume ventilation, which increased ETO_2 levels in comparison to air-breathing (118 ± 4 and 117 ± 4 mmHg) despite a slightly lower inhaled O_2 concentration (~152 mmHg). Figure 2.2-B shows the average and standard deviation of $ETCO_2$ levels in Test A and B. $ETCO_2$ levels at baseline and during hyperoxia were found to be similar, with 40 ± 2 mmHg and 39 ± 2 mmHg (in both tests) respectively. During HC, the $ETCO_2$ levels increased to 49 ± 1 mmHg and 50 ± 2 mmHg in Test A and B respectively. Table 2.I shows, for both ETO_2 and $ETCO_2$ measurements, *P*-values of Shapiro-Wilk W-test, Kendall's rank coefficient and *t*-Student paired test, as well as wsCV and CR. All distributions of differences in tests were found to be normal (Shapiro-Wilk W-test, $P > 0.05$) and no dependence was observed between the differences in measurements and mean of

measurements (Kendall' τ, $P > 0.2$). Finally, no significant difference (*t*-Student paired test, $P > 0.1$) was found between Test A and Test B end-tidal levels, which were also reproducible (ETO_2: CR<20 mmHG, wsCV<5%; $ETCO_2$: CR<6 mmHG, wsCV<6%).

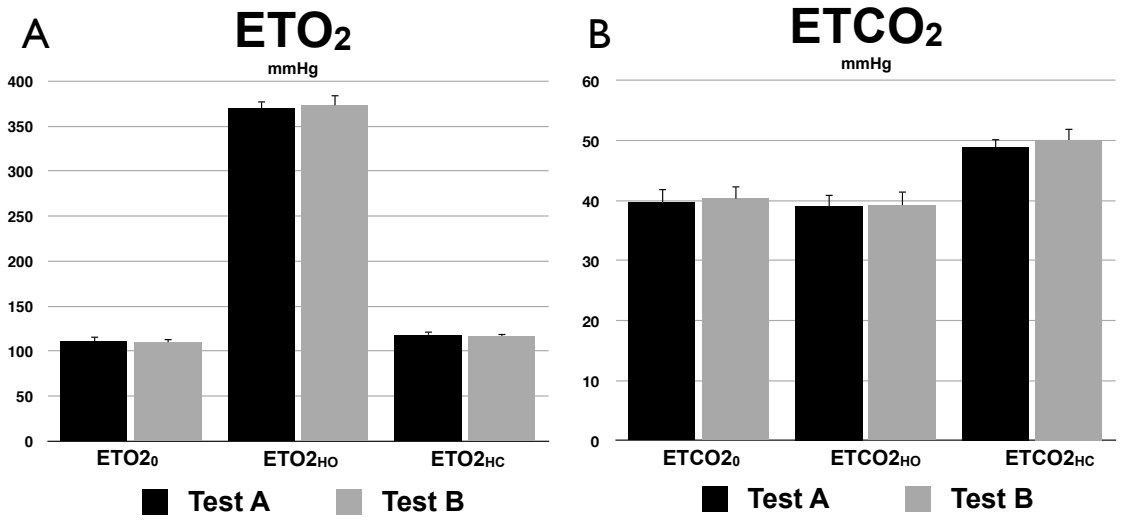

Figure 2.2. Gas manipulations
Test A and B end-tidal O_2 and CO_2 values at baseline (0), during hyperoxia (HO) and during hypercapnia (HC). Errors bars indicate standard deviation.

	$ETO2_0$	$ETO2_{HO}$	$ETO2_{HC}$	$ETCO2_0$	$ETCO2_{HO}$	$ETCO2_{HC}$
Test A mean ± SD	111 ± 6	370 ± 9	118 ± 4	40 ± 2	39 ± 2	49 ± 1
Test B mean ± SD	110 ± 4	374 ± 12	117 ± 4	40 ± 2	39 ± 2	50 ± 2
All mean ± SD	111 ± 5	372 ± 10	118 ± 4	40 ± 2	39 ± 2	50 ± 2
Shapiro-Wilk	*P*=0.38	*P*=0.24	*P*=0.25	*P*=0.05	*P*=0.3	*P*=0.08
Kendall's τ	*P*=0.38	*P*=0.24	*P*=1.00	*P*=0.38	*P*=0.56	*P*=0.38
Paired t-test	*P*=0.73	*P*=0.39	*P*=0.51	*P*=0.58	*P*=0.83	*P*=0.1
CR	13	19	10	5	3	4
wsCV	4.4%	1.9%	3.0%	5.0%	3.2%	2.6%

Table 2.I. End-tidal measurements
Group-averaged ± SD of end-tidal values are presented, followed by Shapiro-Wilk, Kendall's τ and paired *t*-test *P* value. Coefficient of repeatability (CR) and within-subject coefficient of variation (wsCV) are also shown.

2.5.2. Exclusion of non-parenchymal or artifact voxels

Figure 2.3 shows sagittal group-averaged maps of voxels excluded from the ROI analysis given that they were considered as non-parenchymal or dominated by susceptibility artifacts, based on individual $\Delta R2^*_{HC}$, $\Delta R2^*_{HO}$ and $T_2^*_0$. Both tests presented similar patterns of excluded voxels, and, as expected, the latter were mainly situated in regions adjacent to the nasal cavity due to the paramagnetic effect of molecular O_2. In Table 2.II, we present, for each ROI, the group average and standard deviation of the number of voxels with GM probability higher than 0.5, preceding and following the exclusion process. No significant difference was found between Test A and Test B number of pre- and post-exclusion voxels (all $P > 0.23$). In whole GM, 24 ± 4% were excluded from the analysis. The hippocampus and the anterior cingulate were the most affected by the procedure, with a percentage of exclusion of 31 ± 10% and 30 ± 9% respectively, whereas less than 2% of voxels were excluded in the other regions.

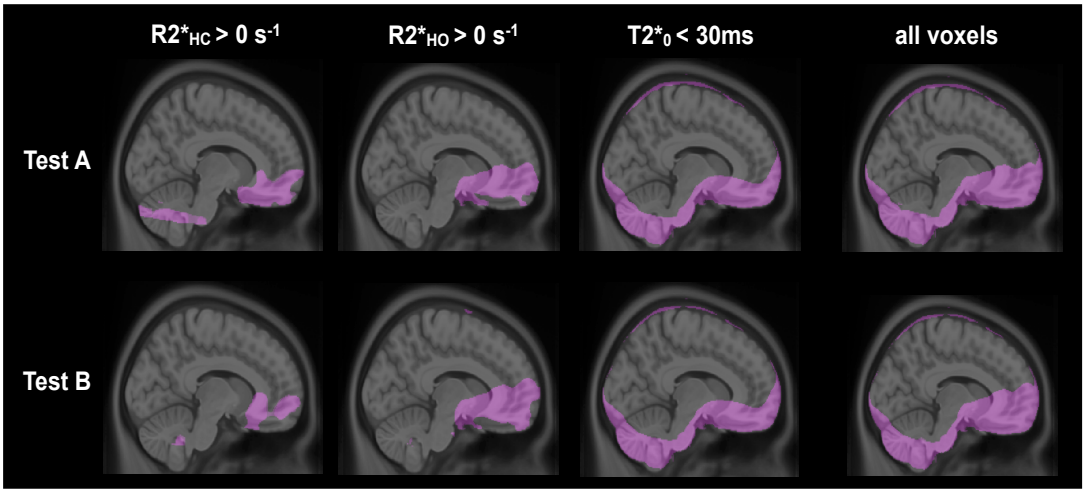

Figure 2.3. Exclusion of non-parenchymal or artifact voxels
For both tests, voxels considered as non-parenchymal or affected by susceptibility artifacts based on individual $\Delta R2^*_{HC}$, $\Delta R2^*_{HO}$ and $T_2^*_0$ are shown overlapping a sagittal slice of the ICBM template. The latest column presents the overall excluded voxels in each test.

	GM	IP	SP	PRE	HIP	AC	PC
Number of voxels pre-exclusion							
Test A mean ± SD	5676 ± 550	234 ± 33	197 ± 32	168 ± 33	79 ± 11	88 ± 21	59 ± 14
Test B mean ± SD	5715 ± 541	226 ± 21	204 ± 20	167 ± 23	78 ± 12	88 ± 15	53 ± 10
Paired t-test	*P*=0.35	*P*=0.26	*P*=0.30	*P*=0.90	*P*=0.55	*P*=0.95	*P*=0.25

Number of voxels post-exclusion							
Test A mean ± SD	4331 ± 567	233 ± 33	193 ± 26	166 ± 32	54 ± 7	63 ± 23	59 ± 14
Test B mean ± SD	4316 ± 561	225 ± 22	200 ± 16	167 ± 23	53 ± 10	62 ± 16	53 ± 10
Paired t-test	*P*=0.74	*P*=0.23	*P*=0.28	*P*=0.92	*P*=0.84	*P*=0.93	*P*=0.25
Percent of excluded voxels (%)							
	24 ± 4	0.58 ± 0.91	1.81 ± 2.37	0.60 ± 0.73	31 ± 10	30 ± 9	0.00 ± 0.00

Table 2.II. Exclusion of non-parenchymal or artifact voxels
Group-averaged ± SD of the number of voxels in each ROI are presented before and after the voxels exclusion procedure. Paired *t*-test *P* values between Test A and Test B number of voxels as well as percentage of voxels excluded are also shown.

2.5.3. T_1 shortening

Estimates of arterial blood T_1 during HO were found to be 1.558 ± 0.004 sec for Test A and 1.556 ± 0.006 sec for Test B, with no significant difference between them (paired *t*-test, $P = 0.39$). Computation of GM-averaged post-T_1-correction $\Delta\%CBF_{HO}$ resulted in 0.4 ± 4.5% for Test A and -2.8 ± 3.3% for Test B. No significant difference (paired *t*-test, $P = 0.25$) was found between them and both were not significantly different from zero ($P > 0.07$).

2.5.4. Detection rate of solutions in ROI

The percentage of voxels where a solution was found for *M* and OEF were computed for each individual and test. The results, presented in the Table 2.III, show no significant difference between Test A and Test B ($P > 0.21$) and all detection rates were above 87% besides in HIP where the detection rare were 78%. These percentages are based on the number of voxels after exclusion of non-parenchymal and artifact voxels found in the Table 2.II.

	GM	IP	SP	PRE	HIP	AC	PC
Test A	89 ± 5	95 ± 4	97 ± 3	93 ± 9	78 ± 11	87 ± 11	100 ± 1
Test B	88 ± 7	92 ± 10	95 ± 6	91 ± 11	78 ± 13	94 ± 5	99 ± 2
Paired t-test	*P*=0.86	*P*=0.53	*P*=0.56	*P*=0.73	*P*=0.99	*P*=0.21	*P*=0.25

Table 2.III. Detection rate of solutions in ROI (%)
Group-averaged ± SD of the percentage of voxels where a solution was found for *M* and OEF are shown in each ROI. Paired *t*-test *P* values between Test A and Test B detection rate are also shown.

2.5.5. Test and retest group-averaged metrics across ROIs

A summary of the dual-echo pCASL and QUO2 ROI-averaged metrics is presented in Figure 2.4. For each combination of metric and ROI, we present the group average of Test A, Test B and of both tests. Resting CBF, O_2 delivery and resting R2* displayed the highest group-averaged test-retest reproducibility. Resting R2* presented the lowest population variance in both tests. Resting CBF and O_2 delivery, due to their direct relation, showed a similar pattern of values across ROIs. Similarly for M and $\Delta R2^*_{HC}$, given that QUO2 M values are very sensitive to change in R2* and CBF during HC while nearly insensitive to change during HO (as later demonstrated in the "Precision of group GM-averaged values – sensitivity to random errors" section). A larger decrease in R2* (higher BOLD increase) was observed during HC than during HO in every ROIs. Although every metrics, but OEF, showed a certain tendency of heterogeneous values across ROIs, all differences were not found statistically significant, as presented in the following section.

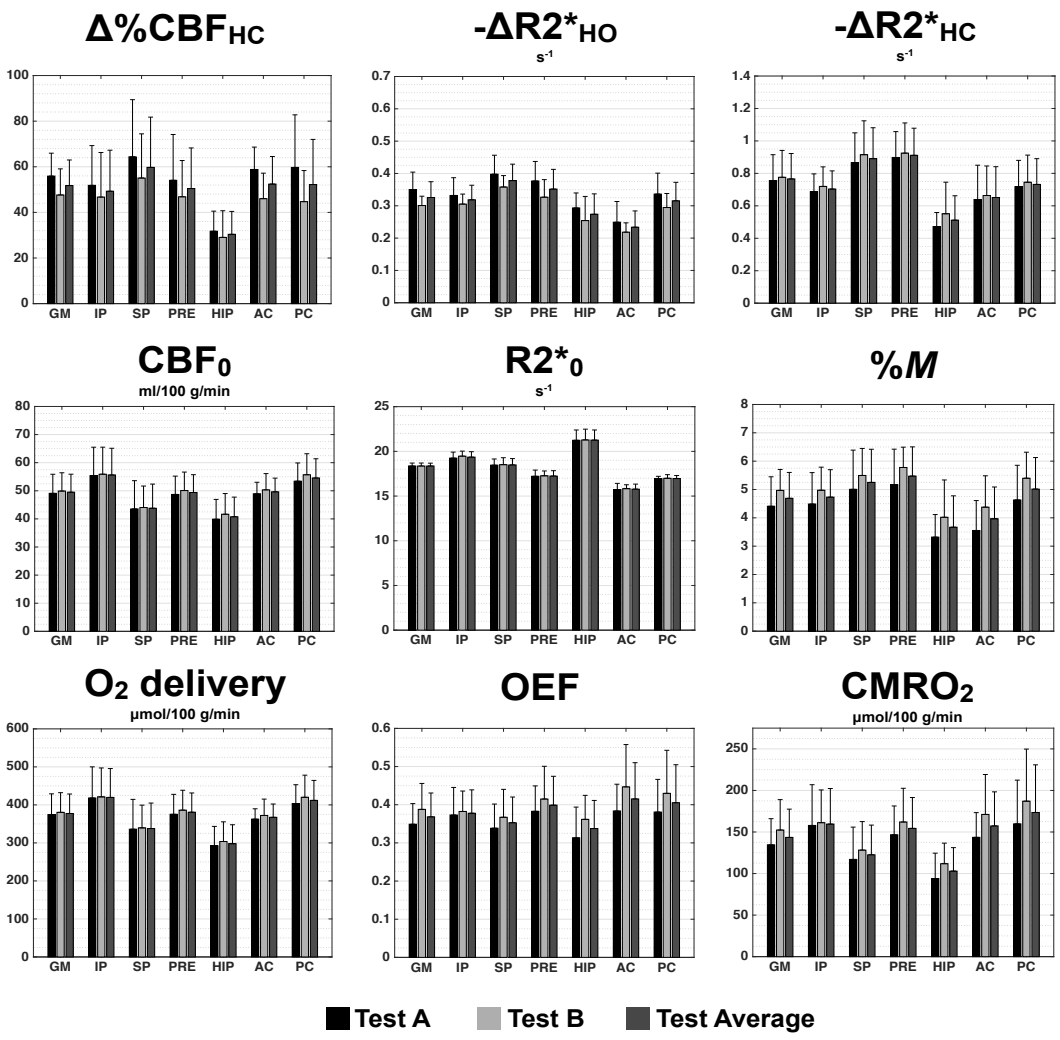

Figure 2.4. Test and retest group-averaged metrics across ROIs
ROI-averaged of Test A, Test B and all tests averaged are presented with standard deviation.

2.5.6. Comparison of all tests averaged between ROIs

Data from all subjects and tests were averaged and compared across ROIs. Figure 2.5 shows where a significant difference ($P < 0.05$) was found between two ROIs, after correction for multiple comparisons. No statistical significant difference was found in fractional CBF change to HC across ROIs, except in the HYP, were the smallest change was found. R2* change to HO was found to be the smallest in AC among all ROIs except compared to HYP values, whereas the smallest R2* change to HC was found in HYP. Due to its low population

variance within ROI, resting R2* presented values generally significantly different across ROIs. On the contrary, OEF were found to have consistent values across ROIs ($P > 0.2$).

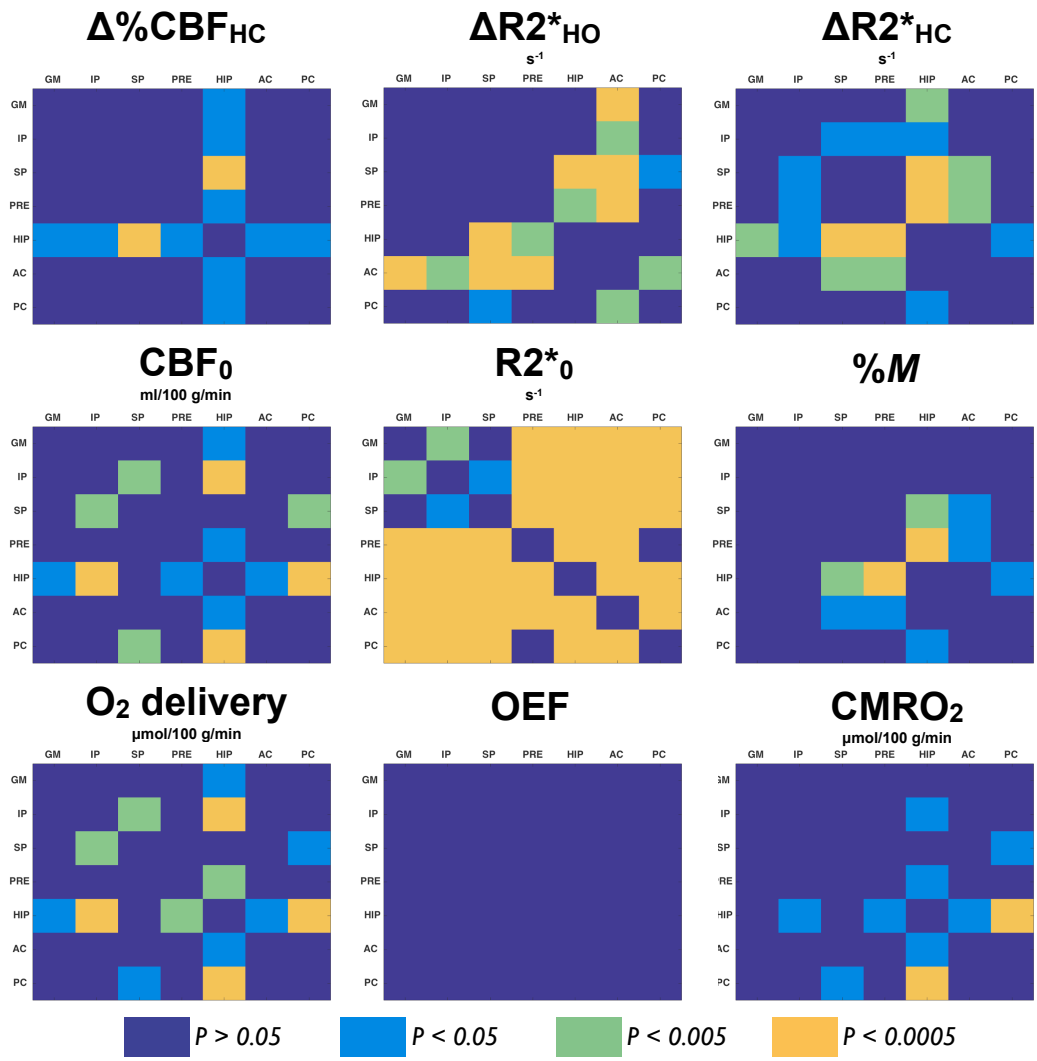

Figure 2.5. Comparison of all tests averaged between ROIs

For each metric, group average of all subjects and tests was compared across ROIs. Colors code for limits in P values after correction for multiple comparisons: dark blue indicates absence of significant difference ($P > 0.05$), while light blue ($P < 0.05$), green ($P < 0.005$) and orange ($P < 0.0005$) illustrate a significant difference between two ROIs (designed in the X and Y axis).

2.5.7. ROI reproducibility analysis

In Table 2.IV, we report the reproducibility analysis of the dual-echo pCASL and QUO2 measurements in each ROI, more precisely, the *P*-value of Kendall's τ, Shapiro-Wilk and paired *t*-test, the CR and wsCV. Shapiro-Wilk and Kendall's τ test detected, for a certain combination of metric-ROI, if the distribution deviated from normality (condition *a* in Table 2.IV) and if there was a dependency between the differences in measurements and the mean of measurements (condition *b* in Table 2.IV) respectively. In all cases, a $\log_{10}$ transformation of the data resulted in the satisfaction of both conditions (reproducibility of transformed data is presented in boldface) except for $\Delta\%CBF_{HC}$ in AC which distribution deviated from normality after the transformation (reproducibility of original data is presented in italic boldface). Paired *t*-tests detected no significant difference between Test A and Test B ($P > 0.07$), except for %*M* in AC ($P < 0.001$), OEF in HIP ($P < 0.03$) and $CMRO_2$ in HIP ($P < 0.05$).

	GM	IP	SP	PRE	HIP	AC	PC
Average volume							
Mean ± SD, cm^3 >50% prob. GM	394 ± 49	20.9 ± 2.5	17.9 ± 1.9	15.2 ± 2.4	4.9 ± 0.8	5.7 ± 1.8	5.1 ± 1.1
$\Delta\%CBF_{HC}$							
Shapiro-Wilk	*P*=0.56	*P*=0.19	*P*=0.04[a]	*P*=0.58	*P*=0.78	*P*=0.03[a]	*P*=0.007[a]
Kendall's τ	*P*=0.77	*P*=0.77	*P*=0.14	*P*=0.38	*P*=0.24	*P*=0.56	*P*=0.24
Paired t-test	*P*=0.19	*P*=0.45	*P*=0.43	*P*=0.51	*P*=0.68	*P*=0.08	*P*=0.23
CR	31.1	32.1	0.4	51.6	30.4	*38.8*	0.5
wsCV	22.4%	25.9%	35.6%	35.8%	40.3%	*26.5%*	46.9%
$\Delta R2^*_{HO}$							
Shapiro-Wilk	*P*=0.21	*P*=0.51	*P*=0.02[a]	*P*=0.49	*P*=0.65	*P*=0.46	*P*=0.93
Kendall's τ	*P*=0.24	*P*=0.03[b]	*P*=0.24	*P*=1.00	*P*=0.14	*P*=0.07	*P*=0.77
Paired t-test	*P*=0.08	*P*=0.41	*P*=0.18	*P*=0.17	*P*=0.20	*P*=0.21	*P*=0.22
CR	0.15	0.21	0.17	0.18	0.15	0.12	0.17
wsCV	16.0%	18.9%	15.3%	18.9%	19.2%	17.4%	19.3%
$\Delta R2^*_{HC}$							
Shapiro-Wilk	*P*=0.57	*P*=0.40	*P*=0.47	*P*=0.05	*P*=0.21	*P*=0.16	*P*=0.02[a]
Kendall's τ	*P*=0.56	*P*=1.00	*P*=0.56	*P*=0.77	*P*=0.03[b]	*P*=0.77	*P*=1.00
Paired t-test	*P*=0.49	*P*=0.35	*P*=0.13	*P*=0.49	*P*=0.12	*P*=0.54	*P*=0.37
CR	0.14	0.17	0.16	0.18	0.18	0.19	0.08
wsCV	6.70%	8.93%	7.43%	8.09%	16.10%	11.00%	6.93%
CBF_e mL/100 g/min							
Shapiro-Wilk	*P*=0.90	*P*=0.25	*P*=0.93	*P*=0.07	*P*=0.80	*P*=0.45	*P*=0.39
Kendall's τ	*P*=1.00	*P*=0.56	*P*=0.56	*P*=0.07	*P*=1.00	*P*=0.14	*P*=0.56
Paired t-test	*P*=0.48	*P*=0.66	*P*=0.77	*P*=0.37	*P*=0.13	*P*=0.50	*P*=0.31
CR	5.4	5.5	7.9	7.4	6.0	9.8	10.9
wsCV	3.88%	3.38%	6.50%	5.32%	5.23%	6.99%	7.45%
$R2^*_0$							
Shapiro-Wilk	*P*=0.45	*P*=0.10	*P*=0.64	*P*=0.19	*P*=0.32	*P*=0.46	*P*=0.55
Kendall's τ	*P*=1.00	*P*=0.77	*P*=0.07	*P*=0.38	*P*=0.14	*P*=1.00	*P*=1.00
Paired t-test	*P*=0.91	*P*=0.07	*P*=0.65	*P*=0.42	*P*=0.85	*P*=0.36	*P*=0.52
CR	0.17	0.65	0.55	0.33	0.94	0.56	0.45
wsCV	0.33%	1.24%	1.05%	0.70%	1.54%	1.30%	0.96%
%*M*							

Shapiro-Wilk	*P*=0.04[a]	*P*=0.31	*P*=0.05[a]	*P*=0.91	*P*=0.20	*P*=0.08	*P*=0.22
Kendall's τ	*P*=1.00	*P*=0.24	*P*=0.38	*P*=0.77	*P*=0.77	*P*=0.77	*P*=1.00
Paired t-test	*P*=0.11	*P*=0.19	*P*=0.28	*P*=0.23	*P*=0.12	*P*=0.0006[c]	*P*=0.10
CR	0.19	1.84	0.22	2.50	2.32	1.72	2.42
wsCV	16.8%	16.6%	20.2%	18.1%	21.5%	16.7%	19.1%
O2deliv µmol/100 g/min							
Shapiro-Wilk	*P*=0.86	*P*=0.27	*P*=0.76	*P*=0.16	*P*=0.29	*P*=0.75	*P*=0.42
Kendall's τ	*P*=1.00	*P*=1.00	*P*=0.56	*P*=0.14	*P*=1.00	*P*=0.24	*P*=0.56
Paired t-test	*P*=0.49	*P*=0.77	*P*=0.79	*P*=0.37	*P*=0.21	*P*=0.52	*P*=0.34
CR	41	44	59	58	46	71	83
wsCV	3.87%	3.63%	6.29%	5.35%	5.36%	6.75%	7.43%
OEF							
Shapiro-Wilk	*P*=0.12	*P*=0.03[a]	*P*=0.75	*P*=0.19	*P*=0.32	*P*=0.09	*P*=0.21
Kendall's τ	*P*=0.38	*P*=0.24	*P*=1.00	*P*=0.24	*P*=0.56	*P*=1.00	*P*=0.77
Paired t-test	*P*=0.15	*P*=0.76	*P*=0.41	*P*=0.35	*P*=0.02[c]	*P*=0.13	*P*=0.37
CR	0.14	0.16	0.16	0.16	0.12	0.21	0.26
wsCV	13.6%	14.1%	16.5%	14.7%	14.7%	18.2%	23.0%
$CMRO_2$ µmol/100 g/min							
Shapiro-Wilk	*P*=0.47	*P*=0.47	*P*=0.58	*P*=0.07	*P*=0.55	*P*=0.36	*P*=0.26
Kendall's τ	*P*=0.56	*P*=0.03[b]	*P*=0.03[b]	*P*=0.24	*P*=0.77	*P*=0.56	*P*=1.00
Paired t-test	*P*=0.15	*P*=0.80	*P*=0.51	*P*=0.36	*P*=0.05[c]	*P*=0.10	*P*=0.30
CR	62	0.16	0.25	80	50	88	128
wsCV	15.2%	14.0%	23.3%	17.9%	20.6%	18.9%	26.7%

Table 2.IV. Reproducibility of QUO2 measurements in different ROI

P value of Shapiro-Wilk, Kendall's τ, paired t-test, coefficient of repeatability (CR) and within-subject coefficient of variation (wsCV) are presented. When conditions described in footnote a or b were present, data were log10 transformed and the conditions were evaluated once again. If the conditions were then satisfied, the reproducibility metrics were computed on the transformed data (results presented in boldface). Otherwise, the reproducibility metrics were computed on the original data (results presented in italic boldface).

[a] The distribution of difference in measurements deviated from normality.

[b] A significant dependency between difference in measurements and mean of measurements was detected.

[c] A significant difference between Test A and Test B was detected.

Figure 2.6 compares individual-subject reproducibility (wsCV) with the population variance (bsCV) of QUO2 measurements in each ROI. Among all ROIs, the measurement that showed lower inter- and intra-subject variability was resting R2* (wsCV < 2%; bsCV < 5.5%). CBF_0 and O_2 delivery come next, with a low individual-subject reproducibility (ROI-averaged wsCV = 5.5%) compared to the population variance (ROI-averaged bsCV = 14.6%), meaning the latter cannot be explained by poor reproducibility of the technique. It is also an indication of reproducible estimate of arterial O_2 content. $\Delta R2_{HC}$ was also found to have a considerably higher intra-subject consistency than across subjects (ROI-averaged wsCV = 9.3%; ROI-averaged bsCV = 22.3%), as opposition to $\Delta R2_{HO}$ (ROI-averaged wsCV = 17.9%;

ROI-averaged bsCV = 17.5%). The highest inter- and intra-subject variability was found in $\Delta\%CBF_{HC}$ ($wsCV_{GM}$ = 22.4%; $wsCV_{allROI}$ = [22.4%, 46.9%]; $bsCV_{GM}$ = 21.6%; $bsCV_{allROI}$ = [21.6%, 37.9%]). As for the QUO2 estimated measurements *M*, OEF and $CMRO_2$, their wsCV in GM were found to be lower than 17% and they ranged from 13% to 27% across all ROIs. Their variability across subjects was higher by a factor of 1.3 in average across ROIs. Values averaged over GM were found to have the lowest inter- and intra-subject variability among regional averages (mean wsCV of 11.0 ± 7.4%; mean bsCV of 16.15 ± 6.55%). Variability in smaller regions, i.e. HIP and PC, was generally found higher, although no significant correlation between ROI volume and variability was found, except for resting R2* measurements (Pearson correlation coefficient R_2=-0.76, P = 0.048).

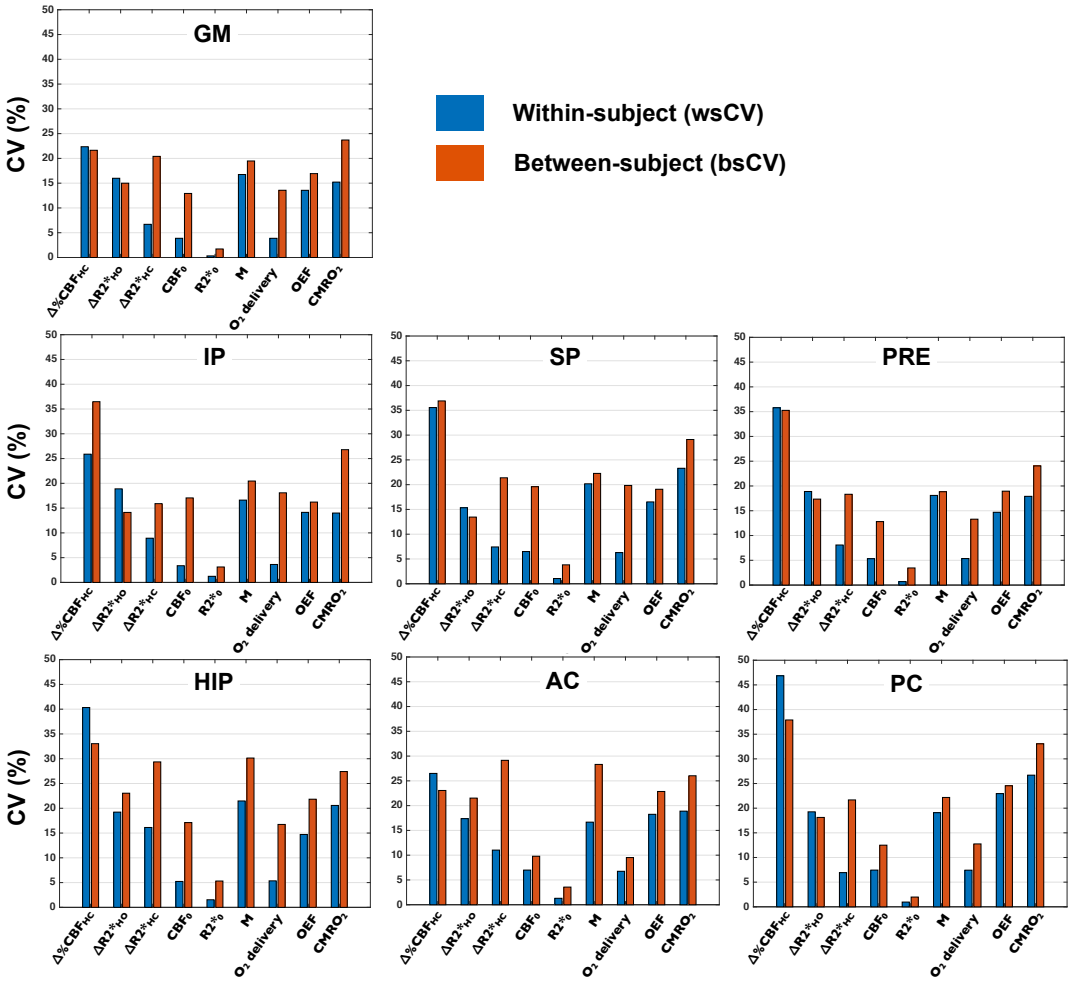

Figure 2.6. ROI analysis of within- and between-subject reproducibility

Within each ROI, are shown the within- and between-subject coefficient of variation (respectively wsCV (blue) and bsCV (red)) for each metric.

Test-retest correlation plots for each metric across the different ROIs can be found in Figure 2.7. For each individual, Test A against Test B measurements is shown, with colors coding for the different ROIs. For each metric, a linear regression model with zero intercept was applied on the data. The computed coefficient of determination (R^2) is displayed in each graph. In each measurement, the regression line that fit the data is shown in solid grey. Values lying in the vicinity of the identity line (solid black line) indicate a good reproducibility of the measurements. Among all quantities, resting R2*, resting CBF, O_2 delivery and $\Delta R2^*_{HC}$ present the best reproducibility, whereas $\Delta\%CBF_{HC}$, $\Delta R2^*_{HO}$, $\%M$, OEF and $CMRO_2$ show a larger scattering of the data around the identity line.

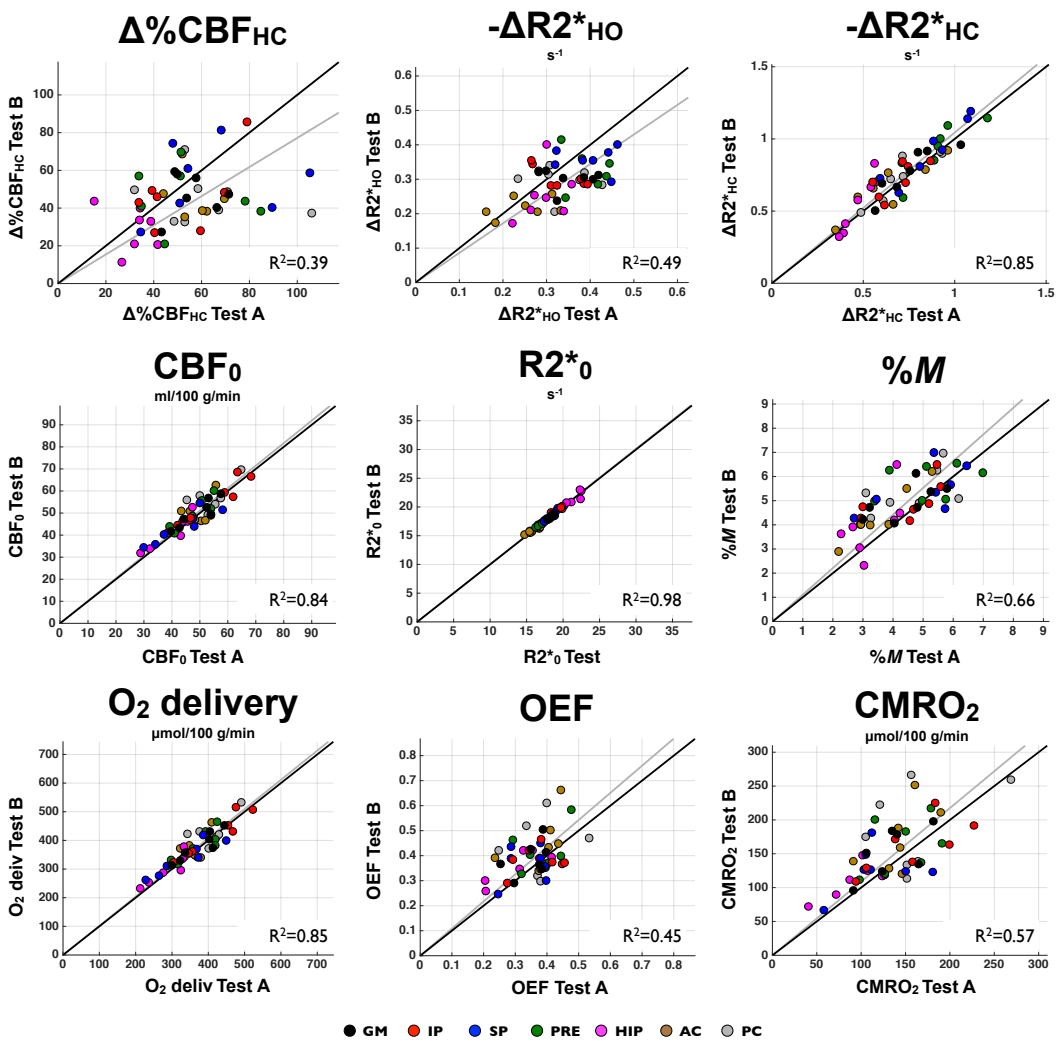

Figure 2.7. ROI analysis of individual reproducibility - Correlation plots
For each measurement, individual Test A against Test B ROI-averaged is plotted. Values close to the identity line (solid black line) indicate a good reproducibility. For each metric, a linear regression with zero intercept was performed on the data. The resulted coefficient of detection (R^2) and the fit to the data (grey line) are presented.

An additional illustration of reproducibility is offered by Bland-Altman plots for each measurement, as shown in Figure 2.8. The individual mean of measurements against the difference in measurements is plotted, with colors coding for the different ROIs. For each ROI, a solid line represents mean of difference, whereas dashed lines depict the confidence intervals (i.e. mean difference ± CR). We can observe a trend toward higher variability in

smaller regions (HIP, AC, and PC) compared to larger regions, a finding that is to be expected based on statistical considerations.

.

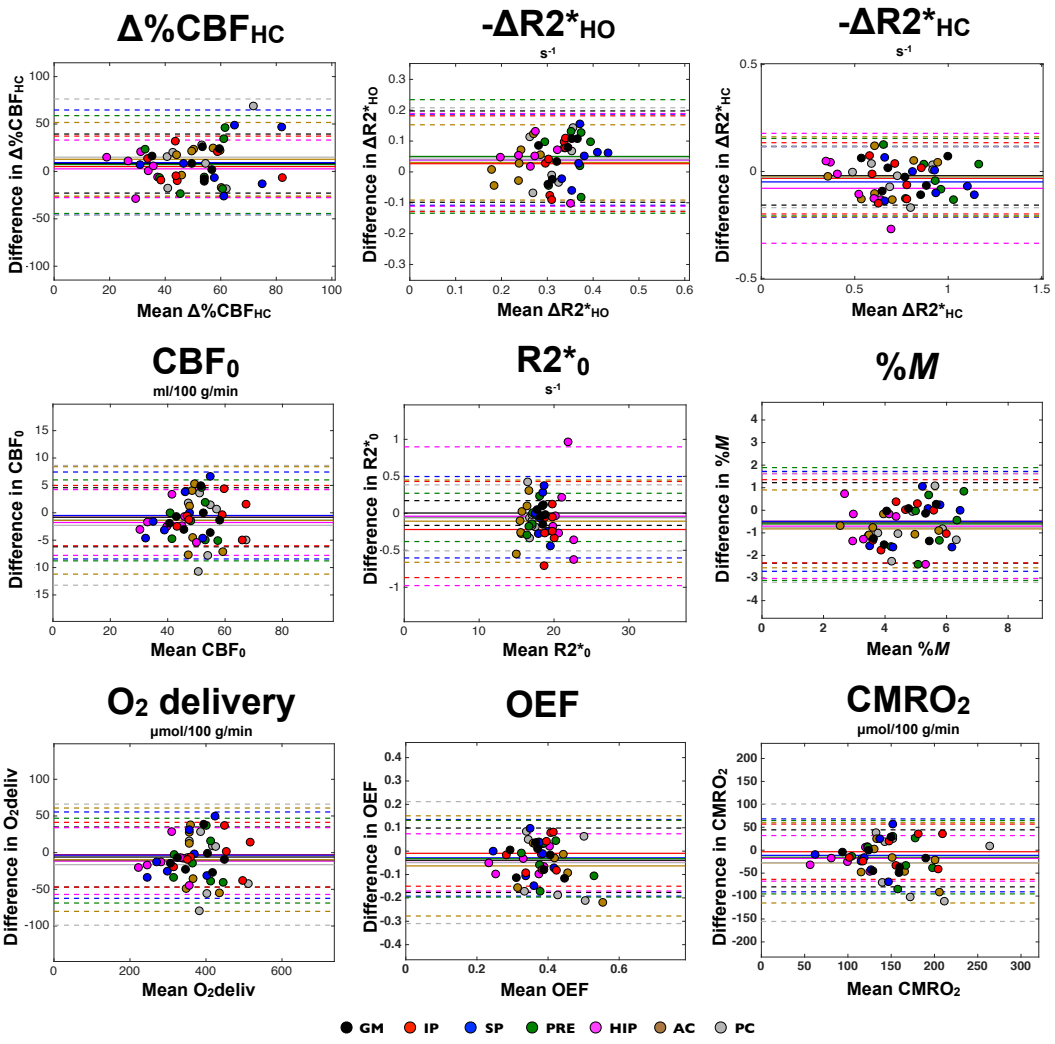

Figure 2.8. ROI analysis of individual reproducibility - Bland-Altman graphs
For each measurement, the difference in sessions against the mean is displayed. Within each ROI, a solid line represents the mean difference between measurements. The dashed lines represent the ROI-averaged limits of agreement (mean ± 1.96 * dSD i.e. mean ± coefficient of repeatability (CR)) indicating that 95% of repeated measures will fall in between them.

2.5.8. Parametric maps

In Figure 2.9, we show group-average Test A and B maps of the different measurements. One axial and one sagittal slice of the ICBM152 template are shown. The group-average maps generally demonstrate good qualitative agreement between test and retest, with the main exception being $\Delta\%CBF_{HC}$. Figure 2.10 shows OEF and *M* maps in individual subjects, for Tests A and B, as well as group average and standard deviation maps. One axial slice of the ICBM152 template is shown. The subject count maps indicate, at each voxel, the number of subject included in the group average, given that voxels with no solution found for OEF and *M* were excluded from the average. Individual OEF and *M* maps generated using the optimized QUO2 present little random fluctuation in values and very few voxels with no solution. Group average maps for both parameters were qualitatively very similar in appearance, although differences between Tests A and B are noted in individual subjects.

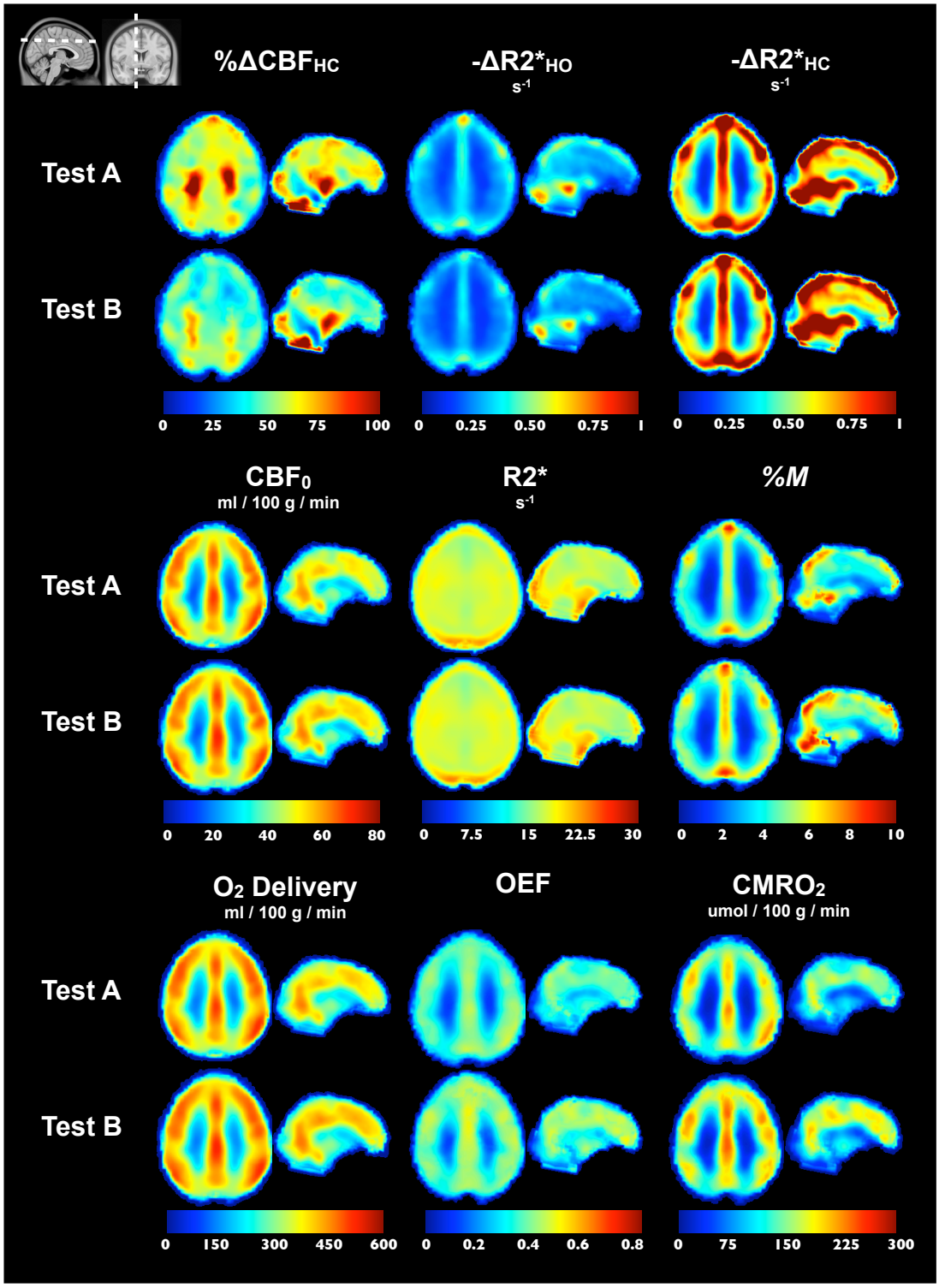

Figure 2.9. Group maps
For each metric, Test A and B group maps are shown in one axial and one sagittal slice. Maps were non-linearly registered to ICBM152 before being averaged. *M*, OEF and $CMRO_2$ maps were averaged using an approach where non-solution voxels were excluded from the average.

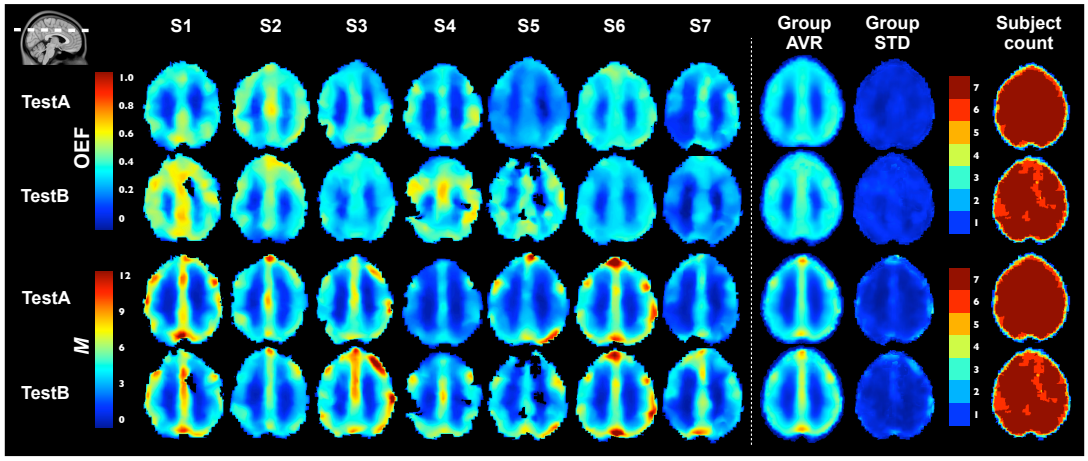

Figure 2.10. Individual OEF and *M* maps
Test A and B individual OEF and *M* maps are shown in one axial slice of ICBM152 template. Followed maps are the group average, the standard deviation, and the subject count maps. The latter maps indicate at each voxel the number of subjects where a solution was found for OEF and *M*, meaning they were part of the group average.

2.5.9. Accuracy of group GM-averaged values - sensitivity to systematic errors

Sensitivity of the model to systematic errors resulting from the assumed parameters is summarized in Figure 2.11. Based on our Test A group-averaged changes in ET during each respiratory manipulation, our evaluated ranges of percent change in metabolism were ±10% and ±7% in HC and HO respectively. Effects of the assumed α, β, [Hb], $CMRO2_{HC}$, $CMRO2_{HO}$ and CBF_{HO} on the HC and HO curves are presented (Figures 2.11- A1 to A6 respectively), followed by resultant estimates of *M*, OEF and $CMRO_2$ (Figures 2.11- B1, B2 and B3 respectively). The β and $CMRO2_{HC}$ assumed values are the principal sources of variation in *M*, while variations in [Hb], $CMRO2_{HO}$ and CBF_{HO} yield almost no change to the estimate. Figures 2.11- A5 and A6 show that, by not affecting the HC curve, variations in metabolism and blood flow during HO shift the HO curve on the nearly horizontal section of the HC curve, resulting in almost no alteration in *M* solution. The assumption of change in $CMRO_2$ during HO is the principal sources of variation in OEF, especially if a decrease in metabolism is considered ($0.93 < CMRO2_{HO} < 1.0$). Furthermore, OEF is similarly sensible to variation in [Hb], $CMRO2_{HC}$ and $CBF_{HO,}$ while presenting almost no change as a variation in

β. Both *M* and OEF are similarly influenced by a variation in α. The used value of 0.18 for α results in an *M* and OEF of 5.0% and 0.39 respectively, while if α is changed to the commonly adopted values of 0.38, the calculated *M* and OEF values become 5.6% and 0.44. Estimate of metabolism being the product of resting CBF by OEF and arterial O_2 content, a certain percent increase/decrease in OEF leads to the same percent increase/decrease in $CMRO_2$ with the exception where [Hb] is varied, given that it leads to a change in the arterial O_2 content in the opposite direction as in OEF.

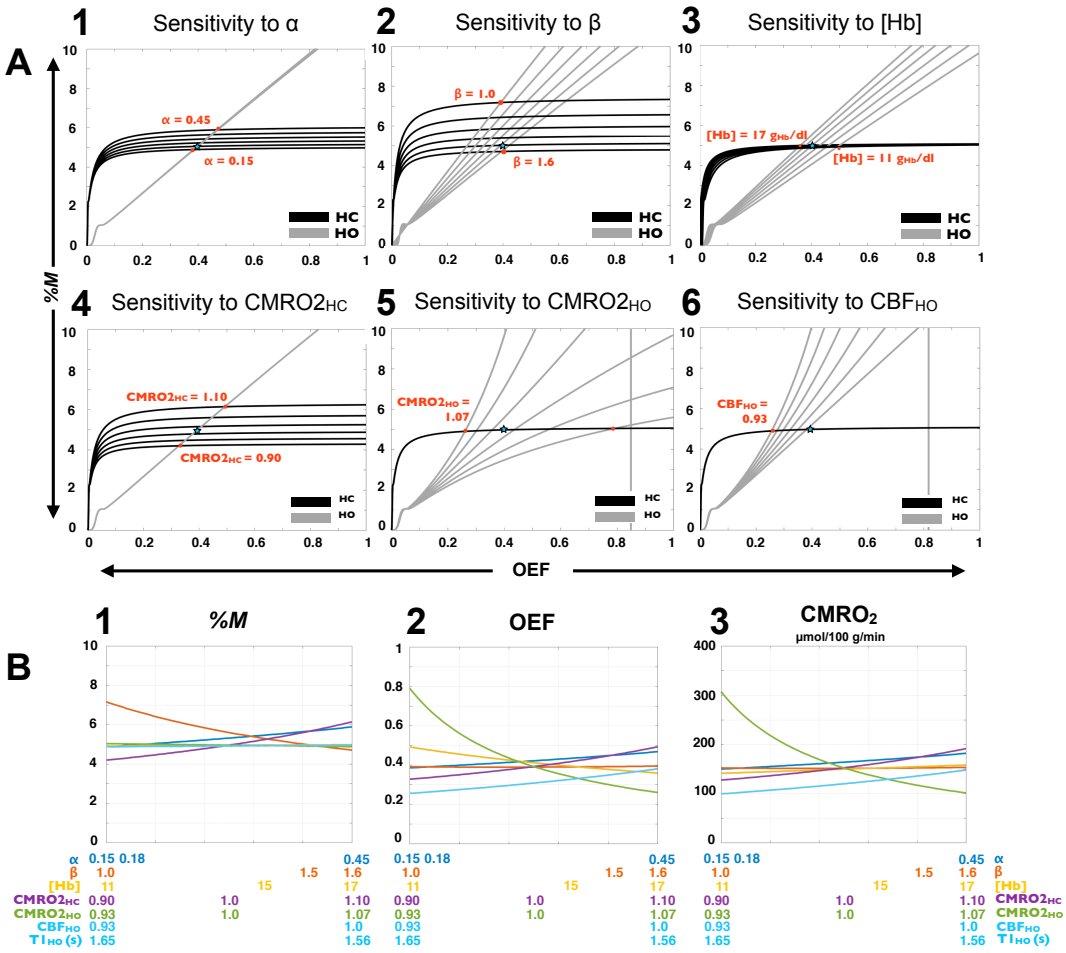

Figure 2.11. Accuracy of group GM-averaged values - sensitivity to systematic errors
Observed effects, on *M*, OEF and $CMRO_2$ estimates, of the assumed QUO2 parameters, are summarized. Estimates were based on group-averaged Test A de-PCASL measurements in GM and ETO_2 ('true' values), while the assumed parameters α, β, [Hb], normalized change in $CMRO_2$ due to HC ($CMRO2_{HC}$) and HO ($CMRO2_{HO}$), as well as normalized change in CBF during HO (CBF_{HO}) were varied independently. The HC and HO curves resulting from the

use of six different values of α, β, [Hb], $CMRO2_{HC}$, $CMRO2_{HO}$ and CBF_{HO} are presented (A1 to A6 respectively). Each red dot represents the HC and HO curves intersection (hence one *M* and OEF solution) when either one of the extremity in the observed range is in use. The remaining *M* and OEF solutions lie on a line connecting both red dots and passing by the subsequent intersections. *M*, OEF and $CMRO_2$ estimates are presented as a function of each varied parameter (B1, B2 and B3 respectively, ranges mentioned below each plot). Below the CBF_{HO} range is shown the corresponding range of blood T_1 during HO. The original values employed in this study were α = 0.18, β = 1.5, [Hb] = 15 g Hb/dl blood, $CMRO2_{HC}$ = 1 (isometabolic hypercapnia), $CMRO2_{HO}$ = 1 (isometabolic hyperoxia), while our post-T_1-correction group-averaged normalized CBF_{HO} in Test A was estimated to be 1 (i.e. no CBF change during HO). Resulted 'true' group-averaged Test A *M*, OEF and $CMRO_2$ estimates in GM were 4.96%, 0.39 and 152 μmol/100 g/min respectively (shown by the blue stars).

2.5.10. Precision of group GM-averaged values - sensitivity to random errors

Sensitivity of *M* and OEF to random errors in BOLD and CBF measurements is summarized in Figure 2.12. Given that neither resting CBF nor arterial O_2 content are varied here, the relative impacts of errors in BOLD and CBF responses measurements on $CMRO_2$ and OEF are equivalent. Therefore, estimates and variation of $CMRO_2$ are not shown. Effect of errors in CBF_{HC}, $R2^*_{HC}$ and $R2^*_{HO}$ on HC and HO curves are presented in Figures 2.12-A1, A2 and A3 respectively. Errors in CBF_{HC} or $R2^*_{HC}$ affect both *M* and OEF estimates, whereas errors in $R2^*_{HO}$, by shifting the HO curve on the nearly horizontal section of the HC curve, result in almost no alteration in *M* solution. OEF and *M* estimates as a function of percent errors or variability of measurement are shown in Figures 2.12- B1 and B2 respectively. Figure 2.12-B1 exhibits a nearly linear increase in OEF errors as each of the input's error increases. Figure 2.12-B2 presents the same observation for *M* estimates, with the exception mentioned above where errors in $R2^*_{HO}$ have almost no noticeable effect. The direction of the effect on OEF and *M* estimates depend of the source of error: an underestimated $R2^*_{HC}$ will lead to an underestimated OEF or *M*, whereas if overestimated, OEF and *M* will also be overestimated. On the other hand, CBF_{HC} have the opposite effect on OEF and *M* as well as $R2^*_{HO}$ on OEF. Figures 2.12- C1 and C2 show resulted variability of OEF and *M* estimates respectively. We observe that for the same percent error, CBF_{HC} will

induce a lower variability in OEF than R2*, and a lower variability in *M* than $R2^*_{HC}$. However, it is known that one of the limiting factors of such calibrated MRI methods is the low signal-to-noise ratio of ASL measurements, which is more susceptible to induce higher errors than in BOLD measurements. Figure 2.12-C brings our attention to the fact that the test-retest variability found in our experimental CBF_{HC} (wsCV=22%) and $R2^*_{HO}$ (wsCV=16%) data, likely contributed to a minimum of 10% variability in our *M* and OEF estimates.

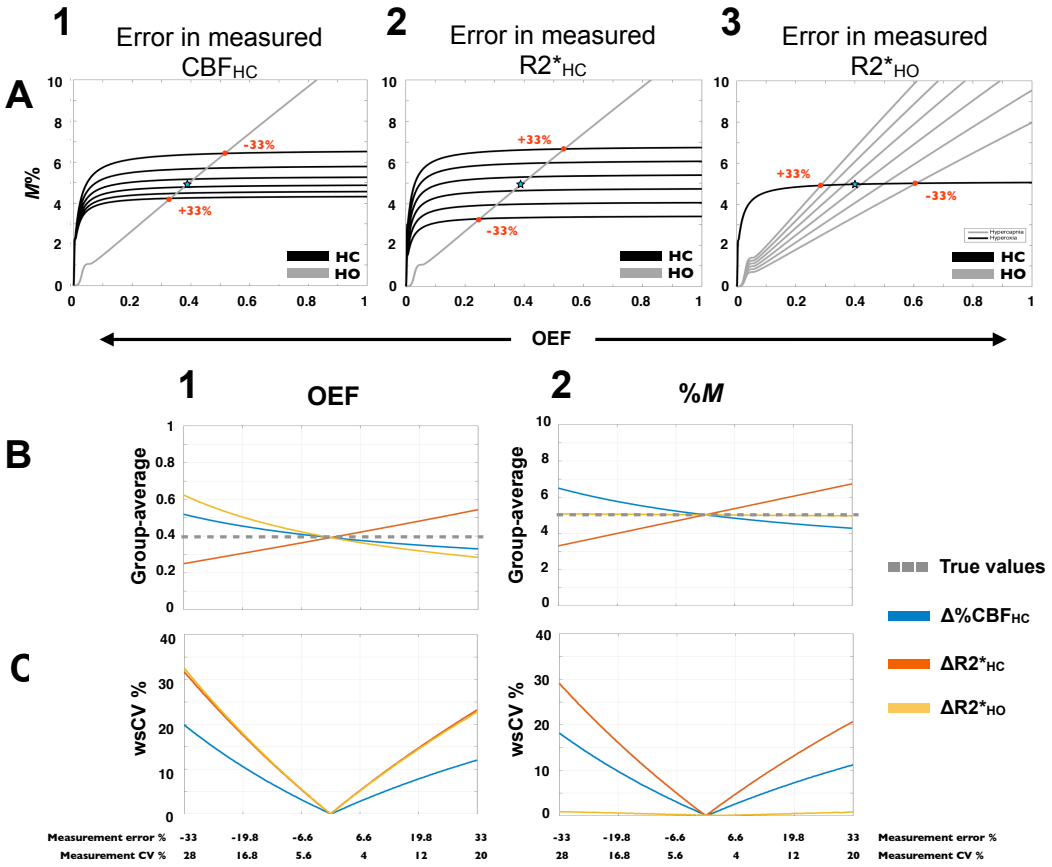

Figure 2.12. Precision of group GM-averaged values - sensitivity to random errors
Observed effects, on *M* and OEF estimates, of error in BOLD and CBF measurements, are summarized. Estimates were based on group-averaged Test A de-PCASL measurements in GM and ETO_2 ('true' values), while a simulated error was added to each observed input independently. Evaluated error ranged from -33% to 33%, which is equivalent to a maximum measurement CV of 28% (when underestimated) and 20% (when overestimated). The hypercapnia (HC) and hyperoxia (HO) curves resulting from six different errors in CBF_{HC}, $BOLD_{HC}$ and $BOLD_{HO}$ are shown (A1, A2 and A3 respectively). Each red dot represents the HC and HO curves intersection (hence one *M* and OEF solution) when either one of the extremity in the observed range is in use. The remaining *M* and OEF solutions lie on a line

connecting both red dots and passing by the subsequent intersections. OEF and *M* estimates (B1 and B2 respectively) in addition to CV between simulated and 'true' OEF/*M* values (C1 and C2) were computed for each source of error (colored lines). Without addition of error in measurements, 'true' group-averaged Test A *M* and OEF estimates were 4.96% and 0.39 respectively (shown by the blue stars and the perforated grey lines).

2.6. Discussion

We have characterized the inter- and intra-subject variability of the estimated *M*, OEF and absolute $CMRO_2$ derived from the optimized QUO2 approach, which is a crucial step in the development and clinical application of this MRI technique for the quantitative measurement of oxygen delivery and consumption in the human brain. A visual inspection of the individual maps of *M* and OEF revealed a larger stability of values and fewer regions with no solution than the individual maps presented in the initial proof-of-concept of the QUO2 model [65].

We obtained physiologically plausible tests-averaged *M*, OEF and $CMRO_2$ estimates in GM that were compared to those in literature summarized in Table 2.V. Variability among different studies in estimated values can arise from: the imaging technique employed, the type of breathing manipulations, the values of the assumed parameters, and the strategy employed to define the grey-matter region. Our *M* average of 4.69 ± 0.91% falls in the low end of reported values, although this may be mainly due to a more aggressive exclusion of large venous voxels. Our OEF and $CMRO_2$ of 0.37 ± 0.06 and 144 ± 34 μmol/100 g/min respectively fall within the reported range of values.

Study	*M* (%)	Study	OEF	CMRO2 μmol/100 g/min
Bulte et al. (2009) [132]	5.3	**Xu et al. (2009) [103]**		158**
Ances et al. (2008) [133]	5.7	**Bolar et al. (2011) [63]**	0.26 ± 0.02	125 ± 15
Gauthier and Hoge (2012) [65]	6.0	**Gauthier and Hoge (2012) [65]**	0.35 ± 0.04	145 ± 30
Ances et al. (2009) [96]	6.5	**Lu and Ge (2008) [102]**	0.35 ± 0.06	
Mark et al. (2011) [129]	6.5-9.7	**Jain et al. (2010) [104]**	0.35 ± 0.01	123 ± 4
Chen and Parrish (2009) [134]	6.7	**Van Zijl et al. (1998) [139]**	0.36	137
Wise et al. (2013) [106]	6.9-9.2	**Wise et al. (2013) [106]**	0.42 - 0.50	184±45-222±82
Chiarelli et al. (2007) [56]	7.0	**Coles et al. (2006) [140]**	0.38 ± 0.68	130 ± 24**
Ances et al. (2009) [96]	7.3	**Leenders et al. (1990) [100]**	0.38	155*
Bulte et al. (2012) [64]	8.5	**Bulte et al. (2012) [64]**	0.38 ± 0.14	155 ± 39
Gauthier et al. (2011) [135]	9.5	**Bremmer et al. (2010) [141]**	0.43 ± 0.63	120 ± 8
Lin et al. (2008) [136]	10.5	**Ibaraki et al. (2010) [23]**	0.43	137*

Leontiev and Buxton (2007) [137]	11.1	**Ito et al. (2004) [142]**	0.44 ± 0.06	129 ± 20
Perthen et al. (2008) [138]	11.6			

Table 2.V. Literature values of *M*, OEF and resting $CMRO_2$
The majority of M values were taken from Gauthier et al. [135]. All are values at 3 T, adjusted to TE=30ms.
Pet studies are identified with a light grey background.
* Extrapolated value to match our mean age of 30 years old.
** Corrected value for the ratio of $CMRO_2$ and mass between GM and WM [106].

2.6.1. Regional inter- and intra-subject reproducibility

Our individual-subject reproducibility in every parameters was found to be lower than our population variance, as also reported in previous study [128,137,143], except for our CBF response to HC and BOLD response to HO. Inter- and intra-subject variability of QUO2 measurements was found to be the lowest when averaged throughout all GM, with general trends toward higher CVs when averaged over smaller regions, a findings consistent with previous studies [143,144]. Based on statistical consideration, averaging an estimate across a relatively large region is likely to yield less variability than when averaging across a small section of the brain. Although we observed a certain trend toward higher variability in smaller regions, our results showed no significant correlation between ROI volume and variability except for R2* measurements. The most intra-subject reproducible measurements was CBF_0, along with O_2 delivery and $R2^*_0$. Our regional CBF_0 wsCV were comparable to that reported by Wang et al. [144].

To our knowledge, reproducibility of OEF and absolute $CMRO_2$ estimated from combined HC and HO calibrated BOLD technique has not been characterized in studies so far published. On the other hand, variability of *M* calibration parameter and relative change in $CMRO_2$ were studied. In a small area of the visual cortex, Leontiev and Buxton [137] evaluated the intra-subject variability in *M*, CBF and BOLD responses to HC employing a different CV computation. Adjusting our CV computation to theirs, we obtain a similar wsCV for *M* of 13% in GM (compared to 12.3%) and a lower variability in $BOLD_{HC}$ and CBF_{HC} with 7% vs. 26.1 and 20% vs. 40.6% respectively. They reported the presence of an important leak in the CO_2 delivery during day 2 for two of their participants, thus increasing their intra-subject variability in BOLD and CBF responses to HC. In another study at 7 Tesla, using a simultaneous hypercapnia-hyperoxia (carbogen) gas-breathing challenge, Krieger et al. [143]

detected more intra-subject variability in their *M* value and BOLD changes to carbogen than what we found (wsCV≃34% vs. wsCV<17%) while they reported less variable CBF changes to carbogen than our CBF changes during HC (wsCV≃9% vs. wsCV=22%). The difference among variability in *M*, CBF and BOLD changes to gas may arise from the different choice of MRI acquisition and gas challenge.

Studies employing dynamic ^{15}O PET as a direct measure of OEF and $CMRO_2$ have reported lower intra-subject variability in OEF and $CMRO_2$. Coles et al. [140] reported a whole brain test-retest coefficient of variation of 4.6% and 3.7% for OEF and $CMRO_2$ respectively, while Bremmer et al. [141] obtained a variability of 8.8%, 9.3% and 5.3% for CBF_0, OEF and $CMRO_2$ in GM respectively. In our study, resting CBF in GM varied less (wsCV=3.9%) while OEF and $CMRO_2$ had a higher degree of variability (13.6% and 15.2% respectively). Higher intra-subject variability in QUO2 estimates than PET estimates may arise partly from a larger noise accumulation in QUO2 techniques as an indirect measure of OEF and $CMRO_2$.

2.6.2. Accuracy of group GM-averaged values - sensitivity to systematic errors

The QUO2 sensitivity to assumed physiological parameters α, β, [Hb], $CMRO2_{HC}$, $CMRO2_{HO}$ and CBF_{HO} was examined. Recently, Wise et al. employed a Bayesian estimation framework in order to estimate α and β [106]. Merola et al. [131] presented a simplified calibration model that substitute the standard α and β parameters with a single one and yielded improved estimates of OEF. Accuracy of estimates is likely to benefit from those calibration techniques where α and β are automatically estimated. Individual OEF estimates can also benefit from a simple blood test to determine the hemoglobin concentration. Isometabolism during hypercapnia and hyperoxia remains of a debate to date. Some studies suggest that $CMRO_2$ does not change with HC [69,78,79] while others report an increase [80], or a decrease [81,82]. Similarly, heterogeneous results are found with regard to metabolism alteration during hyperoxia [83]. Without a clear consensus on the matter, we opted to preserve the assumption of no change in $CMRO_2$ during both respiratory manipulations.

We have reported a certain variation in OEF (and $CMRO_2$) as a function of reduction in blood flow caused by the hyperoxia manipulation. It is common to assume a fixed T_1-corrected CBF_{HO} for every subjects, for example Bulte et al. assumed a blood flow decrease of 4% during periods of hyperoxia at 50% O_2 [64,84], or, as in the initial proof-of-concept of the QUO2 model, to compute the group-averaged measured CBF_{HO} after T_1-correction and use it for every subject. In the present study, we obtained physiologically plausible arterial blood T_1 values (1.56 sec at 60% O_2, consistent with 1.49 sec at 95% O_2 [145]) and post-T_1-correction CBF_{HO} in GM. The latter was used as an individual basis, hence capturing any intra-subject variation between test and re-test blood flow decrease during HO. When correcting for T_1 shortening during HO, rat blood was used as a surrogate for human blood which is justified since they both possess similar blood constitution, are likely to have very similar longitudinal relaxivity to molecular oxygen relationship and to experience similar physiological responses to hyperoxia.

2.6.3. Precision of group GM-averaged values - sensitivity to random errors

The error propagation analysis highlighted how the precision in QUO2 estimates was affected by random errors in the measurements of CBF and BOLD responses to the respiratory challenges. Especially, considering the same range of error, BOLD had a larger impact on QUO2 precision than CBF. However in practice, CBF response to HC is more challenging and carries a bigger uncertainty due to the low contrast-to-noise ratio. The range of error observed (-33% to +33%) is likely to approach the order of error in measured CBF_{HC} while a lower uncertainty is expected in BOLD measurement, yielding smaller effects on QUO2 precision errors. It is therefore believed that the principal limitation in the QUO2 M, OEF and $CMRO_2$ intra-subject reproducibility remains the error in CBF responses. Although the exact contribution of the measurements errors compared to the intrinsic day-to-day physiological variability could be further studied with a within-session test-retest reproducibility design, the present study offers clinically relevant assessment of variability in QUO2 measurements for follow-up studies.

2.6.4. QUO2 qualitative individual and group maps reproducibility

As expected, the reproducibility of QUO2 parameter estimates was generally improved with more extensive averaging of voxels and subjects. While group average maps demonstrated qualitatively good reproducibility, it was found that physiological and measurement noise still limits reproducibility of voxel values at the individual subject level.

2.6.5. Potential QUO2 accuracy and precision improvement

There are other potential avenues to improve the accuracy and precision of functional ASL. One strategy may include the use of a higher magnetic field, which would increase the SNR by increasing spin polarization and the T_1 relaxation time of arterial blood. The gain in SNR might be partly lost due to an increase in physiological noise, however, this effect could be diminished by applying a denoising technique like RETROICOR [146,147]. Improved control for magnetization transfer effects is another mechanism for improving accuracy [148]. Additional approaches may also enhance accuracy and reproducibility of QUO2 measurements by correcting for region-specific variations in tag arrival times [149-151], for drops in label efficiency [152,153], for partial volume [154] and hemodynamic response delays [155]. Benefits may also be offered by improved imaging readout methods such as the use of a 3D imaging readout [156], multiband excitation [157] and background suppression [158-160].

Additional factors that can influence accuracy and precision of measurements in such calibrated approaches are the inhaled concentrations of oxygen and carbon dioxide. A higher O_2 and CO_2 concentration would yield BOLD changes closer to the M value to be extrapolated, reducing measurement errors. Furthermore, higher CO_2 concentration would have the advantage of increasing the contrast-to-noise ratio due to higher CBF changes. However, administration of high levels of O_2 and CO_2 introduce potential problems: higher O_2 concentration can complicate the quantification of CBF due to blood T_1 reduction and susceptibility artifacts in areas close to sinuses and airways, while higher levels of CO_2 can lead to anxiety and potentially alter brain physiology in ways other than the intended vasodilatory effect [161,162]. Future studies should assess the effect of oxygen and carbon dioxide concentration in reproducibility of quantitative calibrated methods such as QUO2. An

investigation on the effect of O_2 concentration in QUO2 estimates is presently in process, comparing 60% vs. 100% O_2 during hyperoxia periods (manuscript in preparation).

The imaging parameters of the de-pCASL used in the present study were adjusted to optimize the detection rate of CBF responses in GM while acquiring whole-brain image with a minimal gap between slices. In order to allow the labeled blood bolus to arrive in the tissue of the imaged region, a post labeling delay (PLD) is employed. In our 2D acquisition, the first and last slices are acquired after a delay of 900 msec and 1986 msec respectively, resulting in an brain-averaged PLD of 1443 msec which is shorter than that recommended in the ASL white paper [112]. The latter recommends a 3D readout PLD of 1800 msec for healthy subjects of age below 70 years old. MacIntosh et al. [149] evaluated the regional arterial transit time (ATT) in a cohort of healthy participants with an age range equivalent to that of our group. Among the temporal, parietal, frontal and occipital lobes, only the latter was reported to have a mean ATT (935 ± 0.108ms) slightly higher than our nominal PLD (900 msec), but lower than the acquisition time of our second slice (953 msec). Although our choice of PLD might not be optimal in lower occipital region of certain healthy participants, we believe that in the large majority of cases, the acquired ASL signal was accurately reflecting CBF and that an increase in our PLD would have resulted in a loss in SNR, especially during hypercapnia where the ATT is known to diminish.

Small cohort sizes like 8 have been common in recent years, particularly for complex fMRI protocols with greater physiological specificity than the classic BOLD contrast. Although our conclusion are limited by the relatively small sample size, we felt that this regional analysis of inter- and intra-subject variability of the QUO2 estimates in such a cohort remains of interest.

In conclusion, the variability of the optimized QUO2 estimates across subjects and the intra-subject reproducibility of estimates in different brain regions were characterized while the impact of errors on the accuracy and precision of such estimates was determined. These results will help guide power analyses for research applications as well as future developments aimed at further improving the reproducibility of the QUO2 method.

2.7. Acknowledgments

The authors would like to thank Scott Nugent, Marius Tuznik, Bahare Sabouri, Carollyn Hurst and André Cyr for their excellent technical assistance and insightful discussions. Jiongjiong Wang at UCLA is acknowledged for providing the pseudo-continuous arterial spin-labeling sequence. This study was supported by the Canadian Institutes of Health Research (MOP 123492), Canada Foundation for Innovation (17380), Natural Sciences and Engineering Research Council of Canada (R0018142), Fonds Québécois de la Recherche sur la Nature et les Technologies (FQRNT), and the Consortium québécois sur la découverte du médicament (CQDM). The funders had no role in study design, data collection and analysis, decision to publish, or preparation of the manuscript.

3. The Impact of Inspired Oxygen Levels on Calibrated fMRI Measurements of *M*, OEF and Resting $CMRO_2$ using Combined Hypercapnia and Hyperoxia

Authors: Isabelle Lajoie, Felipe B. Tancredi, Richard D. Hoge

Authors contributions: Study design and Software development: IL FBT RDH; Data acquisition: IL FBT; Formal analysis and Data interpretation: IL; Writing original draft and Visualization/Data presentation: IL; Project administration and Funding acquisition: RDH.

Status: Published in the journal *PLoS ONE*. 2017; 12(3): e0174932.

3.1. Preface

The precision and accuracy of QUO2 *M*, OEF and $CMRO_2$ estimates may be impacted by the level of O_2 and CO_2 provided during the respective hyperoxia and hypercapnic manipulations. In a preliminary phase of the present thesis, different concentrations of CO_2

were tested on a population of healthy volunteers, and it was concluded that 5% of CO_2 was high enough to yield sufficient responses, while low enough to keep the level of comfort adequate for a majority of the participants (data not shown). On the other hand, the impact of the inspired O_2 levels remained unclear. The O_2 level employed in QUO2 will have a direct influence on the end-tidal O_2, BOLD and CBF responses, in addition to potentially yielding a change in the O_2 metabolism, although the later assumption remains a debate in the literature [83]. In addition to these direct effects, there are more subtle factors that may play an important role in the precision and accuracy of the model-derived estimates. First, a high concentration of O_2, by bringing the BOLD response to the maximum *M* value, may reduce the error associated with the later estimate, and thus that of OEF and $CMRO_2$. However, an increased amount of paramagnetic O_2 in the airways may induce a larger pattern of susceptibility artifact, reducing the number of voxels with valid estimates. Finally, the high HO manipulation, by inducing a larger shortening in the arterial blood T_1 [87-89], the accurate correction of blood changes becomes more important, potentially impacting the accuracy of OEF and $CMRO_2$ as seen in Chapter 2. In the present Chapter 3, we explore these above impacts of the O_2 concentration in calibrated fMRI, and ensure, via a simulation, that the QUO2 model adequately accounts for the individual effects of O_2 levels on end-tidal O_2, CBF and BOLD responses.

3.2. Abstract

Recent calibrated fMRI techniques using combined hypercapnia and hyperoxia allow the mapping of resting cerebral metabolic rate of oxygen ($CMRO_2$) in absolute units, oxygen extraction fraction (OEF) and calibration parameter *M* (maximum BOLD). The adoption of such technique necessitates knowledge about the precision and accuracy of the model-derived parameters. One of the factors that may impact the precision and accuracy is the level of oxygen provided during periods of hyperoxia (HO). A high level of oxygen may bring the BOLD responses closer to the maximum *M* value, and hence reduce the error associated with the *M* interpolation. However, an increased concentration of paramagnetic oxygen in the inhaled air may result in a larger susceptibility area around the frontal sinuses and nasal cavity. Additionally, a higher O_2 level may generate a larger arterial blood T_1 shortening, which

require a bigger cerebral blood flow (CBF) T_1 correction. To evaluate the impact of inspired oxygen levels on *M*, OEF and $CMRO_2$ estimates, a cohort of six healthy adults underwent two different protocols: one where 60% of O_2 was administered during HO (low HO or LHO) and one where 100% O_2 was administered (high HO or HHO). The QUantitative O2 (QUO2) MRI approach was employed, where CBF and R2* are simultaneously acquired during periods of hypercapnia (HC) and hyperoxia, using a clinical 3 T scanner. Scan sessions were repeated to assess repeatability of results at the different O_2 levels. Our T_1 values during periods of hyperoxia were estimated based on an empirical ex-vivo relationship between T_1 and the arterial partial pressure of O_2. As expected, our T_1 estimates revealed a larger T_1 shortening in arterial blood when administering 100% O_2 relative to 60% O_2 (T_{1LHO} = 1.56±0.01 sec vs. T_{1HHO} = 1.47±0.01 sec, $P < 4*10^{-13}$). In regard to the susceptibility artifacts, the patterns and number of affected voxels were comparable irrespective of the O_2 concentration. Finally, the model-derived estimates were consistent regardless of the HO levels, indicating that the different effects are adequately accounted for within the model.

Key-words: Calibrated fMRI; Cerebral oxidative metabolism; Inspired oxygen levels; T_1 shortening; Susceptibility artifacts; Repeatability; Reproducibility

3.3. Introduction

Recently, different groups have proposed that resting cerebral metabolic rate of O_2 consumption ($CMRO_2$) can be imaged using gas-based fMRI techniques [64,85,106]. Our team presented an approach, dubbed QUantitative O_2 (QUO2) based on respiratory calibration of the BOLD signal, using hypercapnia (HC), and hyperoxia (HO). During the gas manipulation, end-tidal O_2 (ETO_2) and CO_2 ($ETCO_2$) levels are constantly monitored and a dual-echo version of pseudo-continuous Arterial Spin Labeling (de-pCASL) is used to measure BOLD and cerebral blood flow (CBF) simultaneously. ETO_2, BOLD and CBF then serve as inputs to the generalized calibration model (GCM) described in Gauthier and Hoge [59], which yields a system of two equations with solutions for the BOLD calibration parameter *M*, i.e. the maximum BOLD signal increase when venous O_2 saturation approaches 100%, and resting oxygen extraction fraction (OEF). The multiplication of OEF by baseline CBF and arterial O_2 content (estimated from ETO_2 monitoring and, optionally, blood testing)

gives the estimated resting $CMRO_2$ in micromoles of oxygen extracted from the cerebral vasculature per minute, per 100g of tissue.

While the initial proof-of-concept of the method produced reliable results when spatially averaged within the brain and over multiple subjects, it suffered from a single-subject instability characterized by large fluctuations in the modeled values and a considerable lack of solution in certain regions [85]. In order to be considered a reliable method for within-subject longitudinal studies, there was a need to improve the single-subject image quality. Additionally, prior to being able to draw conclusion about differences in resting oxidative metabolism between populations or between states of a disease, knowledge about the precision and accuracy of the model-derived estimates was crucial. The breathing circuit and image analysis strategy were updated in previous work [66,163]. The repeatability of the respiratory responses as well as CBF and BOLD responses within grey matter (GM) has also been assessed [67]. Finally, the question of methodological precision was evaluated by assessing the regional intra- and inter-subject variability of QUO2 derived estimates [163].

The choice of O_2 and CO_2 concentration during respective periods of HO and HC may also have an impact on the accuracy and precision of QUO2 derived estimates, which remains to be assessed. Higher CO_2 concentration would have the advantage of increasing the image contrast-to-noise ratio due to higher CBF responses, however it can lead to anxiety and potentially alter brain physiology in ways other than the intended vasodilatory effect [161,162]. In a preliminary phase, it was agreed that the commonly employed 5% CO_2 during HC blocks was low enough to preserve participant's comfort, while high enough to yield significant cerebrovascular responses. As for the O_2 concentration, compared to slight HO levels (e.g. 50-60%), more extreme levels of HO may bring the BOLD responses closer to the maximum M value, therefore diminishing the measurement errors while increasing the SNR. However, due to the paramagnetic characteristic of oxygen molecule, the measured signal may be prone to more prominent susceptibility artifacts patterns in vulnerable regions such as the frontal sinuses and nasal cavity [86], thus yielding inaccurate or non-solution values in those regions. An additional potential impact of the O_2 concentration arises when changes in blood flow during HO are encompassed in the model, such as in the generalized calibrated model. Following a low HO level, CBF responses may be smaller than the inherent noise level of

ASL acquisitions, making its measurement challenging. Furthermore, a decrease in CBF during periods of HO may reflect a combination of phenomena: a vasoconstrictive effect following a hyperventilation-induced decrease in $ETCO_2$ [164], a vasoconstriction due to increased O_2 per se, and an acceleration of arterial blood longitudinal relaxation (T_1 shortening) caused by the increase of dissolved molecular oxygen in blood plasma [87-89]. If not taken into account, this T_1 decay in arterial blood leads to an overestimation of CBF decrease during HO. As a consequence of those complications, it is common to assume a fixed, pre-determined CBF decrease [56,64,84,165]. However, assuming a fixed CBF decrease contributes to the systematic errors and can affect the accuracy and repeatability of OEF and $CMRO_2$ estimates as reported in Lajoie et al. [163]. Therefore, the application of a T_1-correction on the measured CBF during HO is advocated.

Additionally, in theory, the QUO2-derived estimates should not depend on the level of hyperoxia induced, since the model is designed to account for this. In a previous study [163], the within-subject repeatability of the model-derived estimates was assessed based on very small variations of ETO_2 during periods of 60% O_2 hyperoxia. The effectiveness of the QUO2 model to obtain reproducible M, OEF and $CMRO_2$ despite considerable variations in hyperoxia ETO_2 is crucial and remains to be demonstrated.

The present study aims at exploring, in a small cohort of healthy individuals, the impact mentioned above, on QUO2 calibrated fMRI estimates, when providing 100% O_2 during periods of HO instead of the previously provided 60% O_2, in addition to verifying the reproducibility of results regardless of the inspired oxygen levels.

3.4. Materials and Methods

From the group of eight healthy adults that underwent the 24 hour QUO2 test-retest study mentioned previously [163], six of them repeated the experiment, but this time, instead of being given 60% O_2 during periods of HO (referred to as “lower HO levels protocol” (LHO)), the participants were given 100% O_2 (“higher HO levels protocol” (HHO)). Each HO protocol was repeated to assess repeatability of results at the different O_2 levels (referred to as “Test A” and “Test B”). To minimize effects of diurnal fluctuation in blood flow [107], all sessions were acquired between 2 PM and 6 PM. The participants were asked to abstain from

caffeine 3 hours prior to scanning. All participants (3 females and 3 males, mean age: 30.5 ± 6.7 years) gave written informed consent and the project was approved by the Comité mixte d'éthique de la recherche du Regroupement Neuroimagerie/Québec.

3.4.1. Respiratory Paradigm

A gas timing schedule previously described by Bulte et al. [64], with a total duration of 18 minutes, was applied, as in [163]. This involves two 2-min periods of hypercapnia (HC) and two 3-min periods of hyperoxia (HO), induced by administering gas mixtures enriched with CO_2 and O_2 respectively. Hypercapnia was followed by a 1-min normocapnic period and then the 3-min hyperoxic stimulus. Hyperoxia was followed by a 3-min period of normoxia. Periods of normocapnia and normoxia were long enough to ensure a return to baseline as shown by the CBF and BOLD time course in Tancredi et al, Figure 3 [67]. Participants inhaled the gas mixtures via a breathing circuit developed in-house [66]. During the first test-retest experiment [163], the hyperoxia periods were induced with the subjects breathing a mixture of 50% pure oxygen balanced with air, yielding a fix inspired O_2 concentration of 60% O_2. During the second test-retest experiment, the participants were given 100% O_2 during periods of HO. Otherwise participants were given medical air to breath. Respiratory gases were continuously monitored using the CO2100C and O2100C modules of a BIOPAC MP150 system (BIOPAC Systems Inc., CA, USA). For additional details, see Lajoie et al. [163].

3.4.2. Image Acquisition

Images were acquired on a clinical 3T MRI scanner (Siemens TIM TRIO, Siemens Medical Solutions, Erlangen, Germany) using the vendor's 32-channel receive-only head coil. The scan session included a 5-minute anatomical acquisition (1 mm^3 MPRAGE with TR/TE/flip angle = 2.3 seconds/3 msec/9°, 256x240 matrix, GRAPPA factor = 2), and an 18-minute functional scan using dual-echo pseudo-continuous ASL sequence (de-pCASL) [108] in order to acquire simultaneous measures of BOLD and CBF. The de-pCASL parameters were: TR/TE1/TE2/alpha = 4.12 seconds/8.4 msec/30 msec/90°, labeling duration = 2 seconds using Hanning window-shaped RF pulse with duration/space = 500 μsec/360 μsec, flip angle = 25°, peak gradient amplitude = 6 mT/m, mean gradient amplitude = 0.6 mT/m, label offset =

100 mm below the center of image slab, nominal and average post-labeling delay (PLD) = 0.9 and 1.44 seconds. The readout consisted of a GRE-EPI with GRAPPA factor = 2, partial sampling of k-space = 7/8, in-plane resolution of 4.5 x 4.5 mm^2, 21 slices with 4.5 mm thickness and 0.45 mm gap.

3.4.3. Respiratory Data Analysis

Analysis of the respiratory data was carried out using an in-house program developed in Matlab (MathWorks, Natick, MA, USA), as in Lajoie et al. [163]. An automatic extraction of the end-tidal (ET) and end-inspiratory points from the continuous O_2 and CO_2 traces was performed. Each ET point was corrected to account for the low-pass filtering effect of the filter placed in series and to account for an expired partial pressure of water of 47 mmHg [109]. More details about the respiratory data analysis can be found in Lajoie et al. [163].

The average values of ETO_2 at baseline and during both respiratory stimuli were used to compute arterial O_2 content (ml O_2/ml blood) and change in the venous deoxygenated fraction ($[dHb]/[dHb]_0$) as in Chiarelli et al. [56] and Gauthier et al. [85]. The latter quantities are needed to obtain the BOLD calibrated value M, resting OEF and $CMRO_2$ as specified below.

3.4.4. Imaging Data Analysis

3.4.4.1. Preprocessing

Analysis of functional scans along with exclusion of artifact and non-paranchymal voxels were performed using in-house software implemented in C, as in Lajoie et al. [163].

During hyperoxic manipulation, the longitudinal relaxation time (T_1) of blood is altered due to an increase in plasma concentration of paramagnetic O_2 [89]. To account for this change in blood T_1, that bias the measured CBF changes, a corrective factor using the approach described in Chalela et al. [91] and Zaharchuk et al. [92] was applied. First, estimates of the arterial blood T_1 values during hyperoxic periods were obtained based on the individual ETO_2 measurements, used as a surrogate for arterial partial pressure of O_2 (PaO_2), along with the R1 ($1/T_1$) and PaO_2 relationship in rats' blood reported in Pilkinton et al. [89].

Depending on whether our ETO_2 values were within or outside the range of values in Pilkinton et al's study, the T_1 values were either linearly interpolated or extrapolated. Then, the individual blood flow maps during HO were corrected by applying a slice-wise corrective factor based on the quantitative blood flow equation [93], the slice acquisition time and the adjusted T_1 value.

3.4.4.2. Computation of $CMRO_2$

MRI measures of BOLD and CBF acquired during the hypercapnic manipulation, along with the changes in the venous deoxygenated fraction were used as inputs to the generalized calibration model (GCM), described in Gauthier and Hoge [59], yielding a functional curve (the "HC curve") of possible pairings of M and OEF. Repeating the procedure with the hyperoxia measurements yielded a second curve of possible M and OEF pairings (the "HO curve"). The intersection of these two curves provided the true values of M and OEF at each voxel. Finally, $CMRO_2$ was determined by multiplying OEF by O_2 delivery, computed as the product of resting CBF by arterial O_2 content. Since the small regional CBF responses to hyperoxia are difficult to measure due to the low SNR of ASL, a uniform change of CBF was assumed throughout the brain, based on the cortical grey matter change after T_1 correction. Additional information about the computation of $CMRO_2$ can be found in Lajoie et al. [163].

3.4.4.3. Tissue segmentation

Automated segmentation of GM from the anatomical scans was carried out using the FMRIB Software Library (FSL) [113]. Structural images were extracted from T_1-weighted scans using the brain extraction tool (FSL's BET). Finally, a probability mask of GM was created employing the automated segmentation tool (FSL's FAST), and was resampled to the resolution of the functional EPI scans.

3.4.4.4. Regions Of Interest (ROIs)

The model-derived estimates were evaluated throughout cortical GM as well as within six ROIs selected from the ICBM OASIS-TRT-20 atlas [114] and presented in Lajoie et al. [163], Figure 1: the inferior parietal, superior parietal, precuneus, hippocampus, anterior

(caudal and rostral) cingulate and posterior cingulate. Each ICBM three-dimensional ROI was registered to the resolution of the functional EPI scans before being conjoined with the individual's GM probability mask excluding voxels with a GM probability lower than 50% as well as non-parenchymal voxels previously identified. Additionally, voxels where the QUO2 model could not be solved were excluded when performing the ROI analysis of *M*, OEF and $CMRO_2$. The resultant ROI probability masks were used to perform weighted averaging of the different measurements and estimates.

3.4.4.5. Registration

Individual $\Delta R2^*_{HO}$, *M*, OEF and $CMRO_2$ maps were non-linearly registered to the ICBM152 template using the CIVET software package [120] via the CBRAIN tool [121] with 12 degrees of freedom using trilinear interpolation as in Lajoie et al. [163]. Test-averaged maps of $\Delta R2^*_{HO}$ were computed as arithmetic means using in-house software. Averaged maps of *M*, OEF and $CMRO_2$ were obtained excluding any voxels where the QUO2 model could not be solved.

3.4.5. Analysis of sensitivity of model-derived QUO2 values to change in O_2 concentration

The end-tidal O_2, blood flow and R2* measurements during a hyperoxia manipulation depend on the employed O_2 concentration. It was discussed that hyperoxia may also perturb the metabolism [83], however, in our model, we consider HO as an isometabolism challenge as assumed in numerous previous calibrated BOLD studies [64,85,106]. In order to understand the impact of lower and higher levels of HO (respectively LHO and HHO) to QUO2, we performed an analysis of the sensitivity of its model-derived parameters, *M*, OEF and $CMRO_2$, to changes in ETO_2, CBF and $\Delta R2^*$. Employing the GM group-average values in Test A during the LHO protocol, we kept constant the parameters not influenced by the O_2 concentration, while individually varying $ETO2_{HO}$, CBF_{HO} and $\Delta R2^*_{HO}$ within their respective range delimited by GM group-average values in Test A under each HO protocol, to compute the resultant *M*, OEF and $CMRO_2$.

3.4.6. Statistical analysis

For each model-derived estimate (M, OEF and $CMRO_2$), we carried out a statistical analysis, using Matlab, on three different combinations of tests: 1) comparing Test A and Test B under the LHO protocol; 2) comparing Test A and Test B under the HHO protocol; 3) comparing tests A between both protocols. When needed, a two-tailed paired t-test was performed, considering a $P < 0.05$ level of significance, to detect any significant difference between tests and protocols. Within each protocol, we also investigated any difference across ROIs by pooling tests values and using family-wise error (FWE) correction for multiple comparisons, set at $P < 0.05$.

Prior to the analysis, statistical tests were performed on the data to ensure it satisfied the repeatability criteria: each distribution of difference between tests was evaluated for normality using the Shapiro-Wilk W-test, while the independence between the magnitude of difference and mean of measurements was verified using a rank correlation coefficient (Kendall's τ). If the difference distribution appeared to deviate from a normal distribution, or if the magnitude of difference increased with the mean of measurements, the data were transformed on the $\log_{10}$ scale and the verification was repeated. In cases where the $\log_{10}$ scaled data satisfied the criteria, the repeatability was assessed on these scaled values. Otherwise, assessment of repeatability was based on the original values, as done in previous studies [122-124].

The next metrics were evaluated:

a) dSD, the standard deviation of the difference between tests measurements.

b) wsSD, the within-subject standard deviation, equals dSD/√2 considering two measurements.

c) wsCV, the within-subject (or intra-subject) coefficient of variation, as used in Floyd et al. [123] and Chen et al. [125]. wsCV=√[mean of the (wsSD/subject mean)^2]. wsCV provides an unbiased measure of variability expressed as a percent of the mean with a low wsCV indicating a high reproducibility/repeatability. When data were on the $\log_{10}$ scale, wsCV was approximated by 10^(wsSD)-1 [126].

d) bsCV, the between-subject (or inter-subject) coefficient of variation as computed in Tjandra et al. [128]. bsCV = $SD_{pooledData}$ / $mean_{pooledData}$ * 100.

3.5. Results

One participant reported a high level of anxiety during Test A of the LHO protocol, and the measured CBF response to CO_2 was found to be twice the standard deviation of the group mean. Data from this participant has been excluded from the present analysis (as in the previous related work [163]).

3.5.1. Gas manipulation

The test-average and standard deviation of end-tidal O_2 and CO_2 at baseline and during periods of hyperoxia are presented in Figure 3.1. No difference was found within and between protocols resting ETO_2 (within-protocol: $TestA_{LHO}$ = 112±7 mmHg vs. $TestB_{LHO}$ = 112±3 mmHg, P = 0.88, $TestA_{HHO}$ = 113±7 mmHg vs. $TestB_{HHO}$ = 108±7 mmHg, P = 0.05 ; between-protocol: LHO = 112±5 mmHg vs. HHO = 111±7 mmHg, P = 0.7). Within-protocol $ETO2_{HO}$ were identical ($TestA_{LHO}$ = 366±6 mmHg vs. $TestB_{LHO}$ = 371±14 mmHg, P = 0.37 ; $TestA_{HHO}$ = 656±17 mmHg vs. $TestB_{HHO}$ = 652±25 mmHg, P = 0.42), whereas, as expected, between-protocol $ETO2_{HO}$ were found to be significantly different (LHO = 369±10 mmHg vs. HHO = 654±20 mmHg, $P < 6*10^{-12}$). No difference was detected in between-protocol resting $ETCO_2$ (LHO = 40±2 mmHg vs. HHO = 42±2 mmHg, P = 0.3), nor within the LHO protocol ($TestA_{LHO}$ = 41±2 mmHg vs. $TestB_{LHO}$ = 40±2 mmHg, P = 0.57). However a significant difference in resting $ETCO_2$ was observed between Test A and Test B under the HHO protocol ($TestA_{HHO}$ = 43±2 mmHg vs. $TestB_{HHO}$ = 40±2 mmHg, $P < 0.002$). This difference in resting $ETCO_2$ is in agreement with a lower respiratory rate during Test A compared to Test B ($TestA_{HHO}$ = 6±2 breaths per minute vs. $TestB_{HHO}$ = 8±1 breaths per minute, P = 0.03). The $ETCO_2$ changes observed during periods of hyperoxia were found to be equivalent within protocol. For the LHO protocol, they were: $TestA_{LHO}$ = -0.8±1.0 mmHg and $TestB_{LHO}$ = -1.1±1.1 mmHg (P = 0.8), while for the HHO protocol they were: $TestA_{HHO}$ = -2.5±0.7 mmHg and $TestB_{HHO}$ = -2.4±0.7 mmHg (P = 0.5). The averaged decreases in $ETCO_2$ were

significantly ($P < 0.005$) larger in HHO compared to LHO protocol (LHO = -1.0±1.0 mmHg vs. HHO = -2.4±0.7 mmHg).

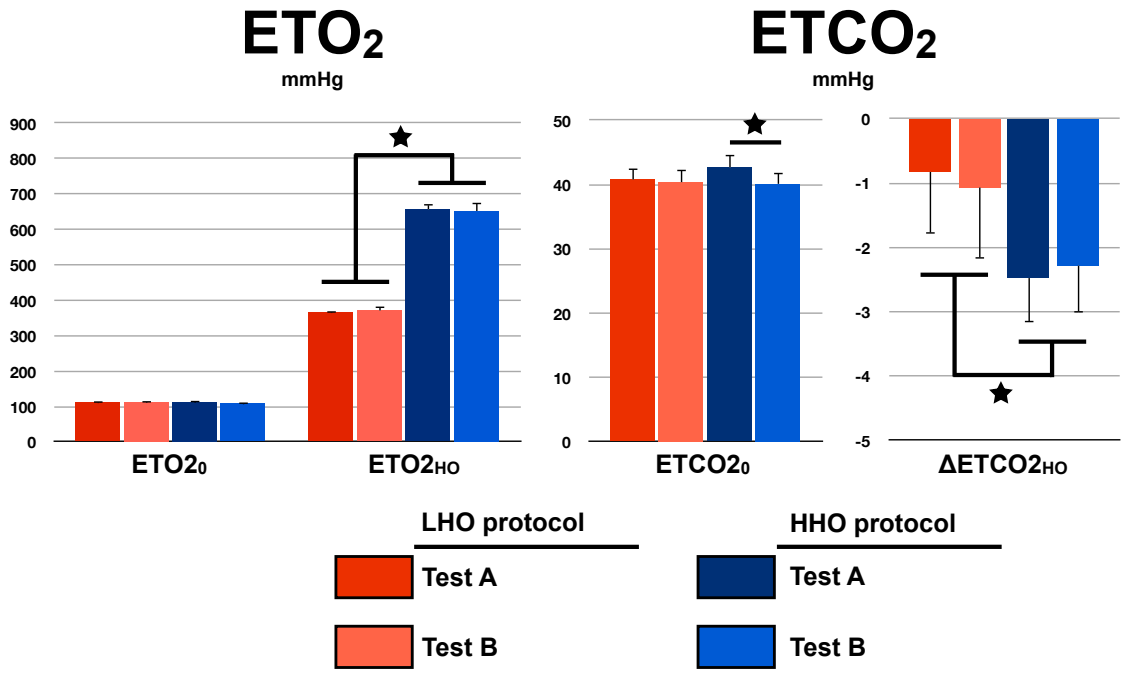

Figure 3.1. Gas manipulations
For each protocol and test, the measured resting (with the subscript '0') and hyperoxic (with the subscript 'HO') end-tidal O_2 and CO_2 are presented. Errors bars indicate standard deviation. A star indicates a significant difference at $P < 0.05$.

3.5.2. Susceptibility artifacts

Figure 3.2 shows a qualitative examination of R2* changes during periods of HO (ΔR_2*) through axial, sagittal and coronal views chosen in order to observe regions vulnerable to susceptibility artifacts. No masking or median filtering were performed on the functional maps prior to the non-linear registration to the ICBM template and maps average. The contrast window was chosen to facilitate the observation of increase in R2* characterized by orange and red colors. An overall R2* decrease (equivalent to a BOLD increase) in white and grey matter during HO is observed, which is more significant under the more extreme levels of HO. On the other hand, as a repercussion of the presence of paramagnetic oxygen molecules in

inhaled air, both protocols presented comparable regions of susceptibility artifacts characterized by positive ΔR2* in voxels surrounding the nasal cavity. Percent of voxels in GM characterized by this increase were found to be the same in both protocols, with 12.8% under the LHO protocol and 11.7% under the HHO protocol (P = 0.25), although the positive values were generally higher under the HHO protocol (shown by darker red color). Any voxel affected by the susceptibility artifacts, later results in a non-solution voxel for M, OEF and $CMRO_2$, and were therefore excluded from the analysis as mentioned in the methodology section.

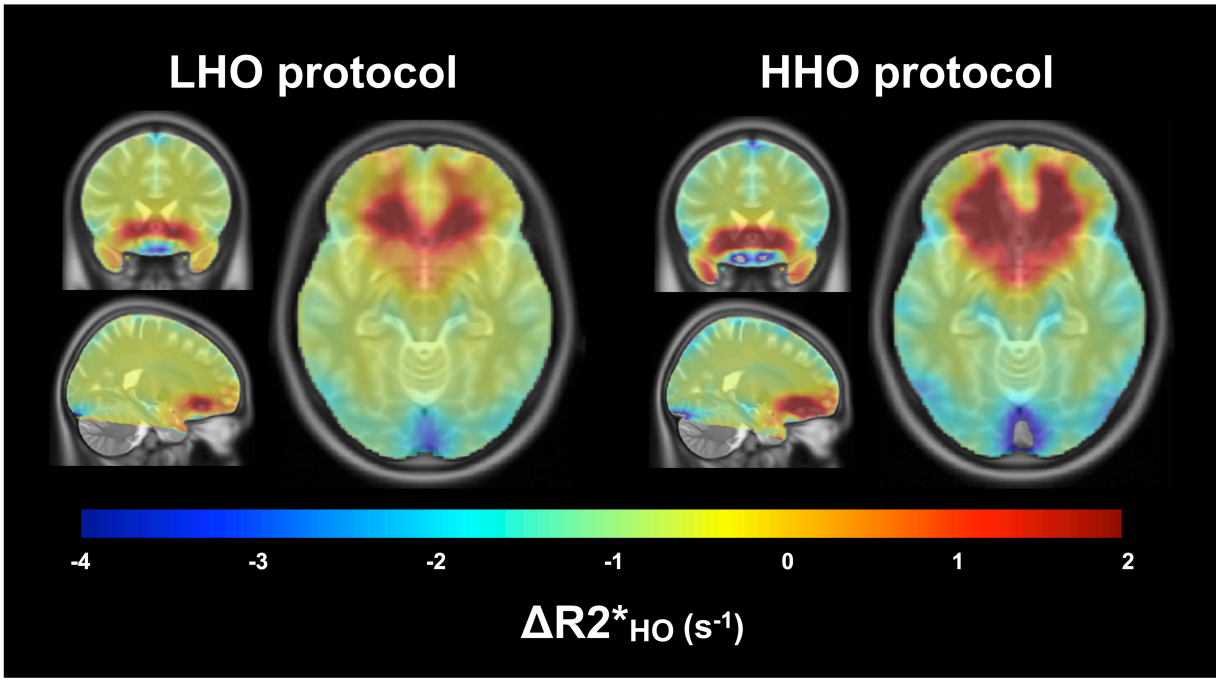

Figure 3.2. Susceptibility artifacts
For each protocol, the averaged maps of ΔR2* during HO are shown in coronal, sagittal and axial views, overlaying the ICBM152 template. The chosen contrast window facilitates the localization of voxels where an increase in R2* is observed (in orange and red). These increases in the transverse relaxation rate are most likely the results of susceptibility artifacts attributable to the presence of paramagnetic O_2 in frontal sinuses and nasal cavity.

3.5.3. T_1 shortening

A value of 1.65 sec was assumed for the normoxic arterial blood T_1 [166], whereas the estimated blood T_1 shortening was larger during the high O_2 hyperoxia state than during the low hyperoxia challenge: T_{1HHO} = 1.47±0.01 sec vs. T_{1LHO} = 1.56±0.01 sec, $P < 4*10^{-13}$. Figure 3.3 summarizes, in both protocols, the GM tests average and standard deviation of blood flow decrease during HO before and after correction of blood T_1. While uncorrected, CBF_{HO} decrease was found to be significantly larger under the HHO protocol (LHO = -8.1±4.2 mmHg, HHO = -17.5±6.6 mmHg, $P < 0.002$). After T_1 correction, CBF_{HO} decreases were less pronounced in both protocols, and were not found significantly different from each other (LHO = -1.9±4.3 mmHg, HHO = -2.8±7.5 mmHg, $P = 0.7$) nor from zero ($P_{LHO} = 0.4$, $P_{HHO} = 0.3$).

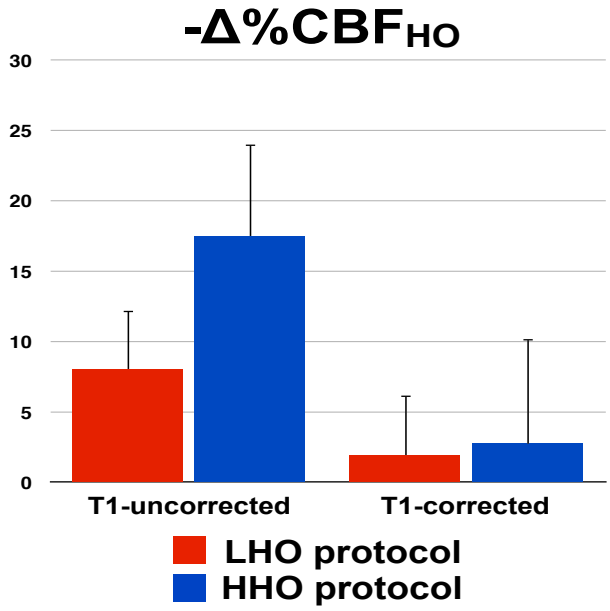

Figure 3.3. T_1 shortening
For each protocol, pre- and post-T_1-correction CBF changes during HO, averaged across tests, are presented with the standard deviation as error bars.

3.5.4. Analysis of sensitivity of model-derived QUO2 values to change in O_2 concentration

The individual impacts of changes in $ETO2_{HO}$, $\Delta R2^*_{HO}$ and $\Delta\%CBF_{HO}$, on *M* and OEF, as a function of the HO levels are examined by numerical simulations. These changes in $ETO2_{HO}$, $\Delta R2^*_{HO}$ and $\Delta\%CBF_{HO}$ are dependent on one another and are examined in order to explain the combined impact on *M* and OEF. Results are summarized in Figure 3.4. Figure 3.4-A shows the displacement in the HO curves caused by the respective variation of $ETO2_{HO}$, $\Delta R2^*_{HO}$ and $\Delta\%CBF_{HO}$, while Figure 3.4-B shows the corresponding OEF and *M* solutions as a function of the individual (colored solid lines) and combined (dashed black lines) changes. Since the O_2 concentration solely modulates the HO curve, which is shifted on the nearly horizontal section of the HC curve, the changes in $ETO2_{HO}$, $\Delta R2^*_{HO}$ and $\Delta\%CBF_{HO}$, either individual or combined, have virtually no impact on the *M* estimates. With respect to OEF, the individual impacts appear to cancel each other out, yielding a modest combined effect. The same conclusion stands for $CMRO_2$, since it is the result of multiplying OEF by two measurements that are independent of the hyperoxic stimulus, i.e. the resting CBF and the resting arterial O_2 content. Therefore, in principle, one would expect *M*, OEF and $CMRO_2$ to remain stable, regardless of the O_2 concentration used to produce hyperoxia. The following sections explore this assumption using real values computed in different ROIs, but also on a voxel-wise basis.

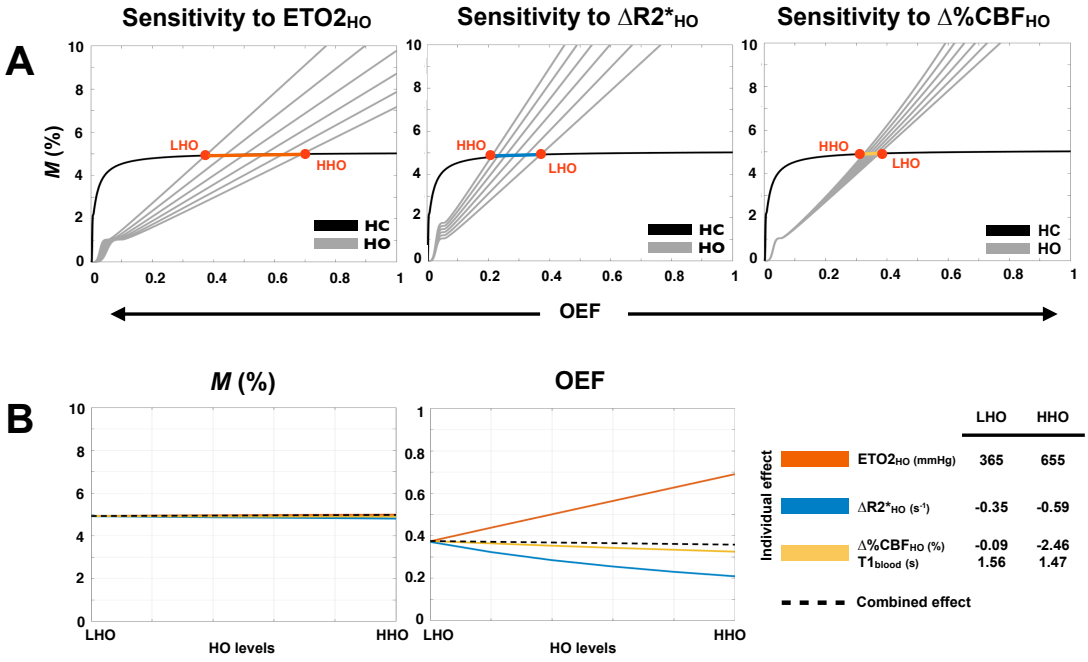

Figure 3.4. Analysis of sensitivity to O_2 concentration

Observed effects, on *M* and OEF, of changes in ETO_2, R2* and CBF following a transition from a low level of hyperoxia (LHO) to a higher level of hyperoxia (HHO) are summarized. Estimates were based on group-averaged Test A measurements during the LHO manipulation, while ETO_2, R2* and CBF were varied independently ranging from their respective LHO value to their HHO value (values are specified in the legend, with the corresponding blood T_1 below CBF_{HO}). The hypercapnia (HC) and hyperoxia (HO) curves resulting from the use of six different values of ETO_2, R2* and CBF are presented (A). Each red dot represents the HC and HO curves intersection (hence one *M* and OEF solution) when either one of the extremity of the observed range is in use. The remaining *M* and OEF solutions lie on the colored line connecting both red dots. *M* and OEF estimates are presented as a function of the individual (colored solid lines) and combined (dashed black lines) effect of changes in ETO_2, R2* and CBF (B).

3.5.5. Protocol-averaged estimates in ROIs

In Figure 3.5-A are shown the ROI-averaged *M*, OEF and $CMRO_2$ in each protocol (red and blue bars) and over both protocols (green bars). For each combination of model-derived estimate and ROI, we observe a good consistency between protocols with the lowest *P* values being: $P = 0.17$ in superior parietal for *M*, $P = 0.37$ in superior parietal for OEF and $P =$

0.06 in GM for $CMRO_2$. Additionally, no apparent divergence was found in variance within each protocol. In Figure 3.5-B are shown, for each estimate, the degrees of difference between ROIs, when comparing the estimate averaged over both protocols and correcting for multiple comparisons (FWE set at $P < 0.05$). OEF estimates were found to be similar across ROIs, with the exception between hippocampus and anterior cingulate where a significant difference was detected ($P = 0.04$). Values of M and $CMRO_2$ in hippocampus were found to be the smallest compared with the other ROIs, with the exception of anterior cingulate (for M) and superior parietal (for $CMRO_2$).

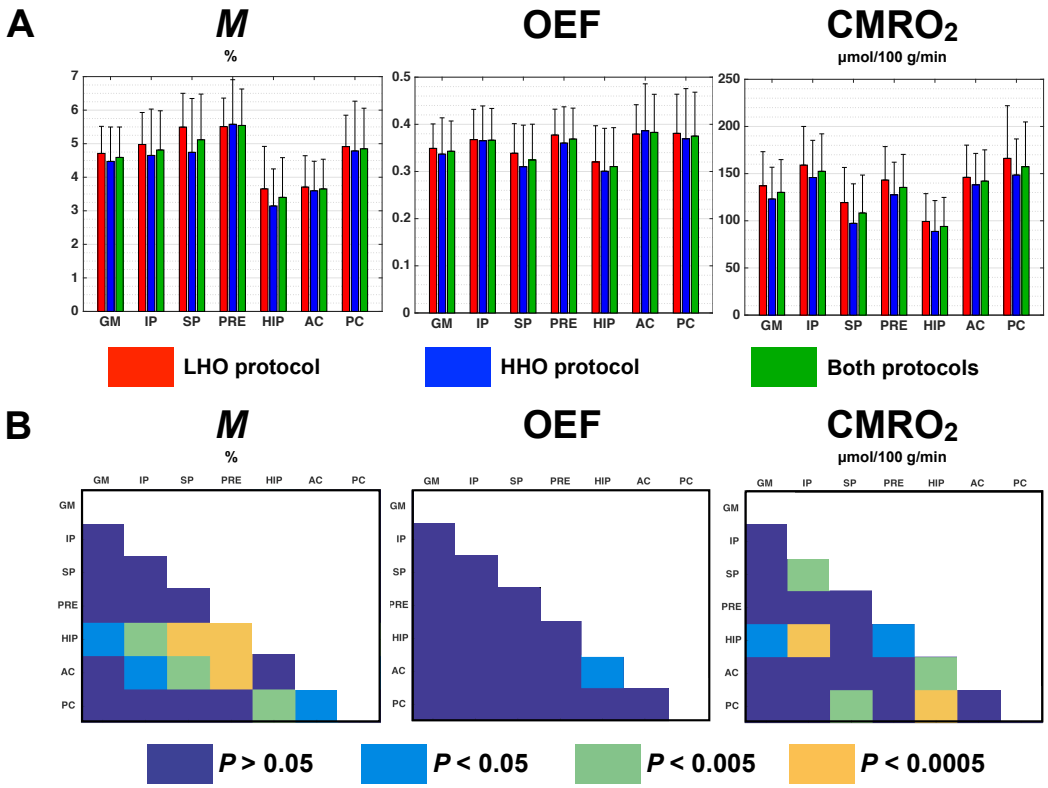

Figure 3.5. Protocol-averaged estimates in ROIs

M, OEF and $CMRO_2$ estimates averaged in different ROIs are compared. Figure A presents the ROI-averaged value and standard deviation obtained under the LHO protocol (red bar), the HHO protocol (blue bar) and in both protocols averaged (green bar). Figure B shows, for each estimate, any significant difference observed between ROIs after correcting for multiple comparisons (FWE, $P < 0.05$): dark blue indicates an absence of significant difference ($P > 0.05$), while light blue ($P < 0.05$), green ($P < 0.005$) and orange ($P < 0.0005$) illustrate a significant difference between two ROIs (represented in the X and Y axis). *LHO* = low hyperoxia, *HHO* = high hyperoxia, *GM* = grey matter, *IP* = inferior parietal, *SP* = superior

parietal, *PRE* = precuneus, *HIP* = hippocampus, *AC* = anterior cingulate, *PC* = posterior cingulate.

3.5.6. Within-subject variability in ROIs

Figure 3.6 presents the within-subject coefficients of variation (wsCV) in every ROIs for *M*, OEF and $CMRO_2$. WsCVs were computed for three combinations of tests: 1) test A vs. B under the LHO protocol, 2) test A vs. B under the HHO protocol, 3) tests A between both HO protocols. Across all ROIs, *M* was found to have a lower within-subject variability under the LHO protocol (mean $wsCV_{LHO}$ = 16%, mean $wsCV_{HHO}$ = 25%, *P* = 0.006). On the other hand, within-subject variability of OEF and $CMRO_2$ were found unchanged regardless of the HO protocol (OEF: mean $wsCV_{LHO}$ = 15%, mean $wsCV_{HHO}$ = 16%, *P* = 0.2; $CMRO_2$: mean $wsCV_{LHO}$ = 17%, mean $wsCV_{HHO}$ = 18%, *P* = 0.6).

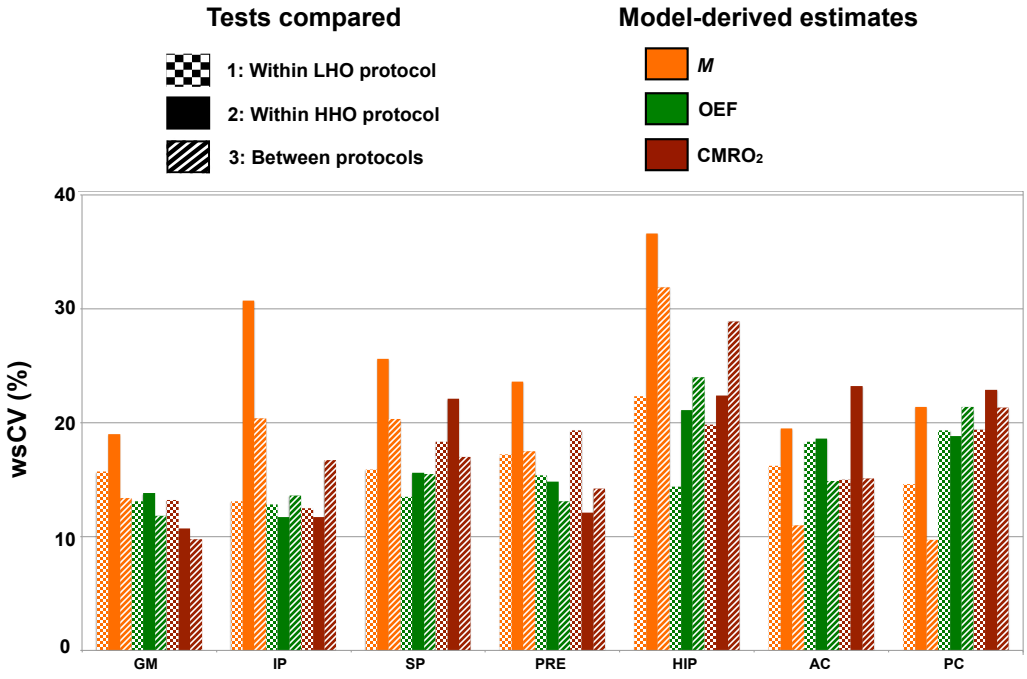

Figure 3.6. Within-subject variability in ROIs
Computed within-subject CVs (wsCV) are shown for *M*, OEF and $CMRO_2$ within each ROI. The model-derived estimates are represented by different colors, while the three combinations of tests are identified by distinct patterns: 1: Test A vs. B under the LHO protocol (squared pattern), 2: Test A vs. B under the HHO protocol (plain pattern), 3: Tests A between both HO protocols (striped pattern). *LHO* = low hyperoxia, *HHO* = high hyperoxia, *GM* = grey matter,

IP = inferior parietal, *SP* = superior parietal, *PRE* = precuneus, *HIP* = hippocampus, *AC* = anterior cingulate, *PC* = posterior cingulate.

3.5.7. Parametric maps

In Figure 3.7, we present, for each combination of tests (1: Test A vs. B under the LHO protocol, 2: Test A vs. B under the HHO protocol, 3: Tests A between both HO protocols), mean tests, between- and within-subject CV maps of *M*, OEF and $CMRO_2$. All functional maps were non-linearly registered (NLreg) to the ICBM space. In addition to intrinsic physiological changes, errors in measurements and head movements occurring between the anatomical and the functional scans, a voxel-wise within-subject repeatability may be partly affected by random inaccuracies in registration. In order to evaluate any limitation on the voxel-wise repeatability caused by the registration to the ICBM space, we present the CVs maps for MPRAGE, and verify if any enhancement was possible thanks to the non-linearly registration of our maps (Figure 3.7-A), compared to the linearly registered MPRAGE (Figure 3.7-B). All CVs maps are shown using a window level of 0-200%. At these levels, the passage from 20% to 30% is characterized by the transition from purple to blue, with 30% being an approximate upper limit for what is considered as low variability. Compared to the linearly registered maps (Lreg), the non-linearly registered (NLreg) MPRAGE maps presented a better defined grey matter region, while whole-brain between- and within-subject variability were found to be lower. WsCV values in NLreg were generally found to be <5% in WM, <10% in GM and exceptionally <20% in few small regions, whereas in Lreg wsCV, values were <10% in WM and GM and <20% in with few small regions. Mean maps of *M*, OEF and $CMRO_2$ (Figure 3.7- C, D, E) qualitatively exhibited an absence of dependency on the O_2 protocol employed. CVs maps of *M* presented slightly less variability under the LHO than the HHO. All three estimates were found to have low GM within-subject variability for the three combinations of tests (<30%). *M* and $CMRO_2$ presented a clearer distinction between the population variance and the within-subject variability, whereas OEF was found to have a lower voxel-wise between-subject variability, approaching the within-subject variability.

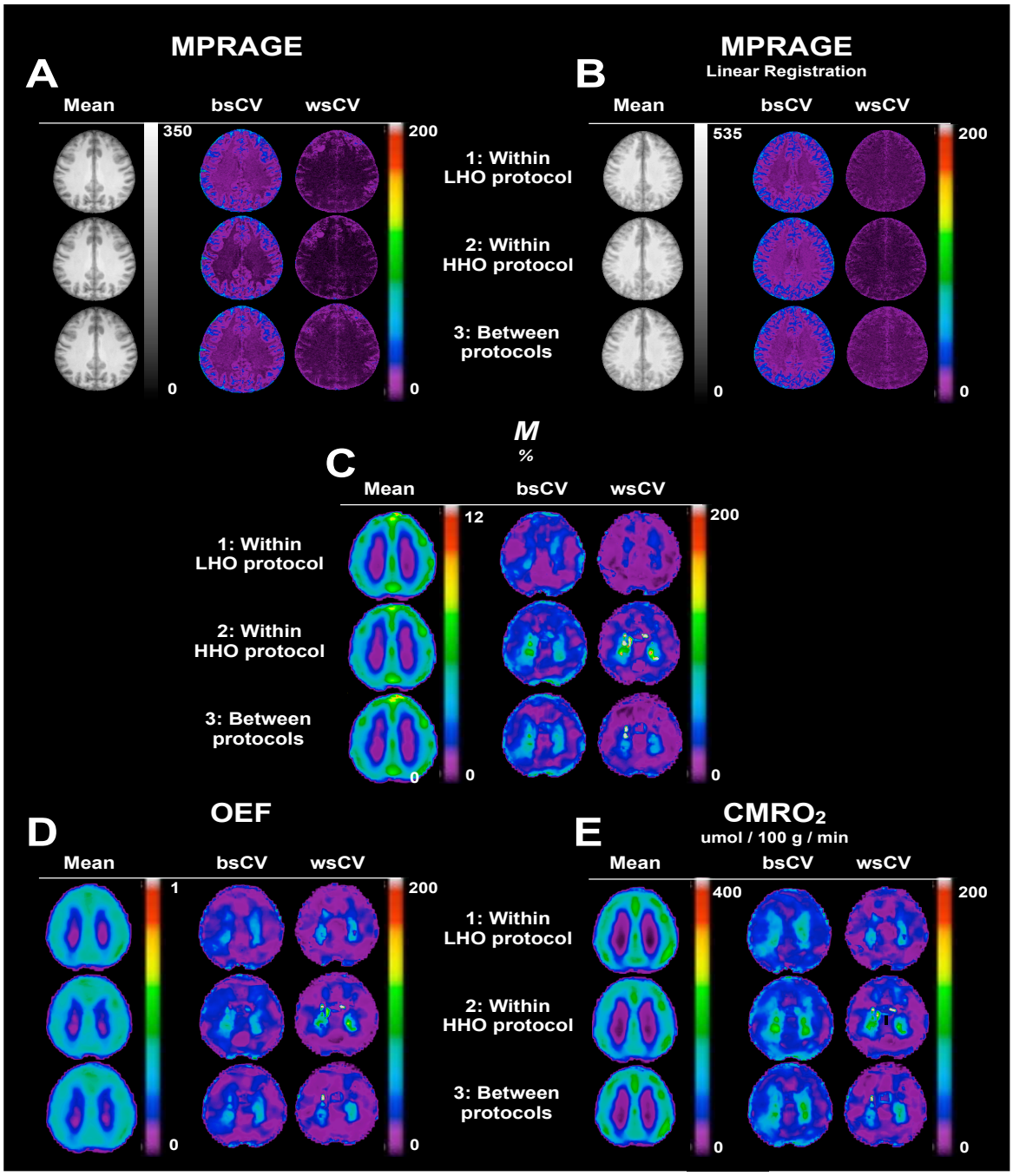

Figure 3.7. Parametric maps

For each combination of tests (1: Test A vs. B under the LHO protocol, 2: Test A vs. B under the HHO protocol, 3: Tests A between both HO protocols), mean tests, between-subject CV and within-subject CV maps for *M* (C), OEF (D) and $CMRO_2$ (E) are shown in one axial slice. Maps were non-linearly registered to the ICBM152 template. As a reference, the equivalent information is presented for MPRAGE maps non-linearly (A) and linearly registered (B) to the template. *LHO* = low hyperoxia, *HHO* = high hyperoxia.

3.6. Discussion

Performing an analysis of individual impacts, on *M* and OEF, of variation in $ETO2_{HO}$, $\Delta R2^*_{HO}$ and $\Delta\%CBF_{HO}$, we have shown how little *M* is affected by the O_2 concentration in GM, and how the individual impacts on OEF were practically cancelling out, yielding a nearly nonexistent combined impact on OEF and therefore on $CMRO_2$. Exploring the within-subject reproducibility in different ROIs as well as on a voxel-wise basis, we observed an unchanged reproducibility for OEF and $CMRO_2$ regardless of differences in $ETO2_{HO}$, $\Delta R2^*_{HO}$ and $\Delta\%CBF_{HO}$ caused by a distinct O_2 concentration in inhaled gas. On the other hand, the *M* within-subject repeatability was found to be slightly enhanced under the LHO protocol. No significant difference was found between protocol-averaged values.

In certain situations, the differences between subjects' brain anatomy are such that a linear transformation is insufficient to register their brain maps on to standard spaces. The local deformations produced by the non-linear registration improve the match. The comparison of linearly versus non-linearly registered individual MPRAGE images provides a qualitative example of the improvement brought by the non-linear registration. The method produced sharper group-averaged maps, characterized by more distinct sulci and more accentuated grey/white matter contrast. Quantitatively, the non-linear co-registration afforded lower CV values.

The presence of paramagnetic molecular oxygen in inhaled air produces susceptibility artifacts. We examined regions vulnerable to those artifacts such as the frontal sinuses and nasal cavity of our $\Delta R2^*_{HO}$ maps. However, no evidence of enlarged patterns of susceptibility artifacts under inhalation of 100% O_2 (HHO) compared to 60% (LHO) was found, thus yielding a comparable percent of non-solution voxels in GM for both protocols.

Rather than assuming a fixed value of CBF change during HO, the individual T_1-corrected $\Delta\%CBF_{HO}$ averaged in GM was used, therefore capturing any intra-subject variation between Test A and Test B in blood flow during HO. Our T_1 values were extrapolated from experimentally-determined values in animal model, which is a common practice in calibrated

fMRI approaches. Human blood constitution is similar to that of bovine and rat blood and is likely to experience comparable T_1 shortening during the hyperoxia stimulus [89,167,168]. This is of course an assumption and represents a potential source of confounds in our blood flow changes calculations.

In CBF quantification, so long as the PLD is equal to or higher than the arterial transit time (ATT), the exact ATT value does not matter. In our 2D acquisition, the first and last slices are acquired after a delay of 900 msec and 1986 msec respectively, resulting in a brain-averaged PLD of 1443 msec. Donahue et al. [151] applied a pCASL in a cohort of healthy volunteers (mean age of 30 ± 4 years) and obtained a group-averaged ATT lower than 900 msec within each lobe, including within the occipital lobe with 834 ± 29 msec. We therefore believe that in the large majority of cases, the acquired ASL signal was accurately reflecting CBF and that an increase in our PLD would have resulted in a loss in SNR, especially during hypercapnic where the ATT is known to diminish [151]. Additionally, the ATT increase during HO should be minor as our data indicates that the CBF decreases induced by hyperoxia, even at high O_2 concentrations, are not substantial. When using a 2D acquisition in a population of elderly or unhealthy patients, it would be recommended to increase the PLD slightly while also imaging a lower number of thicker slices, as in the study De Vis et al. (2015) where a nominal PLD of 1550 msec and 11 slices with 7 mm slice thickness were employed.

Small cohort sizes like that of the present study have been common in recent years, particularly for complex fMRI protocols with greater physiological specificity than the classic BOLD contrast. Despite the relatively small sample size, which limits confidence in the statistical significance of our findings, the present study provides new information on the impact of inspired oxygen levels on calibrated fMRI technique.

To conclude, it was revealed that the pattern of susceptibility artifacts under hyperoxia was comparable regardless of the HO levels. We also demonstrated that variations in $ETO2_{HO,}$ CBF_{HO} and $R2^*_{HO}$ were accounted for within the QUO2 model, resulting in an unchanged ROI-averaged M, OEF and $CMRO_2$ estimates. We observed that the within-subject repeatability was either unchanged (for OEF and $CMRO_2$) or slightly enhanced under the LHO protocol (for M). In summary, the use of a higher hyperoxic challenge revealed no

beneficial impact on the calibrated fMRI measurements, while a reduced concentration of 60% O_2 was shown to maintain sufficient BOLD contrast and to produce consistent model-derived results.

3.7. Acknowledgments

The authors would like to thank Scott Nugent, Marius Tuznik, Bahare Sabouri, Carollyn Hurst and André Cyr for their excellent technical assistance and insightful discussions. Jiongjiong Wang at UCLA is acknowledged for providing the pseudo-continuous arterial spin-labeling sequence. This study was supported by the Canadian Institutes of Health Research (MOP 123492), Canada Foundation for Innovation (17380), Natural Sciences and Engineering Research Council of Canada (R0018142), Fonds Québécois de la Recherche sur la Nature et les Technologies (FQRNT), and the Consortium québécois sur la découverte du médicament (CQDM). The funders had no role in study design, data collection and analysis, decision to publish, or preparation of the manuscript.

4. Application of calibrated fMRI in Alzheimer's disease

Authors: Isabelle Lajoie, Scott Nugent, Clément Debacker, Kenneth Dyson, Felipe B. Tancredi, AmanPreet Badhwar, Sylvie Belleville, Yan Deschaintre, Pierre Bellec, Julien Doyon, Christian Bocti, Serge Gauthier, Douglas Arnold, Marie-Jeanne Kergoat, Howard Chertkow, Oury Monchi, Richard D. Hoge

Authors contributions: Study design, Recruitment of participants and Interpretation of results: All authors; Software development: IL FBT RDH; Data acquisition: IL SN CD KD; Formal analysis: IL; Writing original draft and Visualization/Data presentation: IL.

Status: Published in the journal *NeuroImage: Clinical 15 (2017) 348–358*

.

4.1. Preface

In addition to being characterized by cholinergic deficits [1], deposition of beta-amyloid (Aβ) [2,3] and tau abnormality [4], Alzheimer's disease (AD) is believed to be related to vascular [169] and mitochondrial burdens [6]. Previous positron emission tomography (PET) studies have detected decreases in blood flow and in oxygen metabolism in AD, essentially in the temporal and parietal lobes [14,16,17]. The pattern of hypoperfusion and hypometabolism was found to differ according to the degree of AD progression [24] and between similar conditions such as in frontotemporal and vascular disease dementia where a frontal component has being observed [15,25]. Imaging of baseline $CMRO_2$ using PET is arduous, as it requires three separate injections of short-lived radioactive tracers, making the adoption of the approach in large-scale and clinical studies difficult. The development of MRI-based methods that allow the brain mapping of resting blood flow and of resting $CMRO_2$ became a promising avenue for studies where the vascular and/or the metabolic may be affected, such as in aging and AD. In addition to being accessible and non-invasive, the MRI-based methods provide, within a single modality, concurrent acquisitions of different types of data for correlation purpose such as structural, resting-state connectivity, task-induced responses and cerebrovascular reactivity. Furthermore, any disease-related differences in quantitative MRI estimates may serve to flag bias not considered in standard qualitative BOLD methods. In summary, these MRI approaches may help to dissociate AD from other conditions such as frontotemporal dementia [25] or vascular disease [15] as well as offering new insight on the pathophysiology of AD that go beyond the glucose metabolism and amyloid deposition. The initial proof-of-concept QUO2 was enhanced and further validated as described in previous Chapters. Here, we present the application of the optimized QUO2 method in a cohort of 65 recruited probable AD and 65 age-matched controls. To our knowledge, this is the first time that such techniques are applied in AD.

4.2. Abstract

Calibrated fMRI based on arterial spin-labeling (ASL) and blood oxygen-dependent contrast (BOLD), combined with periods of hypercapnia and hyperoxia, can provide information on cerebrovascular reactivity (CVR), resting blood flow (CBF), oxygen extraction fraction (OEF), and resting oxidative metabolism ($CMRO_2$). Vascular and metabolic integrity are believed to be affected in Alzheimer's disease (AD), thus, the use of calibrated fMRI in AD may help understand the disease and monitor therapeutic responses in future clinical trials. In the present work, we applied a calibrated fMRI approach referred to as Quantitative O2 (QUO2) in a cohort of probable AD dementia and age-matched control participants. The resulting CBF, OEF and $CMRO_2$ values fell within the range from previous studies using positron emission tomography (PET) with ^{15}O labeling. Moreover, the typical parietotemporal pattern of hypoperfusion and hypometabolism in AD was observed, especially in the precuneus, a particularly vulnerable region. We detected no deficit in frontal CBF, nor in whole grey matter CVR, which supports the hypothesis that the effects observed were associated specifically with AD rather than generalized vascular disease. Some key pitfalls affecting both ASL and BOLD methods were encountered, such as prolonged arterial transit times (particularly in the occipital lobe), the presence of susceptibility artifacts obscuring medial temporal regions, and the challenges associated with the hypercapnic manipulation in AD patients and elderly participants. The present results are encouraging and demonstrate the promise of calibrated fMRI measurements as potential biomarkers in AD. Although $CMRO_2$ can be imaged with ^{15}O PET, the QUO2 method uses more widely available imaging infrastructure, avoids exposure to ionizing radiation, and integrates with other MRI-based measures of brain structure and function.

Keywords: Calibrated fMRI, Alzheimer's disease, Cerebral blood flow, Oxidative metabolism, Oxygen extraction fraction, BOLD calibration constant, Cerebrovascular reactivity

4.3. Introduction

Functional MRI (fMRI) methods, such as brain imaging based on arterial spin-labeling (ASL) or blood oxygenation level-dependent (BOLD) contrasts, are sensitive to cerebral blood flow (CBF) and the cerebral metabolic rate of oxygen ($CMRO_2$). Calibrated fMRI exploits this sensitivity, using ASL and BOLD data acquired during controlled manipulations of cerebral physiology to compute quantitative estimates of $CMRO_2$ and related parameters such as the BOLD calibration constant *M* [55,56,59].

In contemporary calibrated fMRI methods, which combine hypercapnic and hyperoxic manipulations, absolute measures of resting $CMRO_2$ in addition to other physical and physiological variables are obtained [64,65]. These methods have the potential to provide distinct physiological information in conditions where cerebral blood flow and metabolism may be affected. Since Alzheimer's disease (AD) is believed to be associated with both vascular and metabolic effects [6,169], it presents a compelling target to study using calibrated fMRI. The objective of the present study was to apply an approach we have previously termed Quantitative O2 (QUO2) [65] in cohorts of probable AD patients and age-matched controls.

There is evidence for mitochondrial dysfunction and oxygen hypometabolism as being a causal factor in AD, as well as in other conditions such as Parkinson's Disease (Bonda et al., 2010; Coskun et al., 2011; Reddy and Beal, 2005; Silva et al., 2011; Sullivan and Brown, 2005; Wallace, 2005). Hence, the QUO2 method allows us to study the hypothesis in which metabolism and vascular dysfunction appear earlier in the disease than cholinergic deficits, beta-amyloid deposition and hyperphosphorylated tau pathology. Moreover, the method may be employed to deepen our understanding of other conditions where vascular and oxygen metabolism may be compromised (such as in Parkinson's Disease). Finally, the physiological information offered by the calibrated fMRI method may be better correlated with the clinical profile of AD than the other biomarker candidates.

While CBF and $CMRO_2$ can be quantitatively imaged using positron emission tomography (PET), the use of calibrated fMRI offers several unique features. First, the estimates of CBF and $CMRO_2$ from calibrated fMRI are expressed within a biophysical framework that is directly relevant to task activation or resting-state BOLD fMRI studies that

are performed in AD [42-47]. Any disease-related difference in parameter estimates from calibrated fMRI may thus be readily evaluated in terms of its impact on standard BOLD methods, which may in turn help identify (or rule out) bias associated with underlying physiological changes that are not accounted for in qualitative BOLD analysis.

Calibrated fMRI also provides, either through intermediate results or incidentally, physiological information that is not available through other methods. The QUO2 method used in the present study yields estimates of resting $CMRO_2$, oxygen extraction fraction (OEF) and M in addition to the transverse relaxation rate constant R2*, and CO_2 cerebrovascular reactivity (CVR) (expressible in terms of several parameters including CBF, BOLD signal, and R2*). M is a sensitivity measure for BOLD fMRI, helping validating the use of the BOLD method as a comparative marker between two groups. R2* is a measure similar to susceptibility-weighted imaging (SWI), it can reflect levels of iron in the tissue as well as level of deoxygenated blood. OEF allows assessment of the presence of cerebral ischemia. These parameters are likely to be influenced by vascular function and oxygen transport, making them potential biomarkers of interest in AD.

Finally, the equipment needed to perform calibrated fMRI techniques may be more readily available for many institutions than equipment necessary to carry out PET radiotracer studies, particularly with short-lived isotopes such as ^{15}O. This would facilitate the implementation of multi-center research such as large-scale cohort studies or clinical drug trials.

4.4. Methodology

4.4.1. Participants

A cohort of 65 individuals with mild to moderate dementia of Alzheimer's type and 61 age-matched controls were recruited for the present study. Recruited patients met the criteria for "probable AD dementia" as specified in the NIA/AA Guidelines [170] and had a Mini-Mental State (MMSE) score between 18 and 27. All participants gave written informed consent and the project was approved by the Comité mixte d'éthique de la recherche du Regroupement Neuroimagerie/Québec. Exclusion criteria at entry included: cessation of

education before achieving basic literacy in native language, prior history of significant psychiatric or neurological illness (other than AD), significant intellectual handicap, undergoing current or recent (≤2 months) treatment for a significant medical condition, chronic obstructive pulmonary disease, history of recurrent asthma, or other significant respiratory disorder, comorbidity with other underlying pathologies for dementia (for AD cohort) and clinical history of cognitive or memory impairment (for control cohort). All participants were either English or French speakers and had a normal or corrected-to-normal hearing and vision (relevant for behavioral testing, although corrective measures were not required during the MRI protocol).

From the recruited group, 31 AD and 24 control participants were not included in the present data analysis due to data inclusion criteria outlined in Figure 4.1, yielding a final dataset of 34 AD (15 males, mean age of 76.9 ± 6.5) and 37 controls (14 males, mean age of 74.4 ± 4.6). All participants underwent a blood draw, which allowed measurement of their hemoglobin concentration [Hb] that was used to compute $CMRO_2$. Participants also completed the Montreal Cognitive Assessment (MoCa) to ensure the absence of cognitive impairment in the control cohort. Control participants who scored less than 26 in the MoCa were excluded from the present analysis (n = 10).

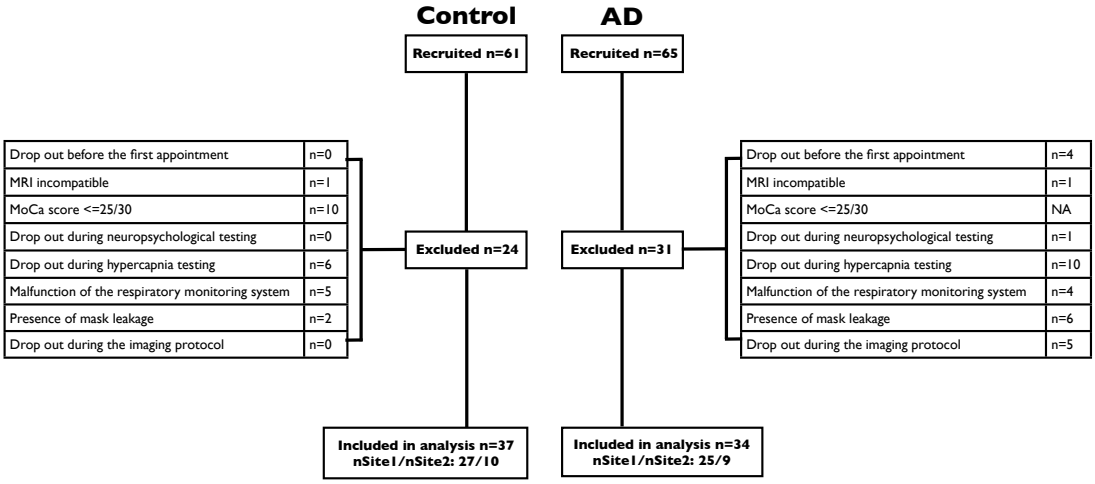

Figure 4.1. Participant retention
Exclusion criteria for the Alzheimer's patients (AD) and healthy controls cohorts. *MoCa* = Montreal Cognitive Assessment.

4.4.2. Data Acquisition

4.4.2.1. Respiratory Paradigm

A gas timing schedule previously described by Bulte et al. [64], with a total duration of 18 minutes, was applied. This involved two 2-minute periods of hypercapnia (HC) and two 3-minute periods of hyperoxia (HO), induced by administering gas mixtures enriched with CO_2 (5%) and O_2 (50%) respectively. Hypercapnia was followed by a 1-minute normocapnic period while hyperoxia was followed by a 3-minute period of normoxia. Participants inhaled the gas mixtures via a breathing circuit developed in-house and described by Tancredi, Lajoie & Hoge (2014) [66]. Respiratory gases were continuously monitored using the CO2100C and O2100C modules of a BIOPAC MP150 system (BIOPAC Systems Inc., CA, USA). For additional details, see Lajoie et al. [163].

Prior to the imaging session, all participants underwent a hypercapnic manipulation of 2 minutes outside of the scanner for familiarization. Thereafter, participants were interviewed to evaluate their level of respiratory discomfort and to confirm their willingness to continue. Participants who reported a significant discomfort were not invited to continue with the imaging session of the study (10 in the AD group, 6 in the control group).

4.4.2.2. Image Acquisition

Acquisitions were performed on two different clinical 3 T scanners of identical make and model (Siemens TIM TRIO, Siemens Medical Solutions, Erlangen, Germany), using a 32-channel receive-only head coil supplied with this system. It was ensured that an equal number of participants from each group were scanned at each site (Table 1, Pearson Chi-Square *P* value of 0.96). Hence, no adjustment for different sites was performed during the statistical analysis. Participants were asked not to consume caffeine or tobacco for two hours prior to their imaging session, to avoid confounding vasoactive effects.

The scan session included a 5-minute anatomical acquisition (1 mm^3 MPRAGE with TR/TE/flip angle = 2.3 seconds/3 msec/9°, 256x240 matrix, GRAPPA factor = 2), and an 18-minute functional scan using dual-echo pseudo-continuous ASL sequence (de-pCASL) [108] in order to acquire simultaneous measures of BOLD and CBF. The de-pCASL parameters

were: TR/TE1/ TE2/alpha = 4.12 seconds/8.4 msec/30 msec/90°, labeling duration = 2 seconds using Hanning window-shaped RF pulse with duration/space = 500 μsec/360 μsec, flip angle = 25°, slice-selective gradient = 6 mT/m, label offset = 100 mm below the center of image slab, nominal and average post-labeling delay (PLD) = 0.9 and 1.44 seconds respectively. The readout consisted of a GRE-EPI with GRAPPA factor = 2, partial sampling of k-space = 7/8, in-plane resolution of 4.5 x 4.5 mm^2, 21 slices with 4.5 mm thickness and 0.5 mm gap.

4.4.3. Data Analysis

4.4.3.1. Respiratory Data Analysis

Analysis of the respiratory data was carried out using a custom software application developed in Matlab (MathWorks, Natick, MA, USA), which performed automatic determination of the end-expiratory (end-tidal (ET)) and end-inspiratory points from the continuous O_2 and CO_2 sampling. Each ET point was corrected to account for the low-pass filtering effect of the filter placed in series and to account for an expired partial pressure of water of 47 mmHg (Severinghaus 1989). For more details, see Lajoie et al. [163].

The average values of ETO_2 at baseline and during both respiratory stimuli were used to compute arterial O_2 content (ml O_2/ml blood) as well as the change in venous deoxygenated fraction ([dHb]/ $[dHb]_0$), as detailed by Chiarelli et al. [56] and Gauthier et al. [85]. The latter quantities are needed to obtain the BOLD calibrated value *M*, resting OEF and $CMRO_2$ as specified below.

4.4.3.2. Image Data Preprocessing

Analysis of functional scans was performed using in-house software implemented in C as in Lajoie et al. [163]. The susceptibility artifacts caused by the paramagnetic molecular O_2 that was inspired, compounded by thick slices used to maximize SNR, limited the image quality of regions on the ventral surface of the brain and those adjacent to the nasal cavity. These regions were excluded from the analysis by empirically determining a threshold in the intensity normalized S0 (label and control averaged) that delineate them. The ASL signal was converted into physiological units of flow (mL/100 g/min) as in Wang et al. [93] with a blood-

brain partition coefficient = 0.9, labeling efficiency = 0.85, blood T_1 = 1.65 seconds, grey matter T_1 = 1.4 seconds [112] and an adjusted PLD to account for slice acquisition time (PLD range for 21 slices of 900-1960 ms). The control S0 at baseline was used as a surrogate for the fully relaxed magnetization M0. In order to compensate for incomplete recovery of longitudinal magnetization during our TR of 4.12 seconds, a factor implicating the grey matter T_1 value was applied to the baseline EPI estimates [112].

In general, the CBF response to hyperoxia is known to be small [84], but small regional changes are difficult to measure due to the low SNR of ASL. Because of this, a uniform change in CBF was assumed throughout the brain, based on averaging of global responses over all participants (the ultimate effect on accuracy is minimal due to the small effect size) [56,64,84,85]. The result of averaging all participants' grey matter $\Delta\%CBF_{HO}$ corrected for blood T_1 was -2%, as described next. During hyperoxic manipulation, the T_1 of blood is altered due to an increase in plasma concentration of paramagnetic O_2 [89]. To account for this change in blood T_1, which biases the measured CBF changes, a corrective factor using the approach described in Chalela et al. [91] and Zaharchuk et al. [92] was applied. First, arterial blood T_1 values during hyperoxic periods were linearly interpolated based on the individual ETO_2 measurements, used as a surrogate for arterial partial pressure of O_2 (PaO_2), along with the R1 ($1/T_1$) and PaO_2 relationship in rats' blood reported by Pilkinton et al. [89]. Then, the individual blood flow maps during hyperoxia were corrected by applying a slice-wise corrective factor based on the quantitative blood flow equation [93], slice acquisition time and adjusted T_1 value.

4.4.3.3. Computation of $CMRO_2$

For each gas challenge, the changes in the venous deoxygenated fraction, along with the changes in BOLD ($\Delta R2^*$) and CBF were used as inputs to the generalized calibration model (GCM), described in Gauthier et al. [59]. This yields a system of two equations with two unknowns: the BOLD calibration parameter *M* (extrapolated maximum BOLD fractional signal increase when venous O_2 saturation approaches 100%) and OEF (the fraction of delivered oxygen that is consumed). Absolute $CMRO_2$ was then determined by multiplying OEF by O_2 delivery, computed as the product of resting CBF by arterial O_2 content. In the

absence of an intersection between the hypercapnia and hyperoxia curves, the voxel is determined to have no solution and will be excluded from any further analysis. In the equation defining M (Gauthier and Hoge [59], equation 7), the parameter α, which expresses the relationship between changes in blood flow and blood volume, was assumed to be 0.18 [70] while β, defining the non-linear dependence of changes in R2* on deoxygenated hemoglobin, was set to 1.5 [71]. The hemoglobin concentration [Hb] was measured from blood drawn from each participant during the scanning session. Metabolic changes associated with periods of hypoxia and hypercapnia remain a topic of debate [77-79,81-83]. Without a clear consensus on the matter, an isometabolism was assumed as in previous calibrated studies [85,94,163].

4.4.4. Statistical Analysis

Regional-based analysis was performed in each individual's original image space (i.e. no spatial resampling). Regions of interest (ROIs) included bilateral grey matter regions for each of the four lobes as defined by the ICBM152 lobes atlas [171], which was non-linearly registered to the ADNI template [172]: frontal, parietal, temporal and occipital, as well as two sub-regions known to be vulnerable to AD [173], i.e. posterior cingulate and precuneus defined from the OASIS-TRT-20 atlas [114]. Given the low SNR in ASL, averaging within lobes was a reasonable compromise in terms of specificity and sensitivity, while allowing for coverage of most of the data and avoided the more arbitrary definition of smaller regions. A region including all four lobes was also created to evaluate measurements throughout cerebral grey matter. A probability mask of grey matter was automatically extracted from T_1-weighted scans using the FMRIB Software Library (FSL) [113], then resampled to the functional EPI scans. Each ROI was also registered to the resolution of the functional EPI scans before being further masked using the individual's grey matter probability map to exclude voxels with a grey matter probability lower than 50%. The ROIs and grey matter probability maps were then used to compute weighted averages for each metric. This weighting procedure served to account for the partial volume effect due to the presence of a mixture of grey matter, white matter and cerebrospinal fluid in EPI voxels. Missing data due to differences in imaged slice positions, susceptibility patterns, or no-solution patterns for M and OEF, were not included in the average. ROI analyses between groups were performed using Matlab (Mathworks, Natick, MA) by applying a univariate general linear model with $P < 0.05$ level of significance. Since

age is known to be a predominant factor in cerebral hemodynamics changes [94,97], results were obtained with and without adjustment for age.

A voxel-wise analysis was also performed to corroborate results of the ROI-based analysis. Individual maps were non-linearly registered, with 12 degrees of freedom using trilinear interpolation, to the ADNI atrophy-specific MRI brain template created from a subset of cognitively normal subjects, patients with mild cognitive impairment (MCI) and patients with mild AD dementia [172]. The non-linear registration was calculated using the CIVET software package [120] via the CBRAIN interface [121]. Brain coverage in normalized group-average data was somewhat limited due to inter-individual differences in: 1) image volume coverage, 2) patterns of susceptibility artifacts, and 3) no-solution patterns for M and OEF. To help correct for these effects, missing data within each participant was interpolated to the respective group-average value and the analyzed region only included voxels where a minimum of 20 participants per group had a valid value. Parametric images were then tested for significant difference between groups by performing a grey matter voxel-wise analysis using SPM12, including age as a covariate. Statistical parametric maps were assessed for cluster-wise significance using a cluster-defining threshold of $P = 0.005$ (uncorrected), while the 0.05 FWE-corrected critical cluster size was set to a minimum of 1250 voxels (voxels of $1x1x1mm^3$). If needed, the cluster size was adjusted to eliminate clusters that were not large enough to reach significance according to the SPM model. A toolbox for SPM was employed to identify the location of clusters, by calculating the percentage of cluster within each region (Tzourio-Mazoyer et al. 2002). The two highest percentages per cluster are reported.

Correlations between Montreal Cognitive Assessment (MoCa) scores and our imaging findings in AD were tested for significance using Spearman's rank-order correlations, with statistical significance set at P 0.05. Correlation with MMSE scores was not performed since these tests were obtained prior to the present study.

4.5. Results

4.5.1. Participant demography

The demographic characteristics of the participants are shown in Table 4.I. We obtained a very good segregation between the two groups based on their respective Montreal Cognitive Assessment (MoCa) score. The difference in age between our groups neared significance, which supports the need to correct for its effect on the different hemodynamic parameters.

	Control	AD	*P* value
Number of subjects	37	34	-
Sites (#1/#2)	27/10	25/9	$P^a = 0.96$
Gender (male/female)	14/23	15/19	$P^a = 0.59$
Age (years)	74.4 ± 4.6	76.9 ± 6.5	$P^b = 0.07$
Education	16.4 ± 3.5	14.6 ± 4.6[c]	$P^b = 0.09$
Mini-Mental State (MMSE)*	-	23.7 ± 2.6	-
Montreal Cognitive Assessment (MoCa)	28.5 ± 1.2	15.6 ± 5.0	$P^b < 1x10^{-14}$

Table 4.I. Demographic and clinical data for each group

Data are means ± standard deviations.

* Performed in AD prior to the current study; was part of the inclusion criteria

[a] Pearson Chi-Square *P* value

[b] Two-sided independent sampling Student *t*-test *P* value

[c] Education information was missing in five AD patients

4.5.2. Susceptibility Artifacts

As expected, with the presence of paramagnetic molecular oxygen in inhaled air situated in the frontal sinuses and nasal cavity, the temporal lobe was the main region in which voxels were excluded due to susceptibility artifacts: a reduction of 4% in the number of voxels (having a minimal grey matter probability of 50%) was observed. The number of voxels in the occipital and frontal lobes reduced by less than 1%, while the parietal lobe was not affected.

4.5.3. Delayed Arterial Transit Time

We compared resting CBF, OEF and $CMRO_2$ values within the four grey matter lobes (Figure 4.2) with that of previous ASL [51,115] and PET studies [14,16,17,174]. Our values are in good general agreement with previous studies, except in the occipital lobe where our estimates are lower in both groups. The occipital lobe is known to be served by the posterior

cerebral artery, which has a substantially longer transit time [149,151,175]. Therefore we suspect our CBF estimates to be biased in this area only due to a short PLD. Conjointly, higher CBF delta percent change during hypercapnia in the occipital lobe compared with the other lobes was also observed and supports this theory (data not shown). This bias in resting CBF and in flow change to hypercapnia propagates to the model-derived *M*, OEF and $CMRO_2$, which prevents us from making any conclusions in the occipital lobe. Therefore, we chose not to include the occipital lobe in subsequent analyses.

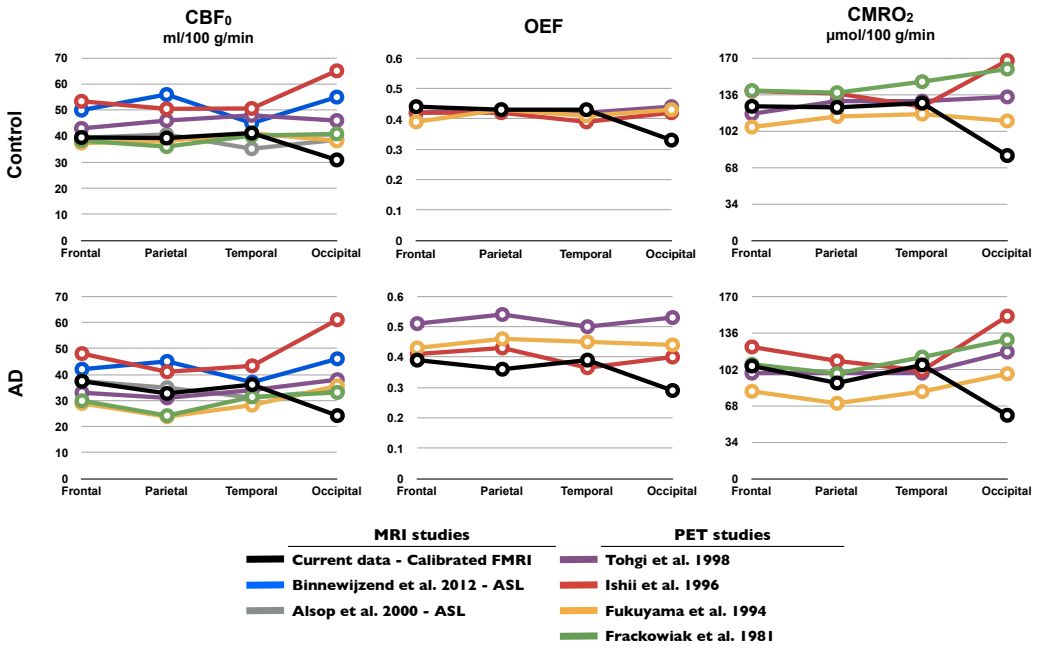

Figure 4.2. Bias in occipital lobe due to delayed arterial transit time (ATT)
Our resting CBF, OEF and $CMRO_2$ values within each grey matter lobe are compared to those found in the literature. Measurements fall within the range of reported values, excepting in the occipital where the ATT is suspected to be longer than our time acquisition, biasing our ASL measurements and thus the derived-model *M*, OEF and $CMRO_2$ estimates in this region. ***CBF_0*** = the resting oxygen delivery; ***OEF*** = the oxygen extraction fraction; ***$CMRO_2$*** = the resting oxygen consumption

4.5.4. Patients Versus Healthy Control Subjects

4.5.4.1. Respiratory Data

Figure 4.3 shows the O_2 and CO_2 end-tidal values (ET) at baseline, during hyperoxia (HO) and hypercapnia (HC) in both groups. No significant differences in respiratory measurements were found between the groups ($P_{ETO2\_0} = 0.5$, $P_{ETO2\_HO} = 0.2$, $P_{ETO2\_HC} = 0.8$, $P_{ETCO2\_0} = 1.0$, $P_{ETCO2\_HO} = 1.0$, $P_{ETCO2\_HC} = 0.8$, adjusted for age).

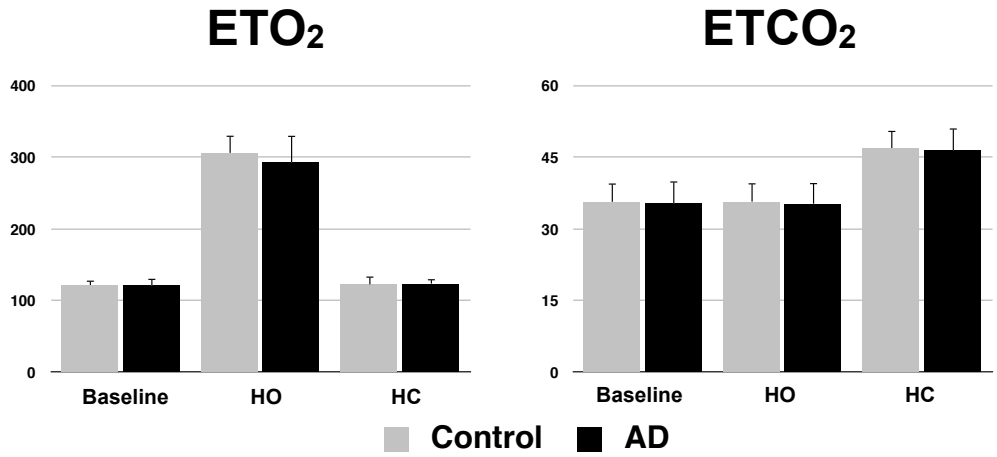

Figure 4.3. Gas manipulations
End-tidal (ET) O_2 and CO_2 values at baseline, during hyperoxia (HO) and during hypercapnia (HC) for both groups. Errors bars indicate standard deviation.

4.5.4.2. Hemoglobin concentration and T_1 corrected CBF change during hyperoxia

The blood test revealed no significant difference in the hemoglobin concentration ([Hb]) between groups ($P = 0.4$ adjusted for age), with an average of 13.9 ± 1.4 and 13.9 ± 1.2 gHb/dl in the patient and control cohorts respectively. Individual values of [Hb] were used in the QUO2 model for M, OEF, and $CMRO_2$ estimation. Blood T_1 during hyperoxia was estimated to be 1.593 ± 0.015 and 1.587 ± 0.011 seconds in AD and controls respectively. These were not significantly different ($P = 0.2$, adjusted for age). As a result, the grey matter cortical group-averaged T_1-corrected CBF values during hyperoxia were -1.7 ± 10.9 and -2.6 ±

8.9% in AD and controls respectively, with no significant difference between them (P = 0.9, adjusted for age). Considering the low SNR associated with these measurements, the T_1-corrected $\Delta\%CBF_{HO}$ averaged over both groups (-2%) was employed as a fixed constant in the computation of the model-derived estimates (descriptions in methodology section).

4.5.4.3. Region-wise analysis

Our grey matter region-wise analysis revealed a decreased CBF and $CMRO_2$ in the parietal, precuneus and temporal regions of AD patients compared to age-matched controls (Table 4.II). Interestingly, all investigated lobes and sub-regions showed a lower resting R2* in AD (corresponding to a slower transverse relaxation of the MRI signal). The $R2^*_0$ in AD was also found significantly lower in all investigated lobes and sub-regions. During the hypercapnic manipulation, R2* decreased less in AD (equivalent to a lower BOLD signal increase), in the frontal, parietal and precuneus regions as well as the whole brain. A tendency for a reduced R2* decrease during hypercapnia was observed in the temporal and posterior cingulate cortex, although the differences were not significant after adjustment for age (respectively P = 0.07 and P = 0.06 respectively). Lower OEF values in the parietal, precuneus and the whole brain of AD were not significant after adjustment for age. No region showed a significant difference between groups for the M value, the R2* change during hyperoxia, and the CBF change during hypercapnia. Since the increase in end-tidal CO_2 during hypercapnia was equivalent in both groups, the percent CVR was also not found to be significantly different.

		Frontal	Parietal	Temporal	Precuneus	PC	*Total*[c]
CBF_0	**Control**	39.5 ± 10.8	39.3 ± 13.1	41.2 ± 10.8	37.2 ± 14.4	43.7 ± 11.4	39.8 ± 11.2
	AD	37.4 ± 9.0	32.7 ± 9.8	36.1 ± 8.3	29.2 ± 10.5	39.9 ± 8.6	35.9 ± 8.8
	p^a / p^b	0.37/0.29	**0.02/0.02**	**0.03/0.01**	**0.01/0.007**	0.12/0.08	0.11/0.07
OEF	**Control**	0.44 ± 0.14	0.43 ± 0.14	0.43 ± 0.13	0.42 ± 0.16	0.47 ± 0.15	0.43 ± 0.13
	AD	0.39 ± 0.08	0.36 ± 0.10	0.39 ± 0.10	0.34 ± 0.13	0.45 ± 0.16	0.38 ± 0.08
	p^a / p^b	0.06/0.13	**0.02**/0.08	0.16/0.33	**0.04**/0.12	0.63/0.72	**0.03**/0.09
$CMRO_2$	**Control**	125 ± 44	124 ± 48	128 ± 40	113 ± 55	144 ± 57	124 ± 42
	AD	105 ± 31	89.2 ± 33.6	106 ± 32	75.6 ± 39.2	130 ± 59	99.9 ± 28.6
	p^a / p^b	**0.04**/0.09	**0.001/0.004**	**0.01/0.04**	**0.002/0.007**	0.32/0.37	**0.007/0.02**
M	**Control**	5.11 ± 1.14	5.79 ± 1.95	6.59 ± 1.69	6.32 ± 2.58	6.20 ± 2.32	5.62 ± 1.33
	AD	4.92 ± 1.53	5.12 ± 1.77	6.43 ± 1.39	5.35 ± 1.93	6.32 ± 3.35	5.24 ± 1.36
	p^a / p^b	0.55/0.82	0.14/0.36	0.68/0.76	0.08/0.22	0.86/0.73	0.25/0.57
$R2^*_0$	**Control**	18.0 ± 1.4	17.2 ± 1.5	24.9 ± 1.4	16.9 ± 1.6	16.2 ± 1.1	19.6 ± 1.3
	AD	16.8 ± 1.0	15.9 ± 1.4	24.1 ± 1.4	15.7 ± 1.4	15.1 ± 1.4	18.4 ± 1.1
	p^a / p^b	$\mathbf{1x10^{-4}/5x10^{-4}}$	$\mathbf{3x10^{-4}/2x10^{-3}}$	$\mathbf{3x10^{-3}/5x10^{-2}}$	$\mathbf{6x10^{-4}/3x10^{-3}}$	$\mathbf{2x10^{-4}/9x10^{-4}}$	$\mathbf{1x10^{-4}/7x10^{-4}}$
$\Delta\%CBF_{HC}$	**Control**	53.8 ± 22.8	63.3 ± 49.7	71.8 ± 39.0	69.5 ± 59.6	37.0 ± 27.9	61.0 ± 30.9
	AD	46.5 ± 23.3	62.4 ± 42.6	62.0 ± 33.0	65.3 ± 44.1	29.1 ± 24.7	54.5 ± 26.8
	p^a / p^b	0.20/0.29	0.94/0.88	0.27/0.34	0.74/0.61	0.22/0.35	0.35/0.42
%CVR	**Control**	4.80 ± 1.93	5.45 ± 3.66	6.32 ± 2.87	6.02 ± 4.45	3.24 ± 2.48	5.37 ± 2.31
	AD	5.25 ± 5.47	6.90 ± 7.90	6.34 ± 4.10	7.15 ± 7.66	3.39 ± 4.77	5.91 ± 5.35
	p^a / p^b	0.65/0.72	0.32/0.49	0.98/0.97	0.45/0.71	0.87/0.91	0.58/0.71
$\Delta R2^*_{HC}$	**Control**	-0.57 ± 0.19	-0.77 ± 0.25	-0.65 ± 0.25	-0.91 ± 0.30	-0.62 ± 0.18	-0.64 ± 0.21
	AD	-0.43 ± 0.18	-0.62 ± 0.23	-0.51 ± 0.23	-0.73 ± 0.29	-0.50 ± 0.21	-0.50 ± 0.19
	p^a / p^b	**0.003/0.02**	**0.01/0.04**	**0.02**/0.07	**0.01/0.04**	**0.01**/0.06	**0.004/0.02**
$\Delta R2^*_{HO}$	**Control**	-0.15 ± 0.09	-0.25 ± 0.10	-0.18 ± 0.13	-0.28 ± 0.11	-0.24 ± 0.08	-0.19 ± 0.09
	AD	-0.17 ± 0.09	-0.26 ± 0.10	-0.19 ± 0.13	-0.29 ± 0.12	-0.23 ± 0.08	-0.20 ± 0.09
	p^a / p^b	0.51/0.42	0.66/0.51	0.83/0.59	0.78/0.70	0.74/0.90	0.61/0.44

Table 4.II. Region-wise analysis in grey matter with and without adjustment for age
For each physiological variable, group average values ± standard deviation in different ROIs are reported, as well as Student *t*-test *P* values calculated with and without adjustment for age. *P* values where significance is reached ($p < 0.05$) are shown in bold. Physiological variables are: **CBF_0** (ml/100 g/min), the resting oxygen delivery; **OEF**, the oxygen extraction fraction; **$CMRO_2$** (μmol/100 g/min), the resting oxygen consumption; ***M*** (%) the maximum BOLD signal increase when venous O_2 saturation approaches 100%; **$R2^*_0$** (s^{-1}), the transverse

relaxation rate constant; Δ**%CBF$_{HC}$** (%), the blood flow percent change during hypercapnia; **%CVR** (%), the cerebrovascular reactivity in percent blood change to change in end-tidal CO_2; Δ**R2*$_{HC}$** (s^{-1}), the R2* change during hypercapnia; Δ**R2*$_{HO}$** (s^{-1}), the R2* change during hyperoxia

[a] : Two-sided independent sampling Student t-test P value, without adjustment for age

[b] : Two-sided independent sampling Student t-test P value, with adjustment for age

[c] : Cerebral grey matter excluding the occipital lobe

4.5.4.4. Voxel-wise analysis

The brain volumes included in the grey matter voxel-wise analysis is shown in Figure 4.4, overlaid on different sagittal and axial sections of the ADNI template. Given the biased ASL signal in the occipital lobe, this lobe was also excluded from the analysis. Clusters with significant differences between groups are reported in Figure 4.5 and Table 4.III. No cluster showed significant increases in AD relative to controls. Significant reductions in CBF were observed in the temporal and parietal lobes in AD, including the precuneus and posterior cingulate. Reductions in $CMRO_2$ were observed in the frontal, temporal and parietal lobes, more specifically in the precuneus. Lower OEF and calibrated parameter *M* were also found in the parietal-precuneus, although the sizes of significant clusters were considerably smaller. Also observed in the region-wise analysis, resting R2* was lower in different AD brain regions, such as in bilateral temporal, frontal, parietal, precuneus and posterior cingulate. As for the change in R2* during hypercapnia, only the frontal lobe revealed a significantly smaller decrease in AD relative to controls. Finally, no significant group difference was found for $\Delta R2^*_{HO}$, $\Delta\%CBF_{HC}$ and %CVR.

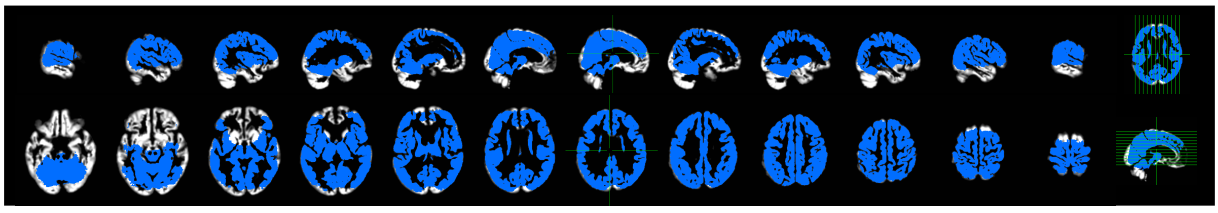

Figure 4.4. Volume of the brain analyzed

Analyzed volume (in blue) only includes voxels where a minimum of 20 participants per group had a valid value. Any remained missing data within the analyzed region were interpolated to the respective group-averaged value. Missing data are due to differences in: 1)

imaged slice position, 2) susceptibility patterns and 3) pattern of no-solutions across subjects. In the axial slices: left=left.

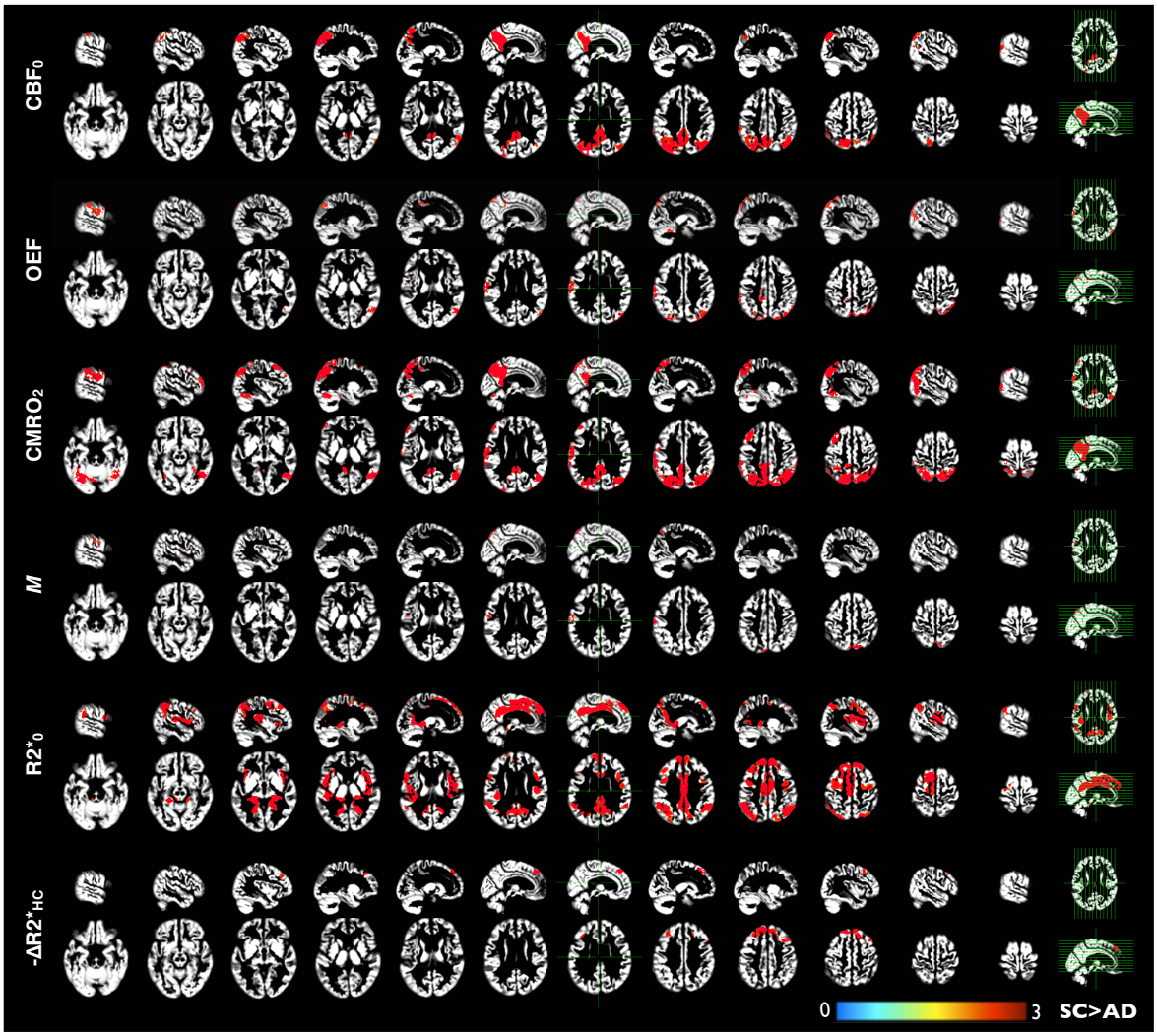

Figure 4.5. Voxel-based analysis adjusted for age

For each physiological variable, the colored regions show a significant deficit in AD (primary $P < 0.005$ and minimum cluster size of 1250 mm^3, yielding a FWE cluster-corrected ($P < 0.05$)). The color bar indicates Student's t-statistic value. Statistically significant clusters are overlaid to different sagittal and axial sections of the ADNI template. Physiological variables are: **CBF_0**, the resting oxygen delivery; **OEF**, the oxygen extraction fraction; **$CMRO_2$**, the resting oxygen consumption; ***M***, the maximum BOLD signal increase when venous O_2 saturation approaches 100%; **$R2^*_0$**, the transverse relaxation rate constant; **$\Delta R2^*_{HC}$**, the R2* change during hypercapnia. In the axial slices: left=left. *SC* = subject control.

	Clusters	*N* voxels	MNI coordinates x,y,z mm	Anatomical areas (First two containing the highest % of the cluster)	%
CBF_0	1	43012	-40 -88 27	Right precuneus	23.85
				Left postcentral	12.37
	2	10652	49 -71 39	Right superior temporal	36.97
				Right superior parietal	20.65
OEF	1	10176	55 -71 11	Right inferior parietal	25.30
				Right inferior temporal	24.45
	2	4852	-67 -14 26	Left inferior parietal	45.98
				Left superior temporal	21.91
	3	2148	-2 -76 52	Left superior parietal	23.74
				Left precuneus	19.69
	4	1699	11 -42 -32	Right Cerebellum	47.32
				Right Cerebellum	30.37
	5	1552	-13 -40 47	Left precuneus	52.26
				Left supplementary motor area	28.03
$CMRO_2$	1	95725	53 -67 -13	Right precuneus	13.16
				Right superior parietal	8.76
	2	2813	-55 36 8	Left inferior pars triangularis	41.41
				Left middle frontal	7.18
	3	4491	-25 31 56	Left superior frontal	4.24
				Left middle frontal	3.07
	4	8699	-29 -74 -26	Vermis	50.39
				Left inferior temporal	29.82
M	1	2107	8 -75 54	Right precuneus	28.14
				Left precuneus	24.35
	2	1799	-67 -13 33	Left supramarginal	67.54
				Left heschl	12.51
$R2^*_0$	1	21132	46 -9 10	Right postcentral	23.51
				Right insula	18.90
	2	14888	-48 6 -2	Left insula	25.91
				Left superior temporal pole	18.48
$-\Delta R2^*_{HC}$	1	6094	-9 39 53	Left inferior pars triangularis	35.58
				Left middle frontal	35.12
	2	6115	8 44 50	Right inferior pars opercularis	31.81
				Right middle frontal	29.84

Table 4.III. Clusters with significant difference (control > AD) adjusted for age

For each physiological variable, significant clusters are reported. Physiological variables are: **CBF_0**, the resting oxygen delivery; **OEF**, the oxygen extraction fraction; **$CMRO_2$**, the oxygen consumption; ***M***, the maximum BOLD signal increase when venous O_2 saturation approaches 100%; **$R2^*_0$**, the transverse relaxation rate constant; **$\Delta R2^*_{HC}$**, the R2* change during hypercapnia.

4.5.4.5. Correlation between QUO2 findings and AD MoCa scores

MoCa scores were only significantly correlated with $R2^*_0$ in the whole brain grey matter (occipital lobe excluded) and temporal cortex (r = 0.37, P = 0.04 ; r = 0.36, P = 0.04 respectively) (Table 4.IV). MoCa scores correlation with $R2^*_0$ in the posterior cingulate and CBF_0 in the precuneus approached significance (r = 0.34, P = 0.06 ; r = 0.32, P = 0.07 respectively).

	Frontal	Parietal	Temporal	Precuneus	Posterior cingulate	*Total*[a]
CBF_0	-0.05 (0.79)	0.20 (0.28)	0.29 (0.11)	0.32 (0.07)	-0.04 (0.84)	0.06 (0.75)
OEF	-0.05 (0.80)	0.12 (0.50)	-0.03 (0.85)	0.12 (0.53)	-0.23 (0.20)	0.04 (0.83)
$CMRO_2$	-0.01 (-0.94)	0.20 (0.28)	0.12 (0.50)	0.29 (0.10)	-0.24 (0.19)	0.05 (0.77)
M	-0.05 (0.80)	0.06 (0.74)	0.00 (0.98)	0.15 (0.41)	-0.21 (0.25)	0.02 (0.90)
$R2^*_0$	0.25 (0.16)	0.22 (0.22)	0.36 (0.04)*	0.16 (0.39)	0.34 (0.06)	0.37 (0.04)*
$\Delta\%CBF_{HC}$	-0.14 (0.45)	-0.17 (0.34)	-0.14 (0.42)	-0.13 (0.49)	0.08 (0.65)	-0.16 (0.38)
%CVR	-0.14 (0.46)	-0.18 (0.34)	-0.16 (0.38)	-0.12 (0.51)	0.1 (0.59)	-0.21 (0.25)
$\Delta R2^*_{HC}$	0.12 (0.51)	-0.03 (0.87)	0.14 (0.45)	-0.06 (0.73)	-0.02 (0.93)	0.09 (0.63)
$\Delta R2^*_{HO}$	0.09 (0.61)	0.08 (0.68)	-0.04 (0.82)	0.09 (0.62)	0.01 (0.96)	0.09 (0.62)

Table 4.IV. Correlation between physiological variables in grey matter and MoCa scores in AD

Values represent the Spearman correlation coefficients (P value) between the Montreal Cognitive Assessment (MoCa) scores and the physiological variables in AD. Physiological variables are: **CBF_0**, the resting oxygen delivery; **OEF**, the oxygen extraction fraction; **$CMRO_2$**, the resting oxygen consumption; ***M***, the maximum BOLD signal increase when venous O_2 saturation approaches 100%; **$R2^*_0$**, the transverse relaxation rate constant; **$\Delta\%CBF_{HC}$**, the blood flow percent change during HC; **%CVR**, the cerebrovascular reactivity in percent blood change to change in end-tidal CO_2; **$\Delta R2^*_{HC}$**, the R2* change during hypercapnia; **$\Delta R2^*_{HO}$**, the R2* change during hyperoxia.

* $P < 0.05$

[a] Cerebral grey matter excluding the occipital lobe

4.6. Discussion

In this study, we investigated whether our QUO2 technique was sensitive to differences in vascular and metabolic function in AD. This calibrated fMRI technique has the advantage of providing quantitative information while being readily integrated with other MRI measures

(i.e. structural MRI) of proven value in AD, and may therefore offer new insights into the underlying mechanisms and causes of the disease.

Although the QUO2 model-derived parameters and MoCa scores in AD were not significantly correlated, vascular and metabolic deficits in AD may be associated with other cognitive scores including: language, verbal reasoning, visuospatial function, as well as visual, short-term and working memory. Correlations between these neuropsychological scores and our imaging findings will be evaluated in a subsequent paper.

4.6.1. Patients versus controls

The hypoperfusion in AD observed in our data supports its relevance as a pathophysiological change in AD [10,176] and is consistent with findings from a previous ASL studies [51,53,54,115]. The absence of significant differences in the frontal lobe blood flow (39.5 ± 10.8 vs. 37.4 ± 9.0 ml/100 g/min) is consistent with an AD-like pattern, as opposed to vascular dementia [15]. With a power of test of 80%, our minimum detectable difference (MDD) in frontal lobe blood flow was 7 ml/100 g/min. Our data showed a coupled parietotemporal pattern of hypoperfusion and hypometabolism in AD, which corresponds to findings in previous PET studies [14-16], including changes in the precuneus, an area where blood flow and glucose use was shown to decline at a very early stage in AD [51,54,118,177,178]. Although the coupling of blood flow and metabolism in AD may imply that the CBF measurement alone is a reliable way of looking at the cerebral function, evidence for some decoupling was previously reported [179], hence, both measurements remain pertinent especially when exploring the causal factors of the disease or assessing response to treatment. For instance, by comparing the MRI oxygen uptake to the PET FDG glucose uptake, one could compute a brain glycolytic index that would flag regions where the oxygen metabolism, and thus indirectly the mitochondrial function, is being compromised and may contribute to the progression of the disease [5-9].

Our voxel-wise analysis on OEF indicated a significant decrease in the AD cohort, within the parietal lobe, while our region-wise analysis reported no significant differences after correction for age (MDD_{Total} = 0.09). Results in the literature are inconsistent regarding

OEF with some studies failing to find a difference [17,174], others noting a decrease in the medial temporal [14], and still others suggesting an increase in the parietal cortex [16]. The coupled reduction in CBF and $CMRO_2$ along with the absence of increased OEF tends to rule out chronic global cerebral ischemia in our AD patients, at least at this stage of the illness.

A trend toward lower calibrated BOLD *M* values in aging has been previously observed [94-97], while, to our knowledge, this study represents the first determination of the *M* value in an AD cohort. The *M* value is determined largely by the baseline deoxyhemoglobin (dHb) brain content. If resting dHb content in the brain is different between two groups, standard BOLD measures must be interpreted with caution, since a task-related BOLD signal increase will depend partly on the baseline dHb. In the present study, we found few differences difference between groups on a voxel-wise basis and no significant difference was found between regions (MDD_{Total} = 0.9%). This finding tends to support the use of BOLD as a comparative biomarker between the two groups studied.

The observed reduction in transverse relaxation rate constant in AD relative to control was unexpected. Iron, by its paramagnetic nature can increase the R2* effect and it is known to be higher in AD, most notably in sub-cortical regions and hippocampus [180], which were not considered in the present analysis. The presence of more brain atrophy in AD [26-29,181] might explain a lower R2* due to the greater inclusion of cerebrospinal fluid in our voxel-wise and regional analyses. In the present study, we sought to limit such partial volume errors by weighting our ROI-averaging with the maps of grey matter fraction determined from individual T_1-weighted image. Otherwise, lower R2* in AD may be due to less deoxygenated hemoglobin or a better shim due to the grey matter being further away from scalp (due to atrophy).

Another interesting finding is the absence of significant differences in percent CVR between our AD and control groups (MDD_{Total} = 1.56%). Nagata et al. [15,179] made the same observation while comparing the vascular reactivity to carbon dioxide inhalation between a group of probable AD, a group of patients with vascular dementia (VaD) and a group of age-matched controls. They found that while the CVR was depleted in the VaD group, it remained normal in the AD group. Our results are consistent with the latter finding, suggesting physiological changes specific to AD rather than vascular dementia.

4.6.2. Limitations

Analyses were performed solely on the basis of the participant's clinical diagnostic status, without taking into account the vascular density or vascular lesion burden that may play a role in the observed results. We will follow up on this in a subsequent paper, while taking into account the fluid-attenuated inversion recovery (FLAIR) and susceptibility-weighted imaging (SWI) scans that were acquired during the MRI session.

During the hypercapnic testing, 10 out of 59 patients (17%) and 6 out of 60 controls (10%) withdrew due to the feeling of anxiety caused by the CO_2 inhalation. Previous studies of respiratory manipulation in our research group [94,163] showed a lower rate of withdrawal associated with periods of hypercapnia. However, the previous study included only healthy participants in their sixties (64 ± 5 years) or younger (31 ± 6 years), while the present participants were in their seventies (group-average age of 76 ± 6 years). Younger participants are, understandably, more comfortable with the procedure than elderly participants and AD patients. It is likely that a clinical trial would experience a lower rate of dropouts among a cohort of mild cognitive impairment (MCI) patients than within a group of AD patients. Also, dropouts were apparent predominantly in the beginning of the study, decreasing from 17% of participants in the first half of the study to 10% of participants in the second half. As time passed, study coordinators got better at identifying potential participants who, by virtue of cognitive or other deficits), were less likely to tolerate the protocol (although this admittedly constitutes a selection bias). Moreover, testing protocol (which included a blood test, the neuropsychological battery, the hypercapnia test and MRI scan) was performed during a single visit. Future calibrated studies may consider planning for a separate day to perform the hypercapnia testing alone, thus reducing potential stress and fatigue experienced by the participants.

Our cohorts' size was also diminished due to either the presence of mask leakage or malfunction of the monitoring system (which affected data for 10 patients and 7 controls), which may be seen as problematic in the context of a trial. Malfunction of the monitoring system consisted of a failing O_2 pump at some point during the first half of the study, and can be considered as an isolated event since no more difficulties were observed following its repair. The leaks were either due to an imperfect fit of the mask to the participant's face, or

small fissures in the valves of the gas system circuit. The fissures in the valves were the result of a manufacturing defect in a specific batch of breathing circuits. Hence, it is unlikely that future clinical trials would experience the same challenge. Also, as time passed, experimenters became experienced at identifying leaks during the acclimation task before the imaging session and hence were able to fix it by either re-positioning the mask, employing skin tape to eliminate any remaining apertures or replacing the defective valve. Data exclusion due to technical challenges passed from 22% in the first half of the study to 5% in the second half.

Although our detectable effect is limited by our final cohort sizes (AD = 34, Control = 37), which in turn limits the statistical power, the clear segregation of the two groups based on their MoCa score (15/30 vs. 28/30) suggests that the observed effects are specific to AD.

Potential confounds can be associated with the use of the same value of certain model parameters in both groups. Among the parameters commonly assumed in calibrated fMRI studies, we find the Grubb coefficient α, the parameter β, the hemoglobin concentration ([Hb]), the change in metabolism during hypercapnia and hyperoxia ($\Delta CMRO2_{HC}$ and $\Delta CMRO2_{HO}$, respectively), as well as the change in blood flow during hyperoxia (ΔCBF_{HO}, directly associated with the arterial blood T_1 during HO). In a previous study [163], the sensitivity of the model-derived M, OEF and $CMRO_2$ estimations to the above assumed parameters was assessed. It was shown that M was mainly affected by systematic errors in β and $\Delta CMRO2_{HC}$, while not much impacted by [Hb], $\Delta CMRO2_{HC}$ and ΔCBF_{HO}. On the other hand, OEF was mostly influenced by the assumed $\Delta CMRO2_{HO}$, whereas not affected much by errors in β. Finally, $CMRO_2$, being the product of CBF_0, OEF and arterial O_2 content, was impacted the same as OEF for all assumed parameters, except for [Hb], which is part of the arterial O_2 content estimation.

In the present study, a blood test allowed the measurement of individual [Hb] and thus eliminated a potential source of systematic error that could have impacted OEF and $CMRO_2$ (Figure 11-B in Lajoie et al. [163]). No difference was found between groups and the mean [Hb] of 13.9 ± 1.3 gHb/dl is in agreement with literature values in aged population [75,76]. Concerning the change of blood flow during periods of hyperoxia, we applied, for each participant, a T_1-correction and noted no significant difference in the resulted grey matter $\Delta\%CBF_{HO}$ between groups. The averaged value over all participants was employed as the

fixed constant value of $\Delta\%CBF_{HO.}$ Finally, possible divergence of the 'true' values of the remained assumed parameters, between groups, could have induced potential errors in our group comparison. Future studies on Alzheimer's disease could help answer this question by determining, for instance, if the metabolism of AD is differently altered during periods of hypercapnia, or if the vascular compliance, and thus the Grubb coefficient α that defines the relation between blood flow and volume, is different in AD patients.

Our lower CBF_0 and higher $\Delta\%CBF_{HC}$ found in the occipital lobe are indicative that for a majority of participants, our post-labeling-delay (PLD) was insufficient due to the longer transit time of the artery serving the occipital lobe. When quantifying the blood flow, as long as the PLD is equal or higher than the time taken by the blood bolus to travel from the labeled slice to the imaged tissue, or arterial transit time (ATT), the exact value of the latter does not matter since the CBF measurement will not be biased by incomplete label delivery. The ATT is known to lengthen with age [175,182], to vary within brain regions served by different major cerebral arteries [149,151,175], to differ between grey matter and white matter, and to decrease under hypercapnic manipulation [151]. Since the ASL signal decays rapidly with time, employing a PLD value high enough to overtake the ATT under all conditions, participants and regions, would be costly in terms of SNR. Therefore, the choice of PLD is a compromise between SNR, sensitivity and specificity. In this study, we opted for a moderate PLD ranging from 900 msec and 1986 msec (given the different slice acquisition times), resulting in a brain averaged PLD of 1443 msec, which is lower than the whole brain PLD of 2000 msec later recommended by the ASL community [112]. Our decision was based on 1) the presence of a hypercapnic manipulation in our study, which is known to accelerate the blood flow and therefore to lower the ATT, 2) the loss of SNR that we would experience in the upper slice if increasing the whole range of PLD values and 3) the fact that our analysis was based on grey matter tissue for which the PCASL is less sensitive to the ATT due to the small difference in T_1 of blood and grey matter [183]. To avoid such a bias in the occipital lobe associated with the imaging of blood prior to its complete delivery, one could obtain the individual baseline and hypercapnic ATT maps using a rapid low-resolution multi-PLD acquisition such as in Dai et al. [184] to compute the true CBF value. Another solution would be to increase the PLD, while decreasing the number of slices such that the upper slices are not

affected by a low SNR due to an excessively high ASL signal decay [97,185]. The use of simultaneous multi-slice acquisition may also help limit T_1 decay of the ASL label signal over the volume.

4.7. Conclusion

Our project, in addition to examining pathophysiological changes in AD using calibrated fMRI, helped identify some key challenges related to calibrated fMRI such as the choice of the post-labeling-delay parameter to limit any flow-related bias due to delayed arterial transit time, the presence of susceptibility artifacts, and the challenge associated with the hypercapnic manipulation in elderly participants, particularly those affected by dementia. Current challenges include: improving the characterization of vascular and metabolic burdens in the AD brain, along with providing additional information such as the transverse relaxation rate constant R2* and cerebrovascular reactivity to CO_2. Future calibrated fMRI studies, in which the latter challenges are overcome, may provide new insights into the pathophysiology of AD that go beyond hyperphosphorylated tau pathology, amyloid deposition and glucose uptake. Moreover, calibrated fMRI may be of value in monitoring disease progression, in differentiating AD from vascular dementia, and for exploring mitochondrial dysfunction as a potential causal factor for the disease.

4.8. Acknowledgments

The authors want to thank Anne-Marie Bédard and Lucile Sinck for their excellent coordination and management work all along this study. Michel Houde is acknowledged for his valuable quality assurance assistance. We thank Carollyn Hurst, André Cyr, Louise Marcotte, Ron Lopez, David Costa, André Cormier, Marius Tuznik, Bahare Sabouri, Michael Ferreira and Ilana Leppert for their help in data acquisition and their excellent technical assistance. Santiago Paiva is acknowledged for his administrative assistance. Jiongjiong Wang at UCLA is also acknowledged for providing the pseudo-continuous arterial spin-labeling sequence. This work was supported by the Canadian Institutes of Health Research [MOP 123492]; the Canada Foundation for Innovation [17380]; the Natural Sciences and

Engineering Research Council of Canada [R0018142]; and the Consortium québécois sur la découverte du médicament (CQDM).

5. General discussion

There is an increased interest in the exploration of vascular and metabolic burden in Alzheimer's disease. The recent development of calibrated fMRI approaches, such as QUO2, that go beyond the relative measurements of oxidative metabolism to yield absolute resting measurements, is of particular interest in better understanding AD and its discrimination from other etiologies such as vascular dementias. The absolute measurement of $CMRO_2$ from calibrated fMRI techniques, rather than from PET, has the advantages that it is much more accessible and does not necessitate the injection of radioactive tracers. Furthermore, in addition to O_2 delivery and consumption, the QUO2 technique provides supplementary physiological biomarker candidates for AD such as the transverse relaxation rate constant and cerebrovascular reactivity. Moreover, one could study the presence of correlations between the QUO2 estimates and other measurements performed concurrently within the same modality (for example: structural, connectivity or task-evoked measurements). Prior to applying the QUO2 approach to an AD population, there was a need for enhancing the quality of single-subject QUO2 estimates, while assessing the accuracy and precision of the model-derived estimates.

In order to enhance single-subject QUO2 measurements, image analysis techniques along with the respiratory and ASL protocol were first revisited. A novel breathing circuit made in-house was also introduced [66] and used throughout the present work. The resultant apparatus yielded precise fractional concentrations of inspired O_2 and CO_2, while being secure and easy to place and remove. The reproducibility of the respiratory trace and of the BOLD/ASL signals in whole-brain GM was assessed [67], revealing robust and consistent measures (CV < 10%), with CBF hypercapnic responses being the most variable (CV < 20%). Thereafter, the variability of QUO2 estimates as well as the impact of errors on their accuracy and precision were evaluated and presented in Chapter 2. It was shown that M, OEF and $CMRO_2$ precision would particularly benefit from a reduced error in CBF hypercapnic response measurement. Additionally, the assumed model parameters that had the largest

impact on the accuracy of *M* were the metabolic changes during HC and the beta parameter. Meanwhile, for OEF and $CMRO_2$, the greatest impact was from metabolic changes during both gas challenges, and the CBF hyperoxia response. In chapter 3, we compared the impact of employing 60% versus 100% inspired O_2 on the model-derived estimates. No difference was found between the number of voxels affected by susceptibility artefacts and the QUO2 model-derived estimates remained comparable regardless of the hyperoxia level. Finally, in chapter 4, the QUO2 method was applied in a cohort of AD patients and a group of age-matched controls. Results revealed the typical parietotemporal pattern of hypoperfusion and hypometabolism in AD, along with providing additional information such as the transverse relaxation rate constant R2* and the cerebrovascular reactivity to CO_2, making the QUO2 approach a promising aid in the understanding, diagnosis and monitoring of the disease.

5.1. Future directions

QUO2 model-derived *M*, OEF and $CMRO_2$, as being estimated from BOLD and CBF measurements, suffer from the low intrinsic SNR of ASL measures. Additionally, small head-motion or instability in either the control or label image may result in perfusion image errors. When being applied in a less compliant clinical population, such motion can become a significant cause of image degradation. We have compared the BOLD and ASL SNR and CNR of the QUO2 protocol (Table 4, Tancredi et al. [67]) and shown that our BOLD SNR was considerably higher than that of ASL (224±9 vs. 2.5±0.1 respectively), while the average CNR of BOLD hypercapnic responses were 3 times larger than that of CBF responses (3.9±0.3 vs. 1.32±0.06), reflecting the higher temporal stability of the BOLD signal. As a consequence, the within-subject variability of CBF responses was larger than that of the BOLD responses with a general trend for higher variability in smaller regions (Table 2.IV, Chapter 2). Finally, the impact of such errors in measured CBF responses on the precision of the model-derived estimates was shown (Figure 2.12, Chapter 2). Enhancing the robustness and reliability of ASL would therefore improve M, OEF and $CMRO_2$ estimates at a single subject level and in small regions. Available strategies include the suppression of background static tissue signal [159,160], the correction of spin labeling imperfections [152] and of B0

field inhomogeneity [153], the elimination of physiological noise [146,186] and the application of improved partial volume correction [154,187].

While our post-labeling-delay (PLD) was optimal for a protocol which included periods of hypercapnia in a healthy young population (Chapter 2 and 3), our ASL data on elderly and Alzheimer's patients revealed a bias in the occipital lobe, where the arterial transit time is known to be longer (Figure 4.3, Chapter 4). Future calibrated fMRI applications on such cohorts would benefit from either one of the following adjustments: 1) increasing the PLD to give enough time for labeled blood to enter all brain tissue [183], along with increasing the slice thickness, resulting in a decreased number of slices such that the SNR in the upper slices would not be drastically affected due to an excessively high ASL signal decay [97,185]; 2) using a low-resolution multi-PLD acquisition to obtain the individual arterial transit time maps to aid the estimation of cerebral blood flow [184].

Throughout the present work, the ability to extract meaningful values in the inferior temporal lobes and anterior medial temporal lobes was limited because of proximity to air-tissue or bone-tissue interfaces, which created susceptibility artifacts. These artifacts, found only in fMRI, could be one of the potential sources of divergent findings between fMRI and PET studies [188]. Hence, the application of advanced calibrated fMRI techniques for studying conditions such as in AD, would greatly benefit from reduced susceptibility artifacts [86] considering the presence of typical regions affected by Alzheimer's disease, including the hippocampus, parahippocampus and amygdala [189-191].

In Chapter 4, when applying the QUO2 technique in elderly and AD cohorts, we observed a higher incidence of participants experiencing anxiety during the 2-min hypercapnia acclimatization compared to previous applications of the approach on healthy younger participants. Our hypercapnia acclimatization session was performed immediately prior to the imaging session, while the participant was lying down on the MRI table, positioned outside of the scanner. This decision was taken in order to allow participants to experience the effects of hypercapnia before the added stress of being inside the MRI bore. Participants who were uncomfortable with hypercapnia were excluded from the experimental protocol. The hypercapnia session being performed on the same day as the MRI session may have increased in certain participants, the stress associated with experiencing for the first time both the

hypercapnia manipulation and MRI scan within a unique visit. To lessen to a certain degree this discomfort, future calibrated studies applied in elderly or patient cohorts may consider planning a previous visit solely dedicated to the hypercapnia acclimatization session, during which the participant is comfortably seated in a room other than that of the MRI scanner.

An additional factor that reduced the statistical power of our study (Chapter 4) was the elimination of data with inadequate quality, which resulted primarily from a leak in the system circuit. This effect was either due to an imperfect fit of the mask to the participant's face, or small fissures in the valves of the gas system circuit. As time passed, the experimenters were more capable of identifying leaks prior to the imaging session, while performing the hypercapnia acclimatization, and thereby able to fix it by either re-positioning the mask, employing skin tape (Tegaderm Film, #1626W, 3M Health Care, St-Paul, MN, USA) to eliminate any remaining apertures between the skin and the mask, or replacing the defective valve. In future studies, a particular precaution should be taken with regards to training the experimenters, such that situations where a leak would weaken the data quality are detected and corrected at the beginning of the imaging session.

5.2. Additional data and future analyses

The design of the study presented in Chapter 4 included a rich array of additional data that remain to be analyzed. This section describes the supplementary material included in the acquired datasets that future studies can explore in order to deeper our knowledge about AD conditions.

In addition to the hemoglobin concentration information input to the GCM model, the blood draw administered to our cohorts of elderly and AD patients provided supplementary information on blood composition, glucose levels, amyloid precursor protein (APP) and apolipoprotein E (APOE) type. Moreover, all participants completed a neuropsychological screening, assessing, in addition to the presence of cognitive impairment (Montreal Cognitive Assessment (MoCa)), attention and executive functions (Trail making test (A and B)), episodic verbal learning (California Verbal Learning Test (CVLT)) and language disturbance (Boston Naming Test). Furthermore, all control participants were evaluated for short-term and working memory (Digit span forward and backward of WAIS-III), verbal reasoning

(Similarities subtest of the Wechsler Adult Intelligence Scale III (WAIS-III) [192], visuospatial function (Hooper Visual Organization Task) and Visual memory (Visual reproduction of Wechsler Memory Scale (WMS)). The above neuropsychological results may provide further knowledge about the nature and extent of cognitive deficits observed in our cohorts and may be combined to our imaging findings and genetic measures to assess possible correlations. Among others, one could determine if the APOE type appears to influence the patient's position on the AD spectrum estimated from the neuropsychological evaluation.

During the MRI session, a high-resolution MPRAGE anatomical scan was acquired which served to obtain the GM probability mask and to compute the non-linear transformation to the ADNI template (Chapter 4). Furthermore, in conjunction with a T_2/PD scan also acquired, it can serve to determine the volume of specific regions as well as cortical thickness, hence assessing the degree of regional atrophy in AD. Moreover, the MRI session included a fluid-attenuated inversion recovery (FLAIR) scan, which can detect white matter asymptomatic vascular lesions, and susceptibility-weighted imaging (SWI) scan, which can segment vasculature and can verify the presence of microbleeds or other vascular pathologies that may not be evident in the FLAIR images. Difference in vasculature across regions as well as vascular lesions may play a role in our findings, and should therefore be the subject to a subsequent study. Finally, a 10-min of resting-state pCASL was acquired, in order to map resting-state network (RSN) connectivity. The connectivity maps, along with the resting physiological data obtained in the QUO2 procedure, may reveal network disruption in AD dissociated from hemodynamic confounds.

In addition to the core protocol of the study, all participants were asked if they would be willing to come back for a PET FDG imaging session of 1.5 hours in order to measure the quantitative cerebral glucose metabolism in micromolar units (CMRGlu). To this date, a sub-set of 21 controls and 9 AD have undergone the PET FDG scans. After acquisition of a minimum sub-set of participants having completed both the QUO2 MRI and PET FDG protocols, one could compute the voxel-wise glycolytic index, which is the ratio of $CMRO_2$ to CMRGlu, and test hypotheses related to mitochondrial dysfunction. A higher degree of non-oxidative glucose metabolism seen in AD, i.e. presence of brain regions with lower glycolytic index, would support the hypothesis of mitochondrial dysfunction in AD. This glycolytic

index along with the evaluation of vascular and metabolic indices may reveal a spectrum of AD subtypes and serve to test hypothesis related to the primary causes of the disease. As discussed in the introduction of the present thesis, two possible chain of actions in the development of the disease may happen and be verified: a deficits in vascular function contributing to oxidative stress in neural tissues with normal oxidative function; or a mitochondrial dysfunction leading to oxidative stress despite normal vascular function.

5.3. Conclusion

The work of the present thesis first included improvements to the QUO2 acquisition protocol and analysis methods, in order to enhance the robustness and sensitivity of the quantitative approach. Then, a reproducibility assessment of the QUO2 measurements and model-derived estimates was performed, in addition to the sensitivity analysis of M, OEF and $CMRO_2$ estimates to random and systematic errors. Thereafter, an evaluation of the impact of inspired oxygen concentration on the calibrated fMRI approach was performed, before applying the enhanced QUO2 to a cohort of probable Alzheimer's disease patients. This thesis work has contributed to the enhancement of MRI quantitative approaches allowing the estimation of resting oxygen metabolism, while guiding future developments and research application of such techniques. Finally, the successful application of calibrated fMRI in Alzheimer's disease, through the identification of some key pitfalls as well as the diffusion of encouraging outcomes, highlights the potential of calibrated fMRI as an additional tool for increasing our understanding of vascular and metabolism burdens in AD.

Bibliography

1. Francis PT, Palmer AM, Snape M, K WG. The cholinergic hypothesis of Alzheimer's disease: a review of progress. Neurol Neurosurg Psychiatry. 1999 Dec. 23;66:137–147.

2. Hardy J, Allsop D. Amyloid deposition as the central event in the aetiology of Alzheimer's disease. Trends Pharmacol. Sci. 1991 Oct.;12(10):383–388.

3. Polvikoski T, Sulkava R, Haltia M, Kainulainen K, Vuorio A, Verkkoniemi A, et al. nejm199511093331902. N Engl J Med. 1995 Aug. 21;333:1242–1247.

4. Mandelkow E, Mandelkow E. Tau in Alzheimer's disease. Trends in cell biology. 1998;8:425–427.

5. Bonda DJ, Lee H-P, Lee H-G, Friedlich AL, Perry G, Zhu X, et al. Novel therapeutics for Alzheimer's disease: an update. Curr Opin Drug Discov Devel. 2010 Mar.;13(2):235–246.

6. Coskun P, Wyrembak J, Schriner SE, Chen H-W, Marciniack C, Laferla F, et al. A mitochondrial etiology of Alzheimer and Parkinson disease. Biochim Biophys Acta. 2012 May;1820(5):553–564.

7. Reddy PH, Beal MF. Are mitochondria critical in the pathogenesis of Alzheimer's disease? Brain Res Brain Res Rev. 2005 Nov.;49(3):618–632.

8. Sullivan PG, Brown MR. Mitochondrial aging and dysfunction in Alzheimer's disease. Prog Neuropsychopharmacol Biol Psychiatry. 2005 Mar.;29(3):407–410.

9. Wallace DC. A mitochondrial paradigm of metabolic and degenerative diseases, aging, and cancer: a dawn for evolutionary medicine. Annu Rev Genet. 2005 Jan.;39:359–407.

10. Aliev G, Smith MA, Obrenovich ME, la Torre de JC, Perry G. Role of vascular hypoperfusion-induced oxidative stress and mitochondria failure in the pathogenesis of Alzheimer disease. Neurotox Res. 2003 Jan.;5(7):491–504.

11. Frackowiak RS, Lenzi GL, Jones T, Heather JD. Quantitative measurement of regional cerebral blood flow and oxygen metabolism in man using 15O and positron emission tomography: theory, procedure, and normal values. J Comput Assist Tomogr. 1980 Dec.;4(6):727–736.

12. Mintun MA, Raichle ME, Martin WR, Herscovitch P. Brain oxygen utilization measured with O-15 radiotracers and positron emission tomography. J Nucl Med. 1984 Feb.;25(2):177–187.

13. Ohta S, Reutens D, Gjedde A. Brief vibrotactile stimulation does not increase cortical oxygen consumption when measured by single inhalation of positron emitting oxygen. Journal of Cerebral Blood …. 1999;19:260–265.

14. Ishii K, Kitagaki H, Kono M, Mori E. Decreased medial temporal oxygen metabolism in Alzheimer's disease shown by PET. J Nucl Med. 1996 Jul.;37(7):1159–1165.

15. Nagata K, Maruya H, Yuya H, Terashi H, Mito Y, Kato H, et al. Can PET data differentiate Alzheimer's disease from vascular dementia? Ann N Y Acad Sci. 2000 Apr.;903:252–261.

16. Tohgi H, Yonezawa H, Takahashi S, Sato N, Kato E, Kudo M, et al. Cerebral blood flow and oxygen metabolism in senile dementia of Alzheimer's type and vascular dementia with deep white matter changes. Neuroradiology. 1998 Mar.;40(3):131–137.

17. Fukuyama H, Ogawa M, Yamauchi H, Yamaguchi S, Kimura J, Yonekura Y, et al. Altered cerebral energy metabolism in Alzheimer's disease: a PET study. J Nucl Med. 1994 Jan.;35(1):1–6.

18. Mintun MA, Vlassenko AG, Shulman GL, Snyder AZ. Time-related increase of oxygen utilization in continuously activated human visual cortex. NeuroImage. 2002 Jun.;16(2):531–537.

19. Yamauchi H, Okazawa H, Kishibe Y, Sugimoto K, Takahashi M. Changes in Blood Flow and Oxygen Metabolism During Visual Stimulation in Carotid Artery Disease: Effect of Baseline Perfusion and Oxygen Metabolism. Stroke. 2002 May 1;33(5):1294–1300.

20. Hattori N, Bergsneider M, Wu H-M, Glenn TC, Vespa PM, Hovda DA, et al. Accuracy of a method using short inhalation of (15)O-O(2) for measuring cerebral oxygen extraction fraction with PET in healthy humans. J Nucl Med. 2004 May;45(5):765–770.

21. Ito H, Ibaraki M, Kanno I, Fukuda H, Miura S. Changes in cerebral blood flow and cerebral oxygen metabolism during neural activation measured by positron emission

tomography: comparison with blood oxygenation level-dependent contrast measured by functional magnetic resonance imaging. J Cereb Blood Flow Metab. 2005 Jan. 19;25(3):371–377.

22. Ibaraki M, Miura S, Shimosegawa E, Sugawara S, Mizuta T, Ishikawa A, et al. Quantification of cerebral blood flow and oxygen metabolism with 3-dimensional PET and 15O: validation by comparison with 2-dimensional PET. J Nucl Med. 2008 Jan.;49(1):50–59.

23. Ibaraki M, Shinohara Y, Nakamura K, Miura S, Kinoshita F, Kinoshita T. Interindividual variations of cerebral blood flow, oxygen delivery, and metabolism in relation to hemoglobin concentration measured by positron emission tomography in humans. J Cereb Blood Flow Metab. Nature Publishing Group; 2010 Feb. 17;30(7):1296–1305.

24. Herholz K, Carter SF, Jones M. Positron emission tomography imaging in dementia. British Journal of Radiology. 2007 Dec. 1;80(Special Issue 2):S160–S167.

25. Foster NL, Heidebrink JL, Clark CM, Jagust WJ, Arnold SE, Barbas NR, et al. FDG-PET improves accuracy in distinguishing frontotemporal dementia and Alzheimer's disease. Brain. 2007 Oct. 1;130(10):2616–2635.

26. Fox NC, Scahill RI, Crum WR, Rossor MN. Correlation between rates of brain atrophy and cognitive decline in AD. Neurology. 1999 May 12;52(8):1687–1689.

27. Josephs KA, Whitwell JL, Ahmed Z, Shiung MM, Weigand SD, Knopman DS, et al. β-amyloid burden is not associated with rates of brain atrophy. Ann Neurol. 2008 Feb.;63(2):204–212.

28. Schott JM, Crutch SJ, Frost C, Warrington EK, Rossor MN, Fox NC. Neuropsychological correlates of whole brain atrophy in Alzheimer's disease. Neuropsychologia. 2008 May;46(6):1732–1737.

29. Sluimer JD, Bouwman FH, Vrenken H, Blankenstein MA, Barkhof F, van der Flier WM, et al. Whole-brain atrophy rate and CSF biomarker levels in MCI and AD: A longitudinal study. NBA. Elsevier Inc.; 2010 May 1;31(5):758–764.

30. Thompson PM, Hayashi KM, de Zubicaray GI, Janke AL, Rose SE, Semple J, et al. Mapping hippocampal and ventricular change in Alzheimer disease. NeuroImage. 2004 Aug.;22(4):1754–1766.

31. Jack CR, Shiung MM, Gunter JL, O'Brien PC, Weigand SD, Knopman DS, et al. Comparison of different MRI brain atrophy rate measures with clinical disease progression in AD. Neurology. 2004 Feb. 24;62(4):591–600.

32. Morra JH, Tu Z, Apostolova LG, Green AE, Avedissian C, Madsen SK, et al. Automated 3D mapping of hippocampal atrophy and its clinical correlates in 400 subjects with Alzheimer's disease, mild cognitive impairment, and elderly controls. Hum. Brain Mapp. 2009 Sep. 15;30(9):2766–2788.

33. Ridha BH, Anderson VM, Barnes J, Boyes RG, Price SL, Rossor MN, et al. Volumetric MRI and cognitive measures in Alzheimer disease. J Neurol. 2008 Feb. 18;255(4):567–574.

34. Cardenas VA, Chao LL, Studholme C, Yaffe K, Miller BL, Madison C, et al. Brain atrophy associated with baseline and longitudinal measures of cognition. NBA. Elsevier Inc.; 2011 Apr. 1;32(4):572–580.

35. Brambati SM, Belleville S, Kergoat M-J, Chayer C, Gauthier S, Joubert S. Single- and Multiple-Domain Amnestic Mild Cognitive Impairment: Two Sides of the Same Coin? Dement Geriatr Cogn Disord. 2009;28(6):541–549.

36. Vernooij MW, Smits M. Structural neuroimaging in aging and Alzheimer's disease. Neuroimaging Clin. N. Am. 2012 Feb.;22(1):33–55, vii–viii.

37. Jack CR, Lowe VJ, Weigand SD, Wiste HJ, Senjem ML, Knopman DS, et al. Serial PIB and MRI in normal, mild cognitive impairment and Alzheimer“s disease: implications for sequence of pathological events in Alzheimer”s disease. Brain. 2009 May 6;132(5):1355–1365.

38. Kim S-G, Ogawa S. Biophysical and physiological origins of blood oxygenation level-dependent fMRI signals. Nature Publishing Group; 2012 Mar. 7;32(7):1188–1206.

39. Ogawa S, Lee TM, Kay AR, Tank DW. Brain magnetic resonance imaging with contrast dependent on blood oxygenation. Proc Natl Acad Sci USA. 1990 Dec.;87(24):9868–9872.

40. Ogawa S, Lee TM, Nayak AS, Glynn P. Oxygenation-sensitive contrast in magnetic resonance image of rodent brain at high magnetic fields. Magn. Reson. Med. 1990 Apr.;14(1):68–78.

41. Kim SG, Fukuda M. Lessons from fMRI about Mapping Cortical Columns. The Neuroscientist. 2007 Nov. 7;14(3):287–299.

42. Atri A, O'Brien JL, Sreenivasan A, Rastegar S, Salisbury S, DeLuca AN, et al. Test-retest reliability of memory task functional magnetic resonance imaging in Alzheimer disease clinical trials. Archives of Neurology. 2011 May;68(5):599–606.

43. Belleville S, Clement F, Mellah S, Gilbert B, Fontaine F, Gauthier S. Training-related brain plasticity in subjects at risk of developing Alzheimer's disease. Brain. 2011 May 26;134(6):1623–1634.

44. Miettinen PS, Pihlajamäki M, Jauhiainen AM, Niskanen E, Hänninen T, Vanninen R, et al. Structure and function of medial temporal and posteromedial cortices in early Alzheimer’s disease. European Journal of Neuroscience. 2011 Jun. 21;34(2):320–330.

45. Greicius MD, Krasnow B, Reiss AL, Menon V. Functional connectivity in the resting brain: a network analysis of the default mode hypothesis. Proc. Natl. Acad. Sci. U.S.A. 2003 Jan. 7;100(1):253–258.

46. Greicius MD, Srivastava G, Reiss AL, Menon V. Default-mode network activity distinguishes Alzheimer's disease from healthy aging: evidence from functional MRI. Proc. Natl. Acad. Sci. U.S.A. 2004 Mar. 30;101(13):4637–4642.

47. Gusnard DA, Raichle ME, Raichle ME. Searching for a baseline: functional imaging and the resting human brain. Nat Rev Neurosci. 2001 Oct.;2(10):685–694.

48. LASSEN NA. Cerebral blood flow and oxygen consumption in man. Physiol Rev. 1959 Apr.;39(2):183–238.

49. Ito H, Kanno I, Ibaraki M, Hatazawa J, Miura S. Changes in human cerebral blood flow and cerebral blood volume during hypercapnia and hypocapnia measured by positron emission tomography. Journal of Cerebral Blood Flow & Metabolism. 2003 Jun.;23(6):665–670.

50. Kety SS, Schmidt CF. The effects of altered arterial tensions of carbon dioxide and oxygen on cerebral blood flow and cerebral oxygen consumption of normal young men. J. Clin. Invest. 1948 Jul.;27(4):484–492.

51. Binnewijzend MAA, Kuijer JPA, Benedictus MR, van der Flier WM, Wink AM, Wattjes MP, et al. Cerebral Blood Flow Measured with 3D Pseudocontinuous Arterial Spin-labeling MR Imaging in Alzheimer Disease and Mild Cognitive Impairment: A Marker for Disease Severity. Radiology. 2013 Apr.;267(1):221–230.

52. Alsop DC, Dai W, Grossman M, Detre JA. Arterial spin labeling blood flow MRI: its role in the early characterization of Alzheimer's disease. J Alzheimers Dis. 2010;20(3):871–880.

53. Alsop DC, Casement M, de Bazelaire C, Fong T, Press DZ. Hippocampal hyperperfusion in Alzheimer's disease. NeuroImage. 2008 Oct.;42(4):1267–1274.

54. Dai W, Lopez OL, Carmichael OT, Becker JT, Kuller LH, Gach HM. Mild Cognitive Impairment and Alzheimer Disease: Patterns of Altered Cerebral Blood Flow at MR Imaging. Radiology. 2009 Jan. 21;250(3):856–866.

55. Davis TL, Kwong KK, Weisskoff RM, Rosen BR. Calibrated functional MRI: mapping the dynamics of oxidative metabolism. Proc. Natl. Acad. Sci. U.S.A. 1998 Feb. 17;95(4):1834–1839.

56. Chiarelli PA, Bulte DP, Wise R, Gallichan D, Jezzard P. A calibration method for quantitative BOLD fMRI based on hyperoxia. NeuroImage. 2007 Sep.;37(3):808–820.

57. Yasaka M, Read SJ, O'Keefe GJ, Egan GF, Pointon O, McKay WJ, et al. Positron emission tomography in ischaemic stroke: cerebral perfusion and metabolism after stroke onset. J Clin Neurosci. 1998 Oct.;5(4):413–416.

58. Blockley NP, Griffeth VEM, Buxton RB. A general analysis of calibrated BOLD methodology for measuring CMRO2 responses: Comparison of a new approach with existing methods. NeuroImage. Elsevier Inc.; 2012 Mar. 1;60(1):279–289.

59. Gauthier CJ, Hoge RD. A generalized procedure for calibrated MRI incorporating hyperoxia and hypercapnia. Hum. Brain Mapp. 2012 Jan. 16;34(5):1053–1069.

60. An H, Lin W. Quantitative measurements of cerebral blood oxygen saturation using magnetic resonance imaging. J Cereb Blood Flow Metab. 2000 Aug.;20(8):1225–1236.

61. He X, Yablonskiy DA. Quantitative BOLD: Mapping of human cerebral deoxygenated blood volume and oxygen extraction fraction: Default state. Magn. Reson. Med. 2006;57(1):115–126.

62. He X, Zhu M, Yablonskiy DA. Validation of oxygen extraction fraction measurement by qBOLD technique. Magn. Reson. Med. 2008 Oct.;60(4):882–888.

63. Bolar DS, Rosen BR, Sorensen AG, Adalsteinsson E. QUantitative Imaging of eXtraction of oxygen and TIssue consumption (QUIXOTIC) using venular-targeted velocity-selective spin labeling. Magn. Reson. Med. 2011 Jun. 14;66(6):1550–1562.

64. Bulte DP, Kelly M, Germuska M, Xie J, Chappell MA, Okell TW, et al. Quantitative measurement of cerebral physiology using respiratory-calibrated MRI. NeuroImage. Elsevier Inc.; 2012 Mar. 1;60(1):582–591.

65. Gauthier CJ, Hoge RD. Magnetic resonance imaging of resting OEF and CMRO2 using a generalized calibration model for hypercapnia and hyperoxia. NeuroImage. 2011;60:1212–1225.

66. Tancredi FB, Lajoie I, Hoge RD. A simple breathing circuit allowing precise control of inspiratory gases for experimental respiratory manipulations. BMC Res Notes. 2014 Apr. 12;7:235.

67. Tancredi FB, Lajoie I, Hoge RD. Test-retest reliability of cerebral blood flow and blood oxygenation level-dependent responses to hypercapnia and hyperoxia using dual-echo pseudo-continuous arterial spin labeling and step changes in the fractional composition of inspired gases. J. Magn. Reson. Imaging. 2015 Mar. 6;42(4):1144–1157.

68. Grubb RL, Raichle ME, Eichling JO, Ter-Pogossian MM. The effects of changes in PaCO2 on cerebral blood volume, blood flow, and vascular mean transit time. Stroke. 1974 Aug.;5(5):630–639.

69. Chen JJ, Pike GB. BOLD-specific cerebral blood volume and blood flow changes during neuronal activation in humans. NMR Biomed. 2009;22:1054–1062.

70. Chen JJ, Pike GB. MRI measurement of the BOLD-specific flow–volume relationship during hypercapnia and hypocapnia in humans. NeuroImage. Elsevier Inc.; 2010 Nov. 1;53(2):383–391.

71. Boxerman JL, Hamberg LM, Rosen BR, Weisskoff RM. MR contrast due to intravascular magnetic susceptibility perturbations. Magn. Reson. Med. 1995;34(4):555–566.

72. Griffeth VEM, Buxton RB. A theoretical framework for estimating cerebral oxygen metabolism changes using the calibrated-BOLD method: Modeling the effects of blood volume distribution, hematocrit, oxygen extraction fraction, and tissue signal properties on the BOLD signal. NeuroImage. Elsevier Inc.; 2011 Jun. 28;:1–15.

73. Rhoades R, Bell D. Medical phisiology: Principles for clinical medicine. 2012.

74. Murphy WG. The sex difference in haemoglobin levels in adults - mechanisms, causes, and consequences. Blood Rev. 2014 Mar.;28(2):41–47.

75. Shapleigh JB, Mayes S, Moore CV. Hematologic Values in the Aged. Journal of Gerontology. 1952 Apr. 1;7(2):207–219.

76. Smith JS, Whitelaw DM. Hemoglobin values in aged men. Can Med Assoc J. 1971 Oct. 23;105(8):816–8 passim.

77. Chen JJ, Pike GB. Global cerebral oxidative metabolism during hypercapnia and hypocapnia in humans: implications for BOLD fMRI. J Cereb Blood Flow Metab. Nature Publishing Group; 2010 Apr. 7;30:1094–1999.

78. Hino JK, Short BL, Rais-Bahrami K, Seale WR. Cerebral blood flow and metabolism during and after prolonged hypercapnia in newborn lambs. Crit Care Med. 2000 Oct.;28:3505–3510.

79. McPherson RW, Derrer SA, Traystman RJ. Changes in cerebral CO2 responsivity over time during isoflurane anesthesia in the dog. J Neurosurg Anesthesiol. 1991 Mar.;3:12–19.

80. Horvath I, Sandor NT, Ruttner Z, McLaughlin AC. Role of nitric oxide in regulating cerebrocortical oxygen consumption and blood flow during hypercapnia. J Cereb Blood Flow Metab. 1994 May;14:503–509.

81. Zappe AC, Uludağ K, Logothetis NK. Direct measurement of oxygen extraction with fMRI using 6% CO2 inhalation. Magnetic Resonance Imaging. 2008 Sep.;26(7):961–967.

82. Xu F, Uh J, Brier MR, Hart J, Yezhuvath US, Gu H, et al. The influence of carbon dioxide on brain activity and metabolism in conscious humans. J Cereb Blood Flow Metab. Nature Publishing Group; 2010 Sep. 15;31:58–67.

83. Xu F, Liu P, Pascual JM, Xiao G, Lu H. Effect of hypoxia and hyperoxia on cerebral blood flow, blood oxygenation, and oxidative metabolism. J Cereb Blood Flow Metab. 2012 Oct.;32(10):1909–1918.

84. Bulte DP, Chiarelli PA, Wise RG, Jezzard P. Cerebral perfusion response to hyperoxia. J Cereb Blood Flow Metab. 2006 May 3;27(1):69–75.

85. Gauthier CJ, Desjardins-Crépeau L, Madjar C, Bherer L, Hoge RD. Absolute quantification of resting oxygen metabolism and metabolic reactivity during functional activation using QUO2 MRI. NeuroImage. Elsevier Inc.; 2012 Nov. 15;63(3):1353–1363.

86. Pilkinton DT, Gaddam SR, Reddy R. Characterization of paramagnetic effects of molecular oxygen on blood oxygenation level-dependent-modulated hyperoxic contrast studies of the human brain. Magn. Reson. Med. 2011 May 23;66(3):794–801.

87. Tadamura E, Hatabu H, Li W, Prasad PV, Edelman RR. Effect of oxygen inhalation on relaxation times in various tissues. J. Magn. Reson. Imaging. 1997;7(1):220–225.

88. Noseworthy MD, Kim JK, Stainsby JA, Stanisz GJ, Wright GA. Tracking oxygen effects on MR signal in blood and skeletal muscle during hyperoxia exposure. J. Magn. Reson. Imaging. 1999 Jun.;9(6):814–820.

89. Pilkinton DT, Hiraki T, Detre JA, Greenberg JH, Reddy R. Absolute cerebral blood flow quantification with pulsed arterial spin labeling during hyperoxia corrected with the

simultaneous measurement of the longitudinal relaxation time of arterial blood. Magn. Reson. Med. 2011 Aug. 29;67(6):1556–1565.

90. Buxton RB, Frank LR, Wong EC, Siewert B, Warach S, Edelman RR. A general kinetic model for quantitative perfusion imaging with arterial spin labeling. Magn. Reson. Med. 1998 Sep.;40(3):383–396.

91. Chalela JA, Alsop DC, Gonzalez-Atavales JB, Maldjian JA, Kasner SE, Detre JA. Magnetic Resonance Perfusion Imaging in Acute Ischemic Stroke Using Continuous Arterial Spin Labeling. Stroke. 2000 Mar. 1;31(3):680–687.

92. Zaharchuk G, Martin AJ, Dillon WP. Noninvasive Imaging of Quantitative Cerebral Blood Flow Changes during 100% Oxygen Inhalation Using Arterial Spin-Labeling MR Imaging. American Journal of Neuroradiology. 2008 Apr. 1;29(4):663–667.

93. Wang J, Alsop DC, Song HK, Maldjian JA, Tang K, Salvucci AE, et al. Arterial transit time imaging with flow encoding arterial spin tagging (FEAST). Magn. Reson. Med. 2003 Aug. 20;50(3):599–607.

94. Gauthier CJ, Madjar C, Desjardins-Crépeau L, Bellec P, Bherer L, Hoge RD. Age dependence of hemodynamic response characteristics in human functional magnetic resonance imaging. Neurobiology of Aging. 2013 May;34(5):1469–1485.

95. Mohtasib RS, Lumley G, Goodwin JA, Emsley HCA, Sluming V, Parkes LM. Calibrated fMRI during a cognitive Stroop task reveals reduced metabolic response with increasing age. NeuroImage. 2012 Jan.;59(2):1143–1151.

96. Ances BM, Liang CL, Leontiev O, Perthen JE, Fleisher AS, Lansing AE, et al. Effects of aging on cerebral blood flow, oxygen metabolism, and blood oxygenation level dependent responses to visual stimulation. Hum. Brain Mapp. 2009 Apr.;30(4):1120–1132.

97. De Vis JB, Hendrikse J, Bhogal A, Adams A, Kappelle LJ, Petersen ET. Age-related changes in brain hemodynamics; A calibrated MRI study. Hum. Brain Mapp. 2015 Jul. 14;36(10):3973–3987.

98. De Vis JB, Petersen ET, Bhogal A, Hartkamp NS, Klijn CJ, Kappelle LJ, et al. Calibrated MRI to evaluate cerebral hemodynamics in patients with an internal carotid artery

occlusion. J Cereb Blood Flow Metab. Nature Publishing Group; 2015 Feb. 25;35(6):1015–1023.

99. Yamaguchi T, Kanno I, Uemura K, Shishido F, Inugami A, Ogawa T, et al. Reduction in regional cerebral metabolic rate of oxygen during human aging. Stroke. 1986 Oct.;17(6):1220–1228.

100. Leenders KL, Perani D, Lammertsma AA, Heather JD. Cerebral blood flow, blood volume and oxygen utilization. Brain. 1990 Jun. 25;113:27–47.

101. Lu H, Xu F, Rodrigue KM, Kennedy KM, Cheng Y, Flicker B, et al. Alterations in Cerebral Metabolic Rate and Blood Supply across the Adult Lifespan. Cerebral Cortex. 2011 May 19;21(6):1426–1434.

102. Lu H, Ge Y. Quantitative evaluation of oxygenation in venous vessels using T2-Relaxation-Under-Spin-Tagging MRI. Magn. Reson. Med. 2008 Aug.;60(2):357–363.

103. Xu F, Ge Y, Lu H. Noninvasive quantification of whole-brain cerebral metabolic rate of oxygen (CMRO2) by MRI. Magn. Reson. Med. 2009 Apr.;62:141–148.

104. Jain V, Langham MC, Wehrli FW. MRI estimation of global brain oxygen consumption rate. J Cereb Blood Flow Metab. Nature Publishing Group; 2010 Apr. 21;30(9):1598–1607.

105. Fan AP, Benner T, Bolar DS, Rosen BR, Adalsteinsson E. Phase-based regional oxygen metabolism (PROM) using MRI. Magn. Reson. Med. 2011 Jun. 28;67(3):669–678.

106. Wise RG, Harris AD, Stone AJ, Murphy K. Measurement of OEF and absolute CMRO2: MRI-based methods using interleaved and combined hypercapnia and hyperoxia. NeuroImage. 2013 Dec.;83:135–147.

107. Parkes LM, Rashid W, Chard DT, Tofts PS. Normal cerebral perfusion measurements using arterial spin labeling: Reproducibility, stability, and age and gender effects. Magn. Reson. Med. 2004;51(4):736–743.

108. Dai W, Garcia D, de Bazelaire C, Alsop DC. Continuous flow-driven inversion for arterial spin labeling using pulsed radio frequency and gradient fields. Magn. Reson. Med. 2008 Dec.;60(6):1488–1497.

109. Severinghaus JW. Water vapor calibration errors in some capnometers: respiratory conventions misunderstood by manufacturers? Anesthesiology. 1989 Jun.;70(6):996–998.

110. Tancredi FB, Hoge RD. Comparison of cerebral vascular reactivity measures obtained using breath-holding and CO2 inhalation. Journal of Cerebral Blood Flow & Metabolism. 2013 Jul.;33(7):1066–1074.

111. Poulin MJ, Liang PJ, Robbins PA. Dynamics of the cerebral blood flow response to step changes in end-tidal PCO~and PO, in humans. J Appl Physiol. 1996 Jul. 13;81:1084–1095.

112. Alsop DC, Detre JA, Golay X, Günther M, Hendrikse J, Hernandez-Garcia L, et al. Recommended implementation of arterial spin-labeled perfusion MRI for clinical applications: A consensus of the ISMRM perfusion study group and the European consortium for ASL in dementia. Magn. Reson. Med. 2015 Jan.;73(1):102–116.

113. Jenkinson M, Smith S. A global optimisation method for robust affine registration of brain images. Med Image Anal. 2001 Jan. 8;5:143–156.

114. Klein A, Tourville J. 101 labeled brain images and a consistent human cortical labeling protocol. Front Neurosci. 2012;6:171.

115. Alsop DC, Detre JA, Grossman M. Assessment of cerebral blood flow in Alzheimer's disease by spin-labeled magnetic resonance imaging. Ann Neurol. 2000 Jan.;47(1):93–100.

116. Johnson NA, Jahng G-H, Weiner MW, Miller BL, Chui HC, Jagust WJ, et al. Pattern of Cerebral Hypoperfusion in Alzheimer Disease and Mild Cognitive Impairment Measured with Arterial Spin-labeling MR Imaging: Initial Experience1. Radiology. 2005 Mar.;234(3):851–859.

117. Du AT, Jahng GH, Hayasaka S, Kramer JH, Rosen HJ, Gorno-Tempini ML, et al. Hypoperfusion in frontotemporal dementia and Alzheimer disease by arterial spin labeling MRI. Neurology. 2006 Oct.;67(7):1215–1220.

118. Asllani I, Habeck C, Scarmeas N, Borogovac A, Brown TR, Stern Y. Multivariate and univariate analysis of continuous arterial spin labeling perfusion MRI in Alzheimer's disease. J Cereb Blood Flow Metab. 2007 Oct. 24;28(4):725–736.

119. Yao J, Rettberg JR, Klosinski LP, Cadenas E, Brinton RD. Shift in brain metabolism in late onset Alzheimer's disease: Implications for biomarkers and therapeutic interventions. Mol Aspects Med. 2011 Aug.;32(4-6):247–257.

120. Collins DL, Holmes CJ, Peters TM, Evans AC. Automatic 3-D Model-Based Neuroanatomical Segmentation. Hum. Brain Mapp. 1995 Sep. 12;3:190–208.

121. Sherif T, Rioux P, Rousseau M-E, Kassis N, Beck N, Adalat R, et al. CBRAIN: a web-based, distributed computing platform for collaborative neuroimaging research. Front Neuroinform. 2014;8:54.

122. Padhani AR, Hayes C, Landau S, Leach MO. Reproducibility of quantitative dynamic MRI of normal human tissues. NMR Biomed. 2002;15(2):143–153.

123. Floyd TF, Ratcliffe SJ, Wang J, Resch B, Detre JA. Precision of the CASL-perfusion MRI technique for the measurement of cerebral blood flow in whole brain and vascular territories. J. Magn. Reson. Imaging. 2003 Nov. 18;18(6):649–655.

124. Jain V, Duda J, Avants B, Giannetta M, Xie SX, Roberts T, et al. Longitudinal reproducibility and accuracy of pseudo-continuous arterial spin-labeled perfusion MR imaging in typically developing children. Radiology. 2012 May;263(2):527–536.

125. Chen Y, Wang DJJ, Detre JA. Test-retest reliability of arterial spin labeling with common labeling strategies. J. Magn. Reson. Imaging. 2011 Mar. 29;33(4):940–949.

126. Bland JM, Altman DG. Measurement error proportional to the mean. BMJ. 1996 Jul. 13;313(7049):106.

127. Bland JM, Altman DG. Statistical methods for assessing agreement between two methods of clinical measurement. Lancet. 1986 Feb. 8;1(8476):307–310.

128. Tjandra T, Brooks JCW, Figueiredo P, Wise R, Matthews PM, Tracey I. Quantitative assessment of the reproducibility of functional activation measured with BOLD and MR perfusion imaging: Implications for clinical trial design. NeuroImage. 2005 Aug.;27(2):393–401.

129. Mark CI, Fisher JA, Pike GB. Improved fMRI calibration: Precisely controlled hyperoxic versus hypercapnic stimuli. NeuroImage. Elsevier Inc.; 2011 Jan. 15;54:1102–1111.

130. Gustard S, Williams EJ, Hall LD, Pickard JD, Carpenter TA. Influence of baseline hematocrit on between-subject BOLD signal change using gradient echo and asymmetric spin echo EPI. Magnetic Resonance Imaging. 2003 Jul.;21(6):599–607.

131. Merola A, Murphy K, Stone AJ, Germuska MA, Griffeth VEM, Blockley NP, et al. Measurement of oxygen extraction fraction (OEF): An optimized BOLD signal model for use with hypercapnic and hyperoxic calibration. NeuroImage. The Authors; 2016 Apr. 1;129:159–174.

132. Bulte DP, Drescher K, Jezzard P. Comparison of hypercapnia-based calibration techniques for measurement of cerebral oxygen metabolism with MRI. Magn. Reson. Med. 2009 Feb.;61(2):391–398.

133. Ances BM, Leontiev O, Perthen JE, Liang C, Lansing AE, Buxton RB. Regional differences in the coupling of cerebral blood flow and oxygen metabolism changes in response to activation: Implications for BOLD-fMRI. NeuroImage. 2008 Feb.;39(4):1510–1521.

134. Chen Y, Parrish TB. Caffeine's effects on cerebrovascular reactivity and coupling between cerebral blood flow and oxygen metabolism. NeuroImage. Elsevier Inc.; 2009 Feb. 1;44(3):647–652.

135. Gauthier CJ, Madjar C, Tancredi FB, Stefanovic B, Hoge RD. Elimination of visually evoked BOLD responses during carbogen inhalation: Implications for calibrated MRI. NeuroImage. Elsevier Inc.; 2011 Jan. 15;54:1001–1011.

136. Lin A-L, Fox PT, Yang Y, Lu H, Tan L-H, Gao J-H. Evaluation of MRI models in the measurement of CMRO 2and its relationship with CBF. Magn. Reson. Med. 2008 Aug.;60(2):380–389.

137. Leontiev O, Buxton RB. Reproducibility of BOLD, perfusion, and CMRO2 measurements with calibrated-BOLD fMRI. NeuroImage. 2007 Jan.;35:175–184.

138. Perthen JE, Lansing AE, Liau J, Liu TT, Buxton RB. Caffeine-induced uncoupling of cerebral blood flow and oxygen metabolism: a calibrated BOLD fMRI study. NeuroImage. 2008 Mar.;40(1):237–247.

139. van Zijl PCM, Eleff SM, Ulatowski JA, Oja JME, Ulug AM, Traystman RJ, et al. Quantitative assessment of blood flow, blood volume and blood oxygenation effects in functional magnetic resonance imaging. Nat. Med. 1998 Jun. 26;4:159–167.

140. Coles JP, Fryer TD, Bradley PG, Nortje J, Smielewski P, Rice K, et al. Intersubject variability and reproducibility of 15O PET studies. J Cereb Blood Flow Metab. 2006 Jan.;26(1):48–57.

141. Bremmer JP, van Berckel BNM, Persoon S, Kappelle LJ, Lammertsma AA, Kloet R, et al. Day-to-day test-retest variability of CBF, CMRO2, and OEF measurements using dynamic 15O PET studies. Mol Imaging Biol. 2011 Aug.;13(4):759–768.

142. Ito H, Kanno I, Kato C, Sasaki T, Ishii K, Ouchi Y, et al. Database of normal human cerebral blood flow, cerebral blood volume, cerebral oxygen extraction fraction and cerebral metabolic rate of oxygen measured by positron emission tomography with 15 O-labelled carbon dioxide or water, carbon monoxide and oxygen: a multicentre study in Japan. Eur J Nucl Med Mol Imaging. 2004 May 1;31(5):635–643.

143. Krieger SN, Gauthier CJ, Ivanov D, Huber L, Roggenhofer E, Sehm B, et al. Regional reproducibility of calibrated BOLD functional MRI: Implications for the study of cognition and plasticity. NeuroImage. 2014 Nov.;101:8–20.

144. Wang Y, Saykin AJ, Pfeuffer J, Lin C, Mosier KM, Shen L, et al. Regional reproducibility of pulsed arterial spin labeling perfusion imaging at 3T. NeuroImage. Elsevier Inc.; 2011 Jan. 15;54(2):1188–1195.

145. Siero JCW, Strother MK, Faraco CC, Hoogduin H, Hendrikse J, Donahue MJ. In vivoquantification of hyperoxic arterial blood water T1. NMR Biomed. 2015 Sep. 30;28(11):1518–1525.

146. Glover GH, Li TQ, Ress D. Image-based method for retrospective correction of physiological motion effects in fMRI: RETROICOR. Magn. Reson. Med. 2000 Jul.;44(1):162–167.

147. Wen-Chau Wu, Edlow BL, Elliot MA, Jiongjiong Wang, Detre JA. Physiological Modulations in Arterial Spin Labeling Perfusion Magnetic Resonance Imaging. IEEE Trans. Med. Imaging. 2009 Jul. 13;28(5):703–709.

148. Zhang W, Silva AC, Williams DS, Koretsky AP. Measurement of Perfusion Using Arterial Spin Labeling Without Saturation. Magn. Reson. Med. 1995 Jun. 23;33:370–376.

149. MacIntosh BJ, Filippini N, Chappell MA, Woolrich MW, Mackay CE, Jezzard P. Assessment of arterial arrival times derived from multiple inversion time pulsed arterial spin labeling MRI. Magn. Reson. Med. 2010 Mar.;63(3):641–647.

150. Gallichan D, Jezzard P. Variation in the shape of pulsed arterial spin labeling kinetic curves across the healthy human brain and its implications for CBF quantification. Magn. Reson. Med. 2009 Mar.;61(3):686–695.

151. Donahue MJ, Faraco CC, Strother MK, Chappell MA, Rane S, Dethrage LM, et al. Bolus arrival time and cerebral blood flow responses to hypercarbia. J Cereb Blood Flow Metab. 2014 Apr. 30;34(7):1243–1252.

152. Aslan S, Xu F, Wang PL, Uh J, Yezhuvath US, van Osch M, et al. Estimation of labeling efficiency in pseudocontinuous arterial spin labeling. Magn. Reson. Med. 2010 Mar.;63(3):765–771.

153. Jahanian H, Noll DC, Hernandez-Garcia L. B0 field inhomogeneity considerations in pseudo-continuous arterial spin labeling (pCASL): effects on tagging efficiency and correction strategy. NMR Biomed. 2011 Mar. 8;24:1202–1209.

154. Asllani I, Borogovac A, Brown TR. Regression algorithm correcting for partial volume effects in arterial spin labeling MRI. Magn. Reson. Med. 2008 Dec.;60:1362–1371.

155. Blockley NP, Driver ID, Francis ST, Fisher JA, Gowland PA. An improved method for acquiring cerebrovascular reactivity maps. Magn. Reson. Med. 2010 Dec. 8;65:1278–1286.

156. Günther M, Oshio K, Feinberg DA. Single-shot 3D imaging techniques improve arterial spin labeling perfusion measurements. Magn. Reson. Med. 2005;54:491–498.

157. Feinberg DA, Setsompop K. Ultra-fast MRI of the human brain with simultaneous multi-slice imaging. Journal of Magnetic Resonance. 2013 Apr.;229:90–100.

158. Ye FQ, Frank JA, Weinberger DR, McLaughlin AC. Noise Reduction in 3D Perfusion Imaging by Attenuating the Static Signal in Arterial Spin Tagging (ASSIST). Magn. Reson. Med. 2000 May 23;44:92–100.

159. Garcia DM, Duhamel G, Alsop DC. Efficiency of inversion pulses for background suppressed arterial spin labeling. Magn. Reson. Med. 2005;54:366–372.

160. Ghariq E, Chappell MA, Schmid S, Teeuwisse WM, van Osch MJP. Effects of background suppression on the sensitivity of dual-echo arterial spin labeling MRI for BOLD and CBF signal changes. NeuroImage. 2014 Dec.;103:316–322.

161. Brannan S, Liotti M, Egan G, Shade R, Madden L, Robillard R, et al. Neuroimaging of cerebral activations and deactivations associated with hypercapnia and hunger for air. Proc. Natl. Acad. Sci. U.S.A. 2001 Feb. 13;98(4):2029–2034.

162. Liotti M, Brannan S, Egan G, Shade R, Madden L, Abplanalp B, et al. Brain responses associated with consciousness of breathlessness (air hunger). Proc. Natl. Acad. Sci. U.S.A. 2001 Feb. 13;98(4):2035–2040.

163. Lajoie I, Tancredi FB, Hoge RD. Regional Reproducibility of BOLD Calibration Parameter M, OEF and Resting-State CMRO2 Measurements with QUO2 MRI. PLoS ONE. 2016;11(9):e0163071.

164. Iscoe S, Fisher JA. Hyperoxia-induced hypocapnia: an underappreciated risk. Chest. 2005 Jul.;128(1):430–433.

165. Goodwin JA, Vidyasagar R, Balanos GM, Bulte D, Parkes LM. Quantitative fMRI using hyperoxia calibration: Reproducibility during a cognitive Stroop task. NeuroImage. Elsevier Inc.; 2009 Aug. 15;47(2):573–580.

166. Lu H, Clingman C, Golay X, van Zijl PCM. Determining the longitudinal relaxation time (T1) of blood at 3.0 Tesla. Magn. Reson. Med. 2004;52(3):679–682.

167. Benga G, Borza T. Diffusional water permeability of mammalian red blood cells. Comp. Biochem. Physiol. B, Biochem. Mol. Biol. 1995 Dec.;112(4):653–659.

168. Lin A-L, Qin Q, Zhao X, Duong TQ. Blood longitudinal (T 1) and transverse (T 2) relaxation time constants at 11.7 Tesla. Magn Reson Mater Phy. 2011 Nov. 10;25(3):245–249.

169. Kivipelto M, Helkala EL, Laakso MP, Hänninen T, Hallikainen M, Alhainen K, et al. Midlife vascular risk factors and Alzheimer's disease in later life: longitudinal, population based study. BMJ. 2001 Jun. 16;322(7300):1447–1451.

170. McKhann GM, Knopman DS, Chertkow H, Hyman BT, Jack CR Jr., Kawas CH, et al. The diagnosis of dementia due to Alzheimer's disease: Recommendations from the National Institute on Aging-Alzheimer's Association workgroups on diagnostic guidelines for Alzheimer's disease. Alzheimer's & Dementia. 2011 May;7(3):263–269.

171. Fonov V, Evans AC, Botteron K, Almli CR, McKinstry RC, Collins DL. Unbiased average age-appropriate atlases for pediatric studies. NeuroImage. 2011 Jan.;54(1):313–327.

172. Fonov V, Coupe P, Eskildsen S, Collins D. Atrophy-specific MRI brain template for Alzheimer's disease and mild cognitive impairment. Alzheimer's & Dementia. Elsevier Ltd; 2011 Jul. 1;7(S):S58.

173. Buckner RL. Molecular, Structural, and Functional Characterization of Alzheimer's Disease: Evidence for a Relationship between Default Activity, Amyloid, and Memory. Journal of Neuroscience. 2005 Aug. 24;25(34):7709–7717.

174. Frackowiak RS, Pozzilli C, Legg NJ, Boulay Du GH, Marshall J, Lenzi GL, et al. Regional cerebral oxygen supply and utilization in dementia. A clinical and physiological study with oxygen-15 and positron tomography. Brain. 1981 Dec.;104(Pt 4):753–778.

175. Mutsaerts HJMM, van Dalen JW, Heijtel DFR, Groot PFC, Majoie CBLM, Petersen ET, et al. Cerebral Perfusion Measurements in Elderly with Hypertension Using Arterial Spin Labeling. Jiang Q, editor. PLoS ONE. 2015 Aug. 4;10(8):e0133717.

176. la Torre de JC. Alzheimer disease as a vascular disorder: nosological evidence. Stroke. 2002 Apr.;33(4):1152–1162.

177. Langbaum JBS, Chen K, Caselli RJ, Lee W, Reschke C, Bandy D, et al. Hypometabolism in Alzheimer-affected brain regions in cognitively healthy Latino individuals carrying the apolipoprotein E epsilon4 allele. Archives of Neurology. 2010 Apr.;67(4):462–468.

178. Sakamoto S, Ishii K, Sasaki M, Hosaka K, Mori T, Matsui M, et al. Differences in cerebral metabolic impairment between early and late onset types of Alzheimer's disease. Journal of the Neurological Sciences. 2002 Aug. 15;200(1-2):27–32.

179. Nagata K, Buchan RJ, Yokoyama E, Kondoh Y, Sato M, Terashi H, et al. Misery perfusion with preserved vascular reactivity in Alzheimer's disease. Ann N Y Acad Sci. 1997 Sep.;826:272–281.

180. Stankiewicz J, Panter SS, Neema M, Arora A, Batt CE, Bakshi R. Iron in chronic brain disorders: imaging and neurotherapeutic implications. Neurotherapeutics. 2007 Jul.;4(3):371–386.

181. Jack CR, Petersen RC, Xu YC, O'Brien PC, Smith GE, Ivnik RJ, et al. Prediction of AD with MRI-based hippocampal volume in mild cognitive impairment. Neurology. 1999 Apr. 22;52(7):1397–1403.

182. Liu Y, Zhu X, Feinberg D, Guenther M, Gregori J, Weiner MW, et al. Arterial spin labeling MRI study of age and gender effects on brain perfusion hemodynamics. Magn. Reson. Med. 2011 Dec. 2;68(3):912–922.

183. Alsop DC, Detre JA. Reduced transit-time sensitivity in noninvasive magnetic resonance imaging of human cerebral blood flow. Journal of Cerebral Blood Flow & Metabolism. 1996 Nov.;16(6):1236–1249.

184. Dai W, Robson PM, Shankaranarayanan A, Alsop DC. Reduced resolution transit delay prescan for quantitative continuous arterial spin labeling perfusion imaging. Magn. Reson. Med. 2012 May;67(5):1252–1265.

185. Wu B, Lou X, Wu X, Ma L. Intra- and interscanner reliability and reproducibility of 3D whole-brain pseudo-continuous arterial spin-labeling MR perfusion at 3T. J. Magn. Reson. Imaging. 2013 May 30;39(2):402–409.

186. Birn RM, Diamond JB, Smith MA, Bandettini PA. Separating respiratory-variation-related fluctuations from neuronal-activity-related fluctuations in fMRI. NeuroImage. 2006 Jul.;31(4):1536–1548.

187. Liang X, Connelly A, Calamante F. Improved partial volume correction for single inversion time arterial spin labeling data. Magn. Reson. Med. 2013 Feb.;69(2):531–537.

188. Veltman DJ, Friston KJ, Sanders G, Price CJ. Regionally Specific Sensitivity Differences in fMRI and PET: Where Do They Come From? NeuroImage. 2000 Jun.;11(6):575–588.

189. Bäckman L, Andersson JL, Nyberg L, Winblad B, Nordberg A, Almkvist O. Brain regions associated with episodic retrieval in normal aging and Alzheimer's disease. Neurology. 1999 Jun. 10;52(9):1861–1870.

190. Pearlson GD, Harris GJ, Powers RE, Barta PE, Camargo EE, Chase GA, et al. Quantitative changes in mesial temporal volume, regional cerebral blood flow, and cognition in Alzheimer's disease. Arch. Gen. Psychiatry. 1992 May;49(5):402–408.

191. kesslak J, Nalcioglu O, Cotman C. Quantification of magnetic resonance scans for hippocampal and parahippocampal atrophy in Alzheimer’s disease. Neurology. 1991 Jan. 24;41:51–54.

192. Wechsler D. WAIS-III administration and scoring manual. The Psychological Corporation.; 1997.